

GPS Interference Mitigation for Small UAV Applications

by

Joy Li

Thesis submitted for the degree of

Master of Engineering, Science

School of Electrical and Electronic Engineering

The University of Adelaide

Adelaide, South Australia

March, 2009

ABBREVIATIONS.....	4
ABSTRACT.....	6
PUBLICATIONS	7
STATEMENT OF ORIGINALITY.....	8
ACKNOWLEDGEMENTS	9
INTRODUCTION	10
1.1 BACKGROUND	10
1.2 MOTIVATION	11
1.3 RESEARCH OBJECTIVES	12
1.4 THESIS OUTLINE.....	12
LITERATURE REVIEW	14
2.1 GLOBAL POSITIONING SYSTEM AND ITS APPLICATIONS.....	14
2.2 GPS VULNERABILITY	15
2.3 GPS ANTI-JAMMING TECHNIQUES	16
<i>Pre-correlation Techniques</i>	16
<i>Post-correlation Techniques</i>	24
SUMMARY	27
ADAPTIVE ANTENNA ARRAY OVERVIEW	29
3.1 FUNDAMENTALS OF ANTENNA ARRAYS	29
3.2 NULL STEERING	33
3.3 STEEPEST DESCENT AND LMS ALGORITHM	38
ANTI-JAMMING UNIT HARDWARE DESIGN	46
4.1 SYSTEM DESIGN AND PERFORMANCE SPECIFICATION	46
4.2 RF FRONT END DESIGN	48
4.3 RF FRONT END DYNAMIC RANGE	50
4.4 IF STAGE GAIN	54
4.5 FILTERING REQUIREMENTS.....	56
4.6 SUMMARY	58
HARDWARE IMPLEMENTATION.....	60
5.1 ANALOGUE FRONT END.....	60
5.2 ANALOGUE TO DIGITAL CONVERTER (ADC).....	62
5.3 COMPLEX DOWN-CONVERSION	63
5.4 DIGITAL SIGNAL PROCESSING	65
5.5 PHYSICAL STRUCTURE.....	72
LABORATORY PERFORMANCE TESTING	74

6.1 SENSITIVITY	74
6.2 SELECTIVITY.....	76
6.3 NON-LINEARITY OF RF FRONT END	77
6.4 OVERALL ANTI-JAMMING ABILITY ANALYSIS.....	80
6.5 OVERALL BROADBAND ANTI-JAMMING LAB TEST RESULT	81
6.6 PERFORMANCE ENHANCEMENT AND SIMULATION RESULTS.....	84
WOOMERA TRIAL 2006	87
7.1 UAV CONFIGURATION	87
7.2 TEST PROCEDURES AND RESULTS.....	90
<i>Top-bottom Configuration Static Test.....</i>	<i>91</i>
<i>Side By Side Configuration Static Test</i>	<i>93</i>
7.3 SUMMARY	96
CONCLUSION	98
APPENDIX A - IF PASSBAND SPECTRUM	102
APPENDIX B - IF PASSBAND SPECTRUM MISMATCH	103
APPENDIX C - SNAP SHOT OF DLMS INSIDE OF SIMULINK	104
APPENDIX D - C/NO OF ALL SATELLITES IN TRIAL	106
REFERENCES.....	107

Abbreviations

ADC: Analogue to Digital Converter
AGC: Automatic Gain Control
AJ: anti-jam/anti-jamming
AOA: Angle of Arrival
BPF: Band Pass Filter
CECOM: Communications-Electronics Command
CDMA: Code Division Multiple Access
C/No: Carrier to Noise Density Ratio
DAC: Digital to Analogue Converter
DLMS: Delayed Least Mean Square
DOA: Direction of Arrival
DSP: Digital Signal Processing
DSSS: Direct-Sequence Spread Spectrum
EMC: Electromagnetic Compatibility
FFT: Fast Fourier Transform
FIR: Finite Impulse Response
FPGA: Field Programmable Gate Array
GLONASS: Global Navigation Satellite System
GNSS: Global Navigation Satellite System
GPIB: General Purpose Interface Bus
GPS: Global Positioning System
IF: Intermediate Frequency
IP3: Third Order Interception Point
IIP3: Input IP3
INS: Inertial Navigation System
LMS: Least Mean Square
LNA: Low Noise Amplifier
LO: Local Oscillator
MDS: Minimum Detectable Signal
MSE: Mean Square Error
MVDR: Minimum Variance Distortionless Response
NF: Noise Figure

NLMS: Normalised Least Mean Square
OIP3: Output IP3
PCB: Printed Circuit Board
RBW: Resolution Bandwidth
RF: Radio Frequency
SFAP: Space Frequency Adaptive Processing
SFDR: Spurious Free Dynamic Range
SIR: Signal to Interference Ratio
SMA: Sub-Miniature A (type of RF connector)
SNR: Signal to Noise Ratio
STAP: Space Time Adaptive Processing
UAV: Unmanned Aerial Vehicle
VCO: Voltage Controlled Oscillator
VHDL: VHSIC (Very High Speed Integrated Circuit) Hardware Description
Language
WGN: White Gaussian Noise

Abstract

The vulnerability of GPS to interference has been a major concern for both military and civilian applications, including small UAVs. Various signal processing techniques have been developed to improve the reliability of GPS receivers against different types of interference. Among these techniques, null steering is recognized as an effective method to protect GPS against both narrowband and broadband interference. However, due to the requirement of multiple antenna channels, it has mainly been implemented for large platform applications.

This thesis examines the suitability of null steering techniques for small UAV applications and determines the practically achievable anti-jamming ability by implementing a two-element miniaturized adaptive antenna array.

The adaptive antenna array is tested against a 2MHz broadband jamming signal under both laboratory testing conditions and a real jamming environment. Approximately 40dB anti-jamming range was achieved in the laboratory testing conditions. 38dB and 42dB were obtained in a real jamming environment with different antenna configuration. The likely performance limitations and possible further performance enhancements are also outlined in this thesis.

Publications

J. Li & M. Trinkle, “Miniaturized GPS interference canceller for UAV application”, presented at IGNSS-07, December 4-6, 2007. Awarded for “*Best Academic Paper*”.

Statement of Originality

This work contains no material which has been accepted for the award of any other degree or diploma in any university or other tertiary institution and, to the best of my knowledge and belief, contains no material previously published or written by another person, except where due reference has been made in the text.

I give consent to this copy of my thesis, when deposited in the University Library, being made available for loan and photocopying, subject to the provisions of the Copyright Act 1968.

SIGNED:

DATE:

Acknowledgements

I wish to thank my supervisor Mr. Matthew Trinkle for the support, attention, patient effort and encouragement given to me during my study. I also would like to thank my principal supervisor Prof. Doug Gray for his guidance and much-valued time. Without their support and encouragement, the completion of this thesis would not have been possible.

I would like to acknowledge that the funding and part of the test equipment used during the trial for this study were provided by the Defence and Science Technology Organisation. I would especially like to thank Dr. Chris Baker, Dr. Mark Knight and Mr. Gary Fielke for their generous support during the trial.

I am also most grateful to Mr. Tyson Ritter for proofreading my thesis. It was his support ensured that this thesis was completed on time.

Finally, I would like to extend a heartfelt thanks to all my friends and work colleagues at the Sensor and Signal Processing Group at the University of Adelaide for their encouragement and support. I have benefited greatly from the many inspiring discussions.

Chapter 1

Introduction

1.1 Background

The Global Positioning System (GPS) has become a critical part of the global navigation infrastructure. It was initially designed and implemented for military application only by the United States. Its applications include precise absolute worldwide navigation for ships, aircraft, land vehicles, and even individual soldiers. However, it has experienced explosive growth in usage since it was made available to civilian users in 1996. Commercial applications have expanded far beyond vehicle navigation to include, for example, geodynamic measurements for earthquake and volcano studies, precision agriculture, and precise timing to facilitate/synchronize communications for applications such as cellular telephones and financial transactions [1]. GPS is the only fully functional Global Navigation Satellite System (GNSS) at present.

Traditionally, GPS is designed to provide absolute worldwide navigation. This is achieved by utilizing a constellation of at least 24 medium earth orbit satellites such that at any time and any location on Earth, there are at least 4 satellites in view. GPS receivers calculate their own positions by estimating their relative distances to satellites that are presently in view. Standard GPS receivers are required to have an acquisition sensitivity of at least -130dBm to be able to provide position in an outdoor environment.

Due to the usage of direct sequence spread spectrum (DSSS) method, GPS has some inherent immunity to interference. However, the vulnerability of the GPS system is a long known problem, mostly due to the long travelling distance required for the GPS signals to reach the Earth's surface. Many studies have been carried out aimed to

reduce the sensitivity to in-band noise of the GPS system. Although much success has been achieved, as there are many ways to overwhelm a GPS receiver and the close in distance advantage, to protect a GPS receiver from interference is not always easy.

1.2 Motivation

As an increasing number of applications rely on GPS, the public demand for higher quality GPS services is continually increasing. One area driving the research is that of improved safety and reliability in military applications of GPS. One such application is Unmanned Aerial Vehicles (UAVs). A UAV is sustained in flight by aerodynamic lift and guided without an onboard crew. It may be expendable or recoverable, and can fly autonomously or be piloted remotely. Historically the greatest use of UAVs has been in the areas of surveillance and reconnaissance. The availability of GPS is critical to UAVs as it used to provide precise positioning and navigation [2].

To provide GPS anti-jamming for small UAVs is particularly challenging as the anti-jamming unit is required to be small and light due to the limited size and loading capacity of small UAVs. Another constraint, which makes the design task more difficult, is the need for low power consumption. This allows UAVs to maximize their flight duration.

Many different GPS anti-jamming techniques have been studied and developed to date. The literature review demonstrates that the application of null steering by using an adaptive antenna array is a simple technique which can effectively protect spread spectrum communication such as GPS from both narrowband and broadband interferences. However, previous studies considering this technique have been mainly directed at larger platforms and the algorithmic details for performance improvements.

At present no performance results are available in the open literature for a miniaturised null steering anti-jam unit, particularly for a GPS guided UAV, to the author's knowledge. Hence, no real data exists which describes the anti-jamming ability of this method and its practical limitations in a jamming environment. Such

data would be useful for validating computer models and to achieve further performance improvements.

1.3 Research Objectives

This research is aimed at investigating the suitability of null steering technique for small platform applications and to estimate the practical interference rejection gain and other performance measurements by implementing a two-element adaptive antenna array. The study is particularly targeted at small GPS guided UAVs, where physical size, power consumption and weight of the anti-jamming unit are the critical design constraints.

1.4 Thesis Outline

Chapter 2 gives an overview of the vulnerability of GPS to interference and the interference mitigation techniques available in the open literature.

Chapter 3 explains the fundamentals of adaptive antenna arrays. Null steering is reviewed in detail along with the Least Mean Square (LMS) algorithm.

The anti-jamming unit specification and system design are explored in Chapter 4. The choice of components has been analysed based on a desired performance specification.

Chapter 5 focuses on the detailed hardware implementation. Challenges and limitations have been investigated and explained in this chapter.

The anti-jamming unit has been tested in a laboratory jamming environment. Chapter 6 gives the detailed procedure of laboratory tests and the resulting performance.

The anti-jamming unit has also been tested in a real jamming environment. Chapter 7 summarizes the trial held in Woomera SA in 2006, and includes details of the testing procedure and corresponding performance results obtained.

Chapter 8 concludes this thesis, summarising the achievements made and possible future developments that could be undertaken.

Chapter 2

Literature Review

2.1 Global Positioning System and its Applications

GPS is a world-wide satellite navigation system, consisting of typically more than 27 satellites in total that provide users with precise position, time and velocity information by using spread spectrum techniques. All GPS signals are transmitted on two carrier frequencies, L1 on 1.57542GHz and L2 on 1.2276GHz using code division multiplexing.

Spread spectrum technology forms the backbone of third generation communication systems. In spread spectrum communication, the information signal is deliberately spread over a wide range of frequencies [13]. This is achieved by multiplying the information signal with a known noise-like signal before it is transmitted. This provides increased resistance to natural interference and the ability to avoid hostile detection. There are two different types of noise-like signals used by GPS for multiplexing. One is the Coarse/Acquisition or CA code, which is modulated on the L1 carrier and is available to civilian users. The other kind is precision code or P code. It is a one week period code. As it was published in GPS-ICD-200, July 1992 [29], it is available to potential spoofers or jammers [30]. For this reason, GPS has the option to replace P code with encrypted Y code which is only available to authorized users [8] [16] [31, p123]. Y code is modulated on both L1 and L2 carriers.

The GPS system has become a vital global utility, being indispensable to modern navigation, map making and land surveying. It also provides an extremely precise time reference, which is required in industries such as telecommunications and scientific research. GPS plays a very important role in military applications. An example application is guiding an unmanned aerial vehicle for tasks such as surveillance and reconnaissance.

2.2 GPS Vulnerability

GPS has some inherent immunity to interference, due to its spread spectrum characteristics. However, the GPS received signal has very low power as it has travelled 20,200km to reach the receiver. The minimum guaranteed signal level on the Earth's surface is only -158.5dBW [31, p262] [29]. At this power level, it is easy for a local in-band source to overwhelm the GPS signal. Reynolds et al. [35] claims that a jammer with power as little as 0.1W located up to 80km away from the receiver could prevent successful C/A code acquisition.

There are three main known sources of unintentional interference reported in [2]. They are:

- FM radio broadcast stations: 92.7 and 98.5MHz have harmonics falling within the GPS L1 frequency.
- Television broadcast stations: channel 66 has a second harmonic that falls within 80kHz of the L1 passband.
- Mobile satellite service transmitters.

Intentional GPS jamming is simple, both in principle and in practice [14]. According to Kaplan [31, p269], a 4-watt jammer can successfully prevent a standard military P code GPS receiver from tracking as far away as 8.3km. This example demonstrates the vulnerability of GPS to jamming signals.

The GPS signal modulation and frequency allocations are publicly available. This makes the signal easy to jam, as any intentional jammer can concentrate all of its power within the GPS signal bands. Commercial GPS jammers have been available on the market since 1997. The Russian firm Aviaconversia marketed and displayed a portable GPS and GLONASS jammer at the Moscow Air Show [16]. Hence, anti-jamming techniques are important for GPS systems.

2.3 GPS Anti-Jamming Techniques

Many different GPS anti-jamming techniques have been studied and developed to date. Signal processing dimensions of amplitude, frequency, time, space, and polarization have been exploited, in many cases with high degrees of anti-jamming success. Depending on whether the processing occurs before or after the GPS receiver, these techniques can be loosely classified as either pre-correlation or post-correlation techniques. For small low-value military platforms, interference suppression techniques are required to add a significant margin to receiver interference tolerance and be effective for all known types of interference. It is also desirable to use small low-cost antenna systems that can be cost effectively added to new GPS receivers or retrofitted to existing legacy GPS receivers [12]. Based on these requirements, the most commonly used anti-jamming techniques are described in the sections below and their suitability for a small UAV application is analysed.

Pre-correlation Techniques

As the name suggests, pre-correlation techniques are usually implemented in external hardware in front of the GPS receiver, prior to the tracking loop. Significant additional DSP processing power is required, but at the same time, this approach provides a simple “add-on” structure which can be applied to any existing GPS receiver without any modifications.

Pre-correlation techniques can provide effective protection against narrowband interference. Some of the techniques in this category can also significantly increase the robustness of a GPS receiver against broadband interference. They are often suitable for military applications due to their capability of providing large anti-jamming (AJ) range against narrowband and/or broadband interference signals. Commonly used pre-correlation techniques include adaptive temporal filters, adaptive spatial filters, space-time adaptive filters and space frequency adaptive filters. They are summarised below.

Adaptive Temporal Filters

Adaptive temporal filters are a well-known pre-correlation technique. The filter is formed either in the time domain or frequency domain by using an FFT. For narrowband interference, they significantly reduce the in-band interference power while having very little effect on the desired GPS signal. This is possible because of the wideband characteristic of GPS, allowing narrowband interference signals to be identified and notched out in the frequency domain without causing significant distortion to the GPS signal.

Capozza et al. [8] devised one kind of adaptive temporal filter by simply setting frequency bins, whose magnitude-square values are greater than a certain threshold, to zero. The threshold is approximately proportional to the mean noise power without interference and is chosen to reduce the interference power as much as possible while minimizing GPS signal degradation. This approach has been implemented in a custom VLSI chip and the integrated hardware was tested in a laboratory condition. Over 40dB AJ range was achieved against a single CW interference. Experiments with multiple uncorrelated CW interference sources were also conducted. However, the pseudo-range error increased by at most 80% due to the degraded quality of the GPS signal. Capozza et al concluded that the increased pseudo-range error due to the insertion of the narrowband interference suppressor can be viewed as an increase in the receiver noise figure and therefore can be mitigated to some extent by designing a very low noise figure receiver albeit at a higher cost.

Windowing is often used in the FFT technique to help reduce the frequency sidelobes caused by the finite duration of the FFT. On the other hand, windowing also degrades the carrier-to-noise power spectral density ratio. Depending on the type of window applied, the insertion loss can be as high as 3dB. For this reason, a second FFT and suppression algorithm running with 50% overlap at the inverse FFT output is applied. This technique is sometimes referred as Overlapped FFT (OFFT). It has an inherent fast response time; therefore, it is most applicable in a rapidly changing interference environment. A detailed comparison between different windowing techniques and their corresponding performance has been conducted in [10].

Adaptive Temporal Filters can also be realized in the time domain by using prediction filters. Interference cancellation is achieved by predicting the narrowband interference(s) based on previous samples and then subtracting the predicted signal from the received signal. Because noise is not predictable and the GPS signal is below the noise, only narrowband interference signals will be mitigated during this process.

A GPS interference canceller has been implemented previously by using the adaptive temporal filter approach [36]. The unit was implemented based on FPGA technology and an overall anti-jamming range of 35dB was achieved against narrowband interference.

Adaptive Temporal Filters potentially provide a large AJ margin against CW and narrowband interference(s). The maximum AJ range is usually limited by the dynamic range of the ADC [9]. However, they are not the ideal technique for UAV applications because they cannot provide protection against broadband interference signals.

Adaptive Spatial Filters

“Spatial domain filtering utilizes antenna-pattern control/discipline and various antenna array techniques to implement beam and/or null steering optimization.” [12] To achieve this, a multi-element antenna array is required. These antennas are arranged in space and are processed to produce a directional response, which concentrates energy from a selected direction whilst rejecting signals radiated from other directions. As a result, interference signal(s) are rejected in angle, rather than in the frequency or time domain. Such techniques often achieve large AJ margins and are effective against both narrow and broadband interference signals [9]. However, there is a limit to the number of interference signals from different directions that can be cancelled. This limit is referred to as the number of degrees of freedom in mathematics. For example, if there are N antennas in the array, then only up to $N-1$ spatially independent interference signals can be rejected. The two main adaptive antenna techniques discussed below are null steering and beam steering.

Adaptive spatial filters must use an adaptive algorithm to adjust to non-stationary interference(s) and changing characteristics of the GPS signal [13]. The adaptive

algorithm provides an optimum solution to the spatial filters, usually subject to minimising the output error power of the array. Depending on how the error signal is defined, either beam steering and/or null steering is realized.

Because adaptive spatial filters reject interference signals in angle, there is a trade-off between the amount of interference suppression and GPS signal preservation. For instance, when the direction of a GPS signal lines up with the interference signal, rejecting such an interference will also block the signal from that satellite.

Null steering: Null steering, often known as side lobe canceller (SLC), has been a commonly applied technique used for effective interference rejection in GPS receivers. It suppresses interference(s) by automatically forming a null in the direction of the interference while trying to maintain unit gain in all other directions. Various techniques have been proposed in the open literature for null steering, and one of the most common and simplest approaches is “power minimization”.

The power minimization approach is based on the fact that before correlation, GPS signals are well below the noise power. Therefore, any signals that are above the noise power observed at the receiver can be considered as interference. By applying spatial filtering, such an interference can be removed by steering a null in its direction, hence reducing the total received power. However, this process will have little effect on the spread spectrum GPS component. For an N-element antenna array, to guarantee that power minimization is achieved by cancellation of interference and not by attenuation of received signals, it is required that the weight of a reference element be fixed at unity, while the others are adaptively adjusted [17].

Null steering has the disadvantage of potentially reducing the received GPS signal level when the GPS signal is incident near to the direction of a jamming signal. However, this is not a major issue as a GPS receiver only requires four satellites to calculate a position while there are often more than six satellites simultaneously visible in the sky. The overall AJ range of the unit is fundamentally limited by the overall system dynamic range and it can be inserted between any existing antennas and receiver without any receiver modification. Most importantly, null steering does not require any prior knowledge of the direction-of-arrival information of the GPS

signals. This advantage makes null steering particularly favourable for UAV applications, as keeping track of the GPS signal DOA could be difficult, given that the orientation of the UAV changes rapidly during flight. It also avoids the requirement for precise antenna calibration.

Beam steering: Instead of minimizing the received signal energy level as in null steering, beam steering attempts to maximize the Signal to Noise Ratio (SNR) by steering a beam in a given direction. Beam steering techniques can be classified as either conventional beam steering or adaptive beam steering. Conventional beam formers use a fixed set of weights to combine the signal from sensors in the array, primarily using only information about the location of the sensors in the space and the signal directions of interest, i.e. desired satellite signals. In contrast, adaptive beam steering techniques generally combine this information with properties of signals actually received by the array, typically to improve the rejection of unwanted signals from other directions. As the GPS receiver requires at least 4 satellite signals to determine the position, multiple spatial filters have to be formed, one for each GPS satellite. Therefore, beam steering techniques require prior knowledge of the satellite signal direction relative to the antenna array orientation which is not always available. In practical situations, these filters share the same antenna array, down conversion stages and ADC converters.

Optimum beam steering techniques most often use the criterion known as Minimum Variance Distortionless Response (MVDR). “The MVDR filter is designed to minimize the filter output variance subject to the constraint that the filter remains distortionless in the vector direction of the signal of interest.” [19] In this case, the output power of each spatial filter will be minimized subject to it having unity gain in the direction of the desired GPS signals.

Beam steering has several advantages over null steering. Because a separate beam is formed at each GPS satellite, a factor of N improvement in SNR will be gained in a non-interference environment, where N is the number of array elements [9]. It also allows the array to be used for accurate carrier phase differential tracking techniques. This is because the MVDR will maintain unity gain in the direction of the desired GPS signals. The MVDR criterion will also utilize the available degrees of freedom to

shape the spatial null to minimise GPS signal cancellation, thereby increasing the probability that GPS signals will be preserved.

Beam steering requires prior Angle of Arrival (AOA) information for each GPS signal to be able to steer a beam in its direction. This information may not be available all the time. Forming a separate beam for each satellite also requires the output from each spatial filter to be passed independently to the GPS receiver. Such functionality is not available yet for most commercial receivers currently available on the market. A customised GPS receiver will increase integration cost. Due to these reasons, beam steering is not considered for small UAV applications.

In recent studies, Greg S. Loegering proposed that a dual-redundant anti-jamming architecture should be applied for GPS guided air vehicle navigation systems [2]. This essentially means two independent GPS receiver units should be installed at the same time with different anti-jamming techniques applied to each receiver. This solution allows the GPS navigation system to be protected when multi-sourced jamming signals are present with different jamming techniques applied. However, such implementations would significantly increase the total size and weight of the anti-jamming unit. Hence, it is not likely to be suitable for applications like small UAVs where physical size and weight are critical design constraints.

A combined beam steering and null steering technique has been proposed by Raymond J. Masak originally in 1988[20]. A beam steering adaptive control loop is simultaneously employed in combination with a null-steering adaptive control loop to enhance the Signal to Interference Ratio (SIR) resulting in an increase in the message quality [21]. Masak also showed a 6dB improvement in SIR when using the combined beam steering/null steering technique against null steering alone. This test was conducted by using a five-element random spaced antenna array with three interference sources. Each interference signal was 10dB above the desired GPS signals at each antenna.

Space-Time Adaptive Filters

Space-Time Adaptive Filters (STAP) perform 2D filtering on signals to remove narrowband and broadband interference signals at the same time. This is achieved by

adding a complex tap-delay line (temporal filter) after each antenna element. “In STAP, the filter coefficients (adaptive antenna weights), in general, are adjusted to minimize the mean output power subject to the look direction constraints.”[18] The optimum solution to this problem requires the manipulation of $LN \times LN$ sized matrices, where N is the number of antenna elements and L is the number of taps behind each antenna element.

The advantage of using STAP is its ability to eliminate N-1 spatially independent wide band interference signals by spatial filtering and additional narrowband interference signals at the same time by temporal filtering. The maximum number of additional nulls that can be formed against narrowband interference signals is $(L-1)/2$ [21]. Because STAP processes signals in both the spatial and temporal domain, it is able to steer nulls in the angle-frequency plane. This allows the antenna array to enhance its interference localisation ability resulting in less chance of cancelling a desired GPS signal [9].

Hatke et al. [16] demonstrated that STAP can also be used to protect a GPS receiver from multipath reflections of the interference arising from nearby objects, such as reflections from the airframe of the aircraft. Gupta and Moore [18] also stressed the importance of this point. “Since the interference signal can be wide band in nature and may have strong multipath, STAP is being proposed for interference suppression.” [18] Most RF adaptive beam steering systems operate under the assumption that the bandwidth of the jamming source can be cancelled using one spatial degree of freedom. This implies that the signals seen at all the antenna elements of the array due to a single jammer have cross-correlation coefficients with magnitude one. However, multipath will cause the signals, including the jamming signal, at each antenna to be only partially correlated with each other [16]. This de-correlation of the jammer signal due to multipath can be compensated by using STAP processing and has made STAP more favourable in dealing with multipath problems than spatial only filtering.

Adding temporal taps to implement space-time adaptive processing will potentially result in a non-uniform frequency response across the operating band. Hence, it is possible that distortion is introduced to the desired GPS signals [14] [22]. Another

characteristic of STAP, which makes this technique less popular in practice, is that $NL \times NL$ space-time matrices need to be manipulated. This will significantly increase the computational complexity of the adaptive algorithm. Advanced adaptive algorithms have been proposed, aimed at reducing the computational complexity for the implementation of STAP. These include the “reduced-rank power minimization” algorithm based on nested Wiener filters [24] [11].

A small affordable anti-jam GPS antenna (SAAGA) has been developed by the U.S. Army CECOM. This unit employs a 4-element antenna array and 31 tap STAP technology [22]. The unit is capable of both L1/L2 operation and provides 30dB interference power suppression against 3 wideband and 7 narrowband interference signals in simulations. In this design, the spatial filter is cascaded with a single FIR filter for the purpose of reducing computational cost. The single FIR filter also results in less distortion to the timing information of the GPS signal, as all channels will experience the same delay. However, a special adaptive algorithm must be applied to ensure that the broadband interference signals are allocated to the spatial filter and the narrowband interference signals to the temporal filter [9]. Therefore, this anti-jam unit is not capable of handling multipath as it only uses a single filter for all antennas.

Space-Frequency Adaptive Filters

“Space-frequency adaptive processing (SFAP) is an alternate approach to STAP where the time domain signals received by various antenna elements are transformed to the frequency domain using the discrete Fourier transform, and the constraint is applied in the frequency domain to suppress the interfering signals.” [18] The transformation from the time domain into the frequency domain is achieved by using an FFT. Therefore the operating bandwidth B is split into L sub-bands each with a bandwidth of B/L . The weight of each antenna is then calculated within each sub-band and the interference is mitigated by placing a spatial null within each bin while preserving the signal. In a SFAP processor, the adaptation is usually performed independently within each frequency bin for the antenna weights and this often leads to a suboptimum solution. The finite width frequency response of the FFT also causes energy leakage between frequency bins. This will also degrade the performance of SFAP compared to STAP. The advantage of SFAP, on the other hand, is its reduced

computational cost. The manipulation of the matrix dimension is reduced from $LN \times LN$ to only L of $N \times N$ matrices [18].

With fixed amount of computational load, the suboptimum SFAP can afford many more taps in its filter due to reduced computational requirements. However, the advantage of using the SFAP is not always obvious. The key factor which determines which algorithm will result better performance is system dynamics. Fante and Vaccaro [23] concluded in their study that SFAP only outperforms STAP when the requirement for the weight update rate is higher than 10kHz. Gupta and Moore [18] stated that in a mixed wide band and narrowband RF environment, applying a window function in the time domain before transforming the signal into the frequency domain could improve the performance of SFAP. This is because the windowing function helps to localize the narrowband interference signals into fewer frequency bins by reducing sidelobes.

Post-correlation Techniques

Pre-correlation techniques are normally expensive and physically bulky due to the external hardware requirements in front of the GPS receiver. As a result they are often not suitable for civilian GPS users.

Compared with pre-correlation techniques, post-correlation techniques are relatively simple. They usually involve modifications to the GPS receiver tracking loop. A major advantage of these schemes is that they are effective against all interference waveforms and require little, if any, modification to the receiver hardware as for most techniques can be implemented by software. Some can be implemented completely in software. On the other hand, the amount of protection post-correlation techniques provide is usually significantly less compared with pre-correlation techniques [9]. The most commonly applied post-correlation techniques include:

Adaptive Loop Bandwidth

In a high noise environment, a simple solution is to decrease the closed-loop bandwidth of the tracking loops since the amount of noise present in the system is directly proportional to the loop bandwidth. However, this will also result in a lower

system dynamic tracking ability. It is desirable to have a wider tracking loop bandwidth when the Doppler shift is changing rapidly.

Adaptively adjusting the tracking loop bandwidth according to the dynamic conditions and interference power would best optimize the system performance against noise. This technique is known as Adaptive Loop Bandwidth. By reducing the loop bandwidth, higher anti-jam margins can be achieved, typically 10dB [9]. The limitation of this approach is that interference mitigation can only occur in low dynamic conditions.

Data Wiping

One of the most effective techniques is to increase the pre-detection integration time, also known as coherent integration time. In a typical GPS receiver, the hardware may coherently integrate the correlated signal for a millisecond before it is used in the tracking loops. In a jamming environment, longer coherent integration time will increase the processing gain, and hence improve the C/No. However, as the navigation data message is also embedded in the GPS signal, the longest possible integration period is 20ms. This corresponds to the bit period of the navigation message. Continuing to integrate past the bit boundary runs the risk of having the data bit change value, hence reducing the correlation peak of the GPS signal. Therefore, integration times longer than 20ms can only be achieved if the 50Hz navigation data is removed from the received signal. This technique is commonly recognised as “Data Wiping”.

To realize data wiping, the receiver has to know the value of the navigation data. Some receivers simply assume the navigation data does not change with time and store a complete message [9]. A more effective method is to obtain the navigation data and coherent information by using network assistance, however this approach will significantly increase the integration cost. It is currently planned to broadcast the new civil signal on L2 frequency without the navigation data for the next generation of GPS [25].

There is a limit on how long the integration time can be. Long integration times will result in the receiver providing independent updates less often and requires a smaller

loop bandwidth hence slower system dynamics. The length of the integration should be chosen based on the application of GPS and the user error tolerance. “Data Wiping” in general can improve the tracking threshold of GPS receivers by up to 6dB, and is most effective for GPS receivers that already have high anti-jam immunity [9].

Integration with INS

Inertial navigation methods have been used in a wide variety of navigation applications in the fields of marine, aerospace and spacecraft technology. Compared with GPS, Inertial Navigation Systems (INS) update at a much faster rate, if not in a continuous fashion. Unlike GPS, the INS systems achieve navigation by continuously tracking the position, orientation and velocity information using computers and motion sensors. As errors tend to accumulate over the time, the INS systems suffer from a constantly drifting position solution. However these position errors are introduced at a slower rate than the GPS errors. The complementary characteristics of GPS and INS have led to a combined GPS/INS approach, sometimes referred to collectively as GPS/INS coupling. Such an integration scheme provides users with immunity against momentary GPS signal outages and signal failure detection in a noisy or jamming environment.

Several architectures have been proposed for combining the measurements from each source in various forms on three different levels. The most obvious way is to combine the navigation solution from each system to improve the accuracy. This is achieved by using an optimum integrating filter and is referred as “loose coupling” mode.[26] The optimum integrating filter is realised using two cascaded Kalman filters, one inside of the GPS receiver and one external to combine GPS and INS outputs [28] [27]. As the GPS and INS remain completely separate in this integration, a minimum of 4 satellites are still required by the GPS receiver to provide coordinate/velocity inputs to the integration Kalman filter and no AJ is achieved at this stage. To overcome this problem and better utilize GPS and INS information, a “tightly-coupled” GPS/INS architecture has been developed. In this approach, raw data from GPS (such as pseudo-range) are combined with INS measurements, and this results in significant system improvement. Another advantage of this approach is that only one Kalman filter is required. This simplifies the calculation process and results in a more

optimised solution. The quality of the navigation service may be improved, however no AJ is achieved.

A third architecture of integration is so-called ultra-tight configuration, in which the tracking loops within the GPS receiver are replaced with a single loop that is closed through a Kalman filter. With this configuration, only errors in the aiding velocity need to be tracked by the receiver instead of the absolute motion compare with previous configurations [39]. Various studies have shown that ultra-tight coupling outperforms the tightly-coupled architecture in many ways. This includes improvements in jamming to signal ratio, and RF interference mitigation, a reduction in non-coherent integration period in weak-signal GPS processing and lots of other benefits. [28]. The limitation of this technique is its computational complexity mainly due to the Kalman filter used. Therefore, it is not straight forward to implement it in a real time application.

Summary

As has been described in the research objectives, this project considers the design of an anti-jamming unit particularly for small UAV applications. The anti-jamming technique for this application is expected to add a significant margin to the receiver interference tolerance by using a small low-cost antenna array system. The chosen technique should also be effective for most, if not all, known types of interference. It is also desirable to design a versatile unit which can be cost effectively added to any new or existing GPS receivers. .

As pre-correlation techniques are able to provide a significant amount of AJ protection for both broadband and narrowband interference signals and at the same time require no modification to GPS receivers, they are preferred over post-correlation techniques for this project.

Considering all pre-correlation anti-jamming techniques which have been described in this chapter, null steering appears to be the most suitable techniques due to its simplicity and effectiveness against both narrowband and broadband interference signals. Such a technique also provides an “add-on” structure which allows the anti-

jamming unit to be incorporated with any existing GPS receivers without any modification.

To further improve the anti-jamming ability and reduce the constraints during the design process, a few STAP taps were incorporated with the null steering algorithm to reduce the mismatch between the RF front ends.

Chapter 3

Adaptive Antenna Array Overview

In the literature review section, the null steering technique of spatial filtering has been shown to be one of the more effective techniques for interference rejection in GPS receivers. The anti-jamming unit has been designed with this approach by using a two-element antenna array. To reduce the mismatch between the two RF front ends, a tap-delay line has also been added on the auxiliary antenna channel. The detailed design can be found in Chapter 4. This chapter explains the fundamentals of the adaptive antenna array and how “power minimization” can be applied to the anti-jamming unit.

3.1 Fundamentals of Antenna Arrays

An antenna array is by definition a radiating (or receiving) configuration consisting of more than one antenna element [2]. These antenna elements are arranged in space such that the overall radiation (or reception) pattern of their combined output is different to the output of each individual element. There are many ways to arrange the antenna elements, resulting in a variety of radiating structures with differing properties. The directionality and sensitivity of the overall radiation pattern can also be controlled by manipulating the amplitude and phase of individual element outputs before combining them together.

To demonstrate the basic principle of antenna arrays, consider a simple two-element antenna array as shown in Figure 1. To further simplify the analysis, it has been assumed there is a single frequency component in the received signal. Signals containing multiple frequency components can also be analysed in the same way by using superposition.

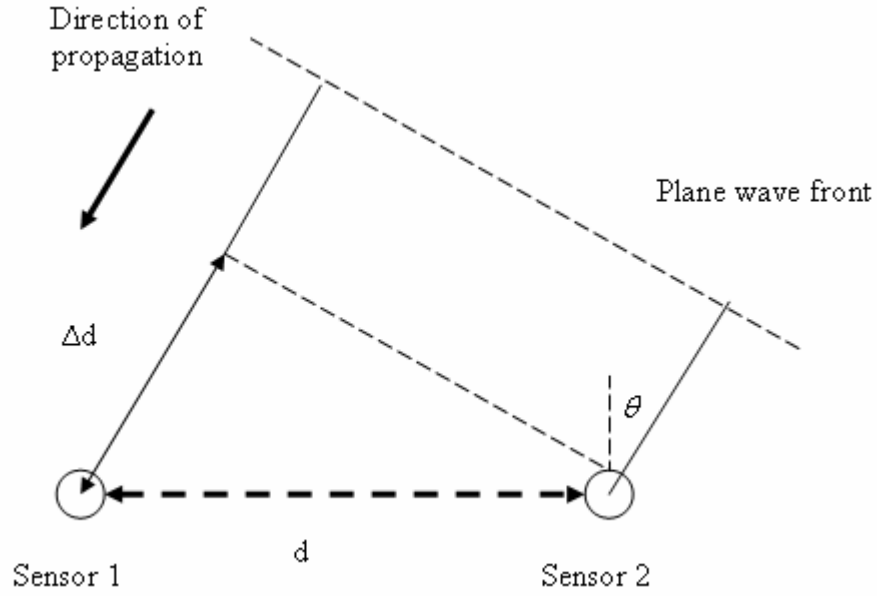


Figure 1: Phase relationship for plane wave incident on a two antenna system

The above diagram clearly indicates that the signal has to travel extra distance to reach sensor 1 compared with sensor 2. The signal received by sensor 1 will be both time and phase delayed due to the extra distance travelled. This is also approximately true for narrowband signals. In Figure 1, θ is used to represent the angle between the direction of propagation and normal of the array. The extra distance travelled then depends on the space between the two elements, d , and angle θ . By using simple geometry, the additional distance the wave has to travel to reach sensor 1 is given by $\Delta d = d \cdot \sin \theta$.

This concept can be mathematically generalised to an array of arbitrary shape by using a 3D coordinate system. Consider Figure 2, where a single plane wave is incident upon the array from the azimuth and elevation directions θ and Φ respectively.

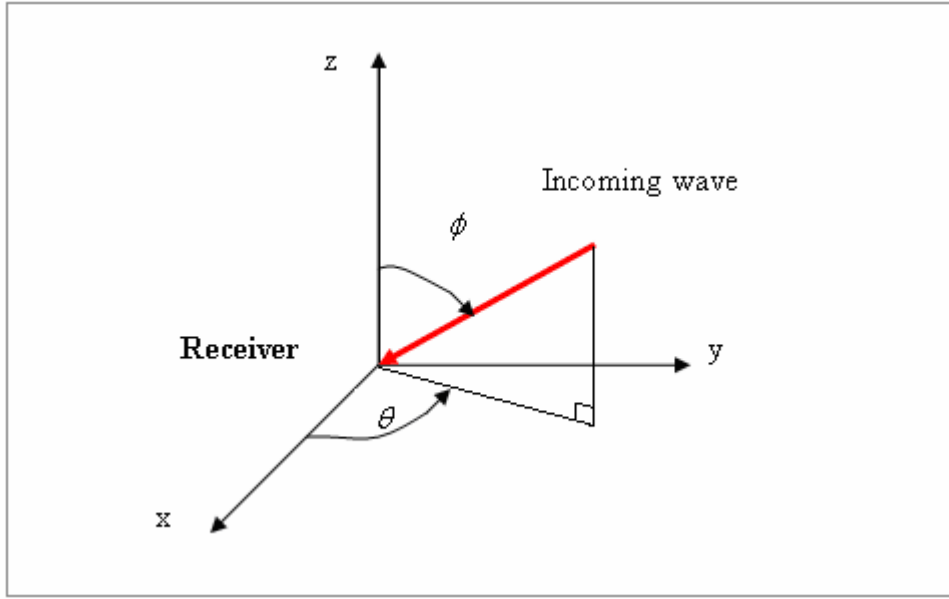


Figure 2: 3-D coordinate system for antenna array system

In this coordinate system, (x_j, y_j, z_j) are the coordinates of the j^{th} receiving antenna. Hence the phase delay to the j^{th} receiver can be given by $k^T u_j$ where

$$k = \frac{2\pi}{\lambda} \begin{bmatrix} \cos \theta \sin \phi \\ \sin \theta \sin \phi \\ \cos \phi \end{bmatrix} \text{ and } u_j = \begin{bmatrix} x_j \\ y_j \\ z_j \end{bmatrix} \quad \text{Equation 1}$$

For example, if a signal $s(t)$ is incident upon the array from the direction of k_s , then the phase delay due to the spatial separation of the receivers can be represented by using vector $v(k_s)$, where

$$v(k_s) = \begin{bmatrix} \exp(ik_s^T u_1) \\ \exp(ik_s^T u_2) \\ \vdots \\ \exp(ik_s^T u_k) \end{bmatrix} \quad \text{Equation 2}$$

Therefore, the received signal vector of the antenna array is given by

$$x(t) = s(t)v(k_s) \quad \text{Equation 3}$$

For conventional beamforming, each element output x_j is multiplied by a complex weight, modifying the phase and amplitude relation between elements. This complex weight vector is known as the steering vector $v(k)$, where k is the steering direction. Therefore, if there are K receiving antennas in total, the output of the antenna array can be obtained by substitution, for example:

$$y(k, k_s, t) = \frac{1}{K} v^H(k) x(t) = \frac{1}{K} s(t) v^H(k) v(k_s) \quad \text{Equation 4}$$

In the scalar form,

$$y(k, k_s, t) = \frac{1}{K} s(t) \sum_{j=1}^K \exp(i(k_s - k)^T u_j) \quad \text{Equation 5}$$

By examining the above equation, it is clear that the output of the array is dependent on both the steering direction k of the array and target direction k_s . The array will have maximum output when the steering direction is matched to the target direction. This is often illustrated via the beam pattern of the array, which is the output power of the array steered in the direction k when a signal of unit amplitude is incident upon the array from direction k_s , and is given by

$$P(k, k_s) = \frac{|y(k, k_s, t)|^2}{|y(k, k, t)|^2} = \frac{\left| \sum_{j=1}^K \exp(i(k_s - k)^T u_j) \right|^2}{K^2} \quad \text{Equation 6}$$

A two-element conventional beamformer has been simulated in MATLAB. The array is setup as illustrated in Figure 1. The sensors are placed a half wavelength apart from each other and the target angle is 45° . Both antenna elements are given a weight of 1, so the beam pattern should have maximum gain at the target angle of 45° . The incident wave is given an amplitude of 10 units. The beam pattern of such an array is plotted in Figure 3.

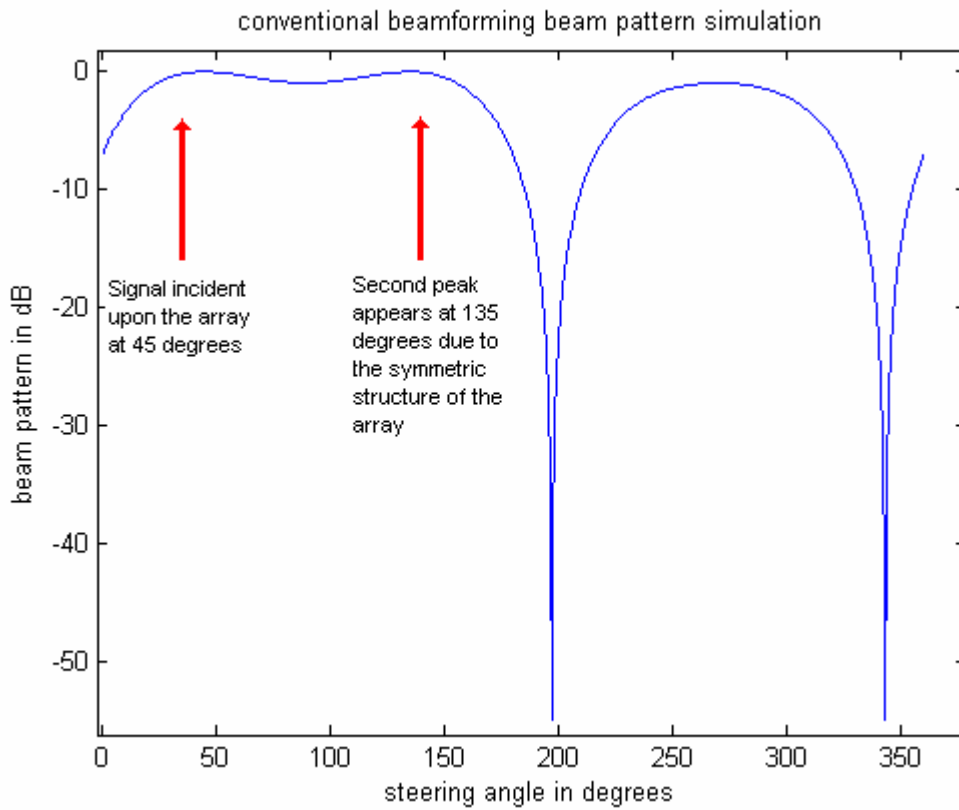


Figure 3: *Beam pattern of two-element conventional beam former*

The above plot clearly shows that the maximum gain of the array is at the steering angle of 45° , which is also the target direction. The beam pattern also shows a second peak at 135° . This is due to the symmetric structure of the array, which results in the same phase relationships in the two sensors when steering at 45° and 135° . These angles are ambiguous to the array and cannot be distinguished without further spatial information.

3.2 Null steering

Figure 4 illustrates a simple adaptive antenna array system. Each received signal is multiplied by a complex array weight before being combined together to form the final output. The weight vector is constantly updated by a weight update algorithm that adapts to the changing radiation environment.

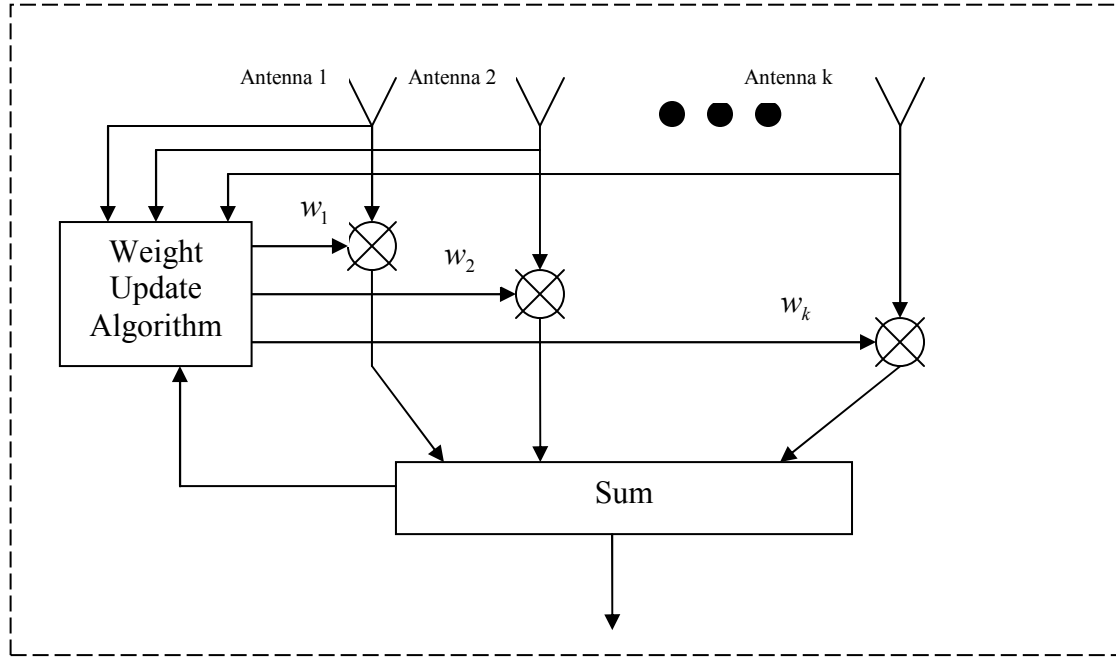


Figure 4: Simple adaptive antenna array system

One of the simplest approaches to reject the interference signals using an adaptive antenna array is to manipulate the antenna array to point nulls in the directions of interference signals. This approach is known as null steering and has been described in the literature review section.

Power inversion is one of the most effective techniques to reject both narrowband and broadband interference signals and is based on the null steering principle. Figure 5 shows a typical configuration of a power inversion array. $x(t) = [x_1(t) \ x_2(t) \ \dots \ x_n(t)]^T$ is a vector of output antenna waveforms. The output of the overall array can be written as $e(t) = d(t) - x^T(t)w(t)$, where $d(t)$ is the reference and $x(t)$ is the array of auxiliary elements.

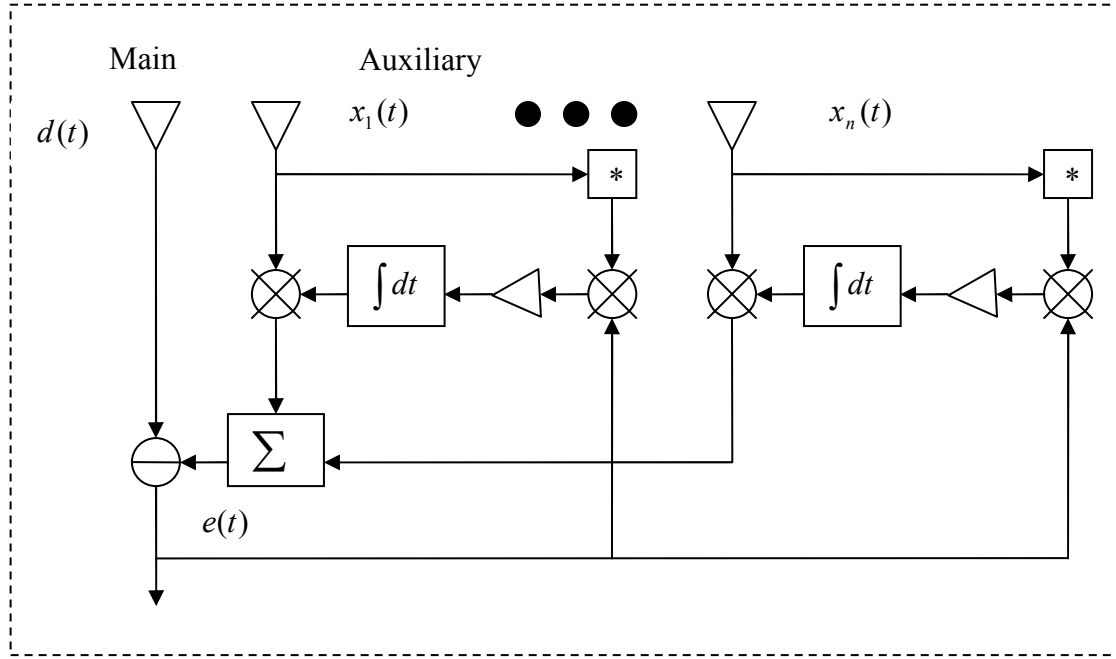


Figure 5: Adaptive antenna array by power inversion

The idea is to adjust the complex array weight vector to minimize the average power of the error signal, $e(t)$. As a result, the signal components from the main antenna with strong correlation with the auxiliary antennas are eliminated. The GPS signal is below the noise floor when it reaches the Earth surface. It is too weak to trigger the nulling process. However, once a null is formed, all signals in the nulling directions will be suppressed, including GPS signals.

In the discrete time domain, the average error signal power can be written as:

$$E\{e^2[k]\} = E\{(d[k] - y[k])^2\} = \sigma_d^2 - 2w^T p + w^T R w \quad \text{Equation 7 [4]}$$

In the above equation, σ_d^2 represents the average energy received by the main antenna, $R = E[x(n)x^H(n)]$ which is the correlation matrix of input data and $p = E[d(n)x^H(n)]$ is the cross-correlation vector between the input data and desired signal. An optimum weight vector exists that reduces the average error signal power to its minimum. It can be shown that this optimum weight vector is the solution to Weiner Hopf equation [31]:

$$w = R^{-1} p \quad \text{Equation 8 [4]}$$

One of the main advantages of using the power inversion method is that interference mitigation can be achieved without knowing the structures or directions of jamming

signals or the desired signals. This is one of the most desired properties for UAV applications, as in most situations, prior knowledge of interference is not available.

Null steering has been simulated in MATLAB. The array is once again setup according to Figure 1 with a half wavelength space between the two sensors. This is also the same setup for the anti-jamming unit. An interference signal is incident upon the array at broadside with amplitude of 10 units. To each sensor has been added independent white noise with power of 0.001 units squared. The optimum weight vector has been calculated according to Equation 8 and the error signal power obtained by this solution is plotted in Figure 6.

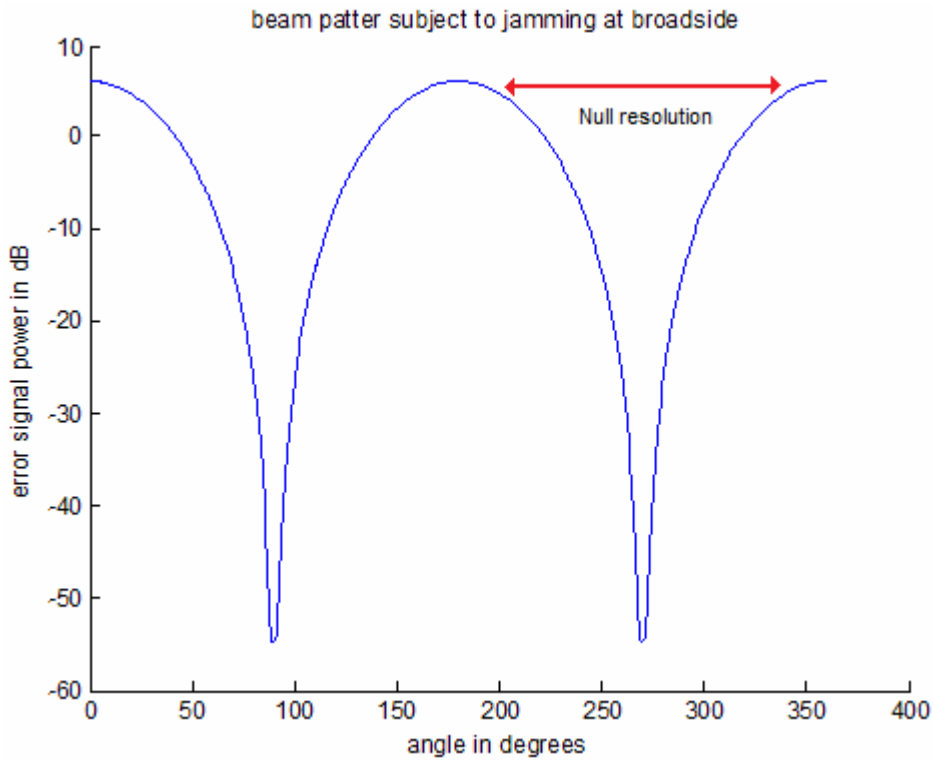


Figure 6: Null steering beam patten subject to broadside jamming

The above plot clearly shows that the optimum solution causes the array to arrange itself to direct a null in the interference direction of 90° . As a consequence of the symmetric structure of the array, this angle is ambiguous to the array at a second direction of 270° . Therefore a second null is also produced in this direction. The depth of the null is dependent on the resolution of simulated angle. In practice, this is often limited by the system dynamic range. As the array only has two antenna elements, the resulting nulls are particularly wide. At 106° , which is 16° away from the nulling angle of 90° , the error signal power has been attenuated by 20dB compared with its

peak value of approximately 6dB. At 150°, 60° away from 90°, the error signal power is 3dB less than its peak value. This implies that the system has a nulling(3dB) bandwidth of 120°. The same situation applies to the second null at 270°.

A polar plot of the error signal power is shown in Figure 7 below. This can be considered as the antenna reception pattern of the array. The onboard receiver integrated together with the anti-jamming unit is μ Patch 101 designed by Faxtrax Ltd. The maximum tracking sensitivity of this receiver is -180dBW. Under normal weather conditions, the minimum expected GPS signal strength is -160dBW. Therefore the receiver can afford to suffer at least 20dB attenuation before it loses track. The margin where 20dB or more attenuation was caused by the nulls has been marked in pink in Figure 7. In this region, the receiver is not able to track any satellites. The size of this region is approximately 40° for each null, which together is 22.2% equates to the unit circle in this 2D plot. However, if the nulling region is examined in 3D, a cone shape will be obtained for each null.

polar plot of beam pattern subject to jamming at broadside

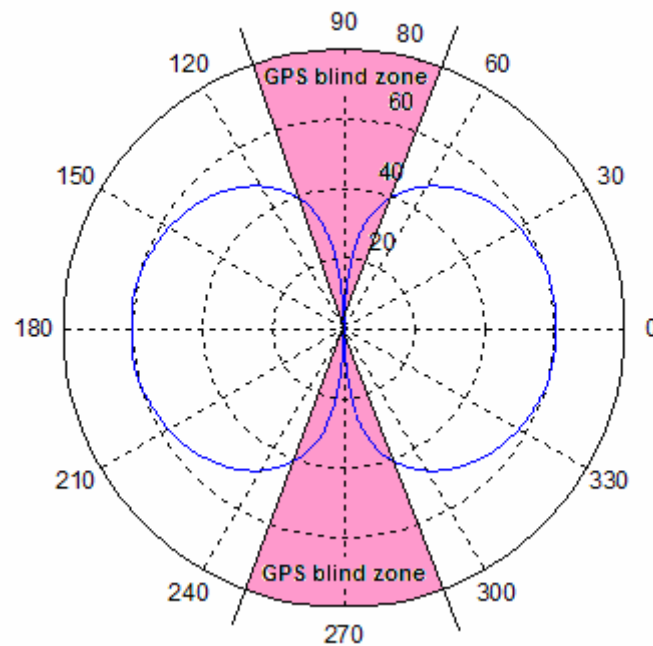


Figure 7: Null steering beam pattern subject to broadside jamming polar plot

However, broadside jamming is the worst case scenario for nulling resolution. As the jamming angle moves towards the end fire direction, the nulling resolution becomes sharper. Consider the polar plot of error signal subject to end fire jamming in Figure 8. In this scenario, the GPS blind zone is approximately 7.5° for each null which

together equates to 4.17% of the unit circle. In practice, additional antenna elements can be used to improve nulling resolution.

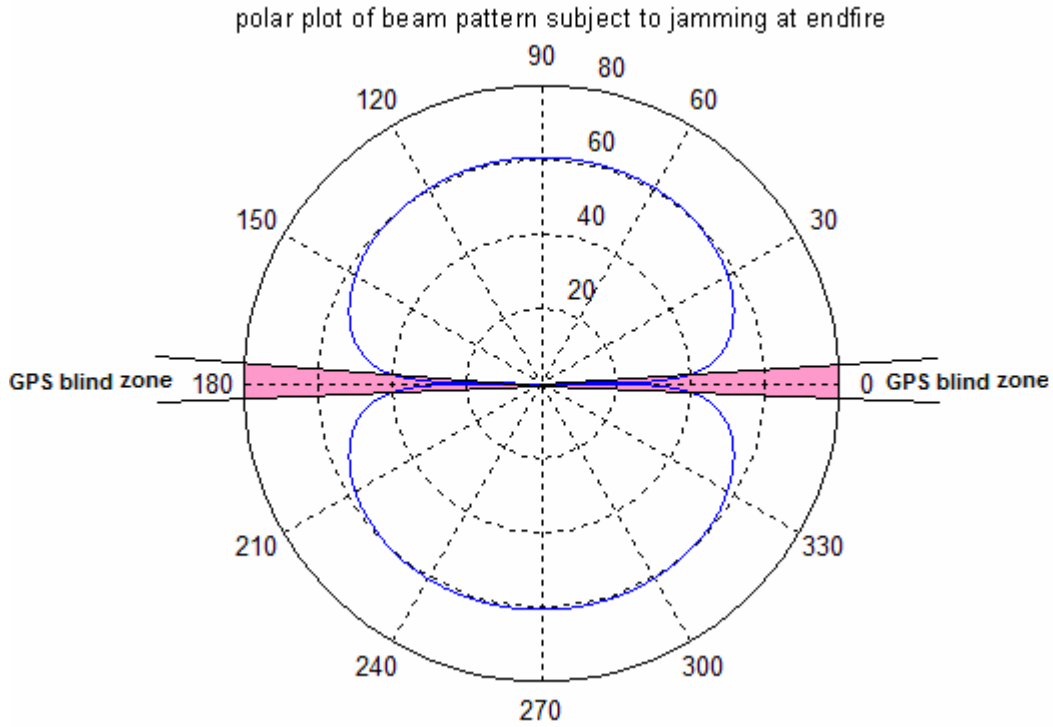


Figure 8: Null steering beam pattern subject to end fire jamming polar plot

3.3 Steepest Descent and LMS Algorithm

Many algorithms that have been developed in recent years to approximate the Wiener Hopf solution. These algorithms are often recursive so the weight vector can continuously adapt to a changing RF environment. One such search algorithm is known as steepest descent, which finds the solution to some objective function constructed based on the error $e(n)$. It starts with an initial guess for the weight vector and forms a better guess iteratively by taking a small step μ each time in the direction of negative gradient of the error surface. The idea of the steepest descent algorithm can be represented by using the following two equations, where $w(n)$ is the n^{th} iteration of the weight vector.

$$w(n+1) = w(n) + 2\mu E[x(n)e(n)] \Rightarrow w(n+1) = w(n) - 2\mu(Rw(n) - p) \quad \text{Equation 9}$$

In the above equations, $E[\]$ represents the ensemble average.

The steepest descent algorithm will indeed converge to the optimum Weiner solution if the exact gradient vector, defined by $Rw - p$, is obtained at each iteration, and if a suitable step-size parameter is chosen. However, in practice, the gradient vector cannot be obtained as it requires the prior knowledge of both the covariance matrix of the input data (R) and cross correlation vector between the input signal and desired signal (p). Consequently, the gradient must be estimated from the available data. One such approach is the Least Mean Square (LMS) algorithm.

The LMS algorithm uses $x(n)e(n)$ instead of its ensemble average as an estimate of the gradient vector. This reduces the LMS algorithm to:

$$\hat{w}(n+1) = \hat{w}(n) + 2\mu e(n)x(n), \text{ where } e(n) = d(n) - y(n) \quad \text{Equation 10}$$

As the above equation shows, the LMS algorithm is very simple. It requires neither measurements of the relevant correlation functions nor matrix inversion. For an N^{th} order digital filter, it requires $2N+1$ multiplications and $2N$ additions for each iteration to calculate the filter output [3].

Figure 9 illustrates how power minimization and the LMS algorithm can be applied to the anti-jamming unit. The desired signal $d(n)$ is the input signal from the reference channel, while the auxiliary antenna with three tap delays form the input signal vector $x(n)$ to the LMS algorithm.

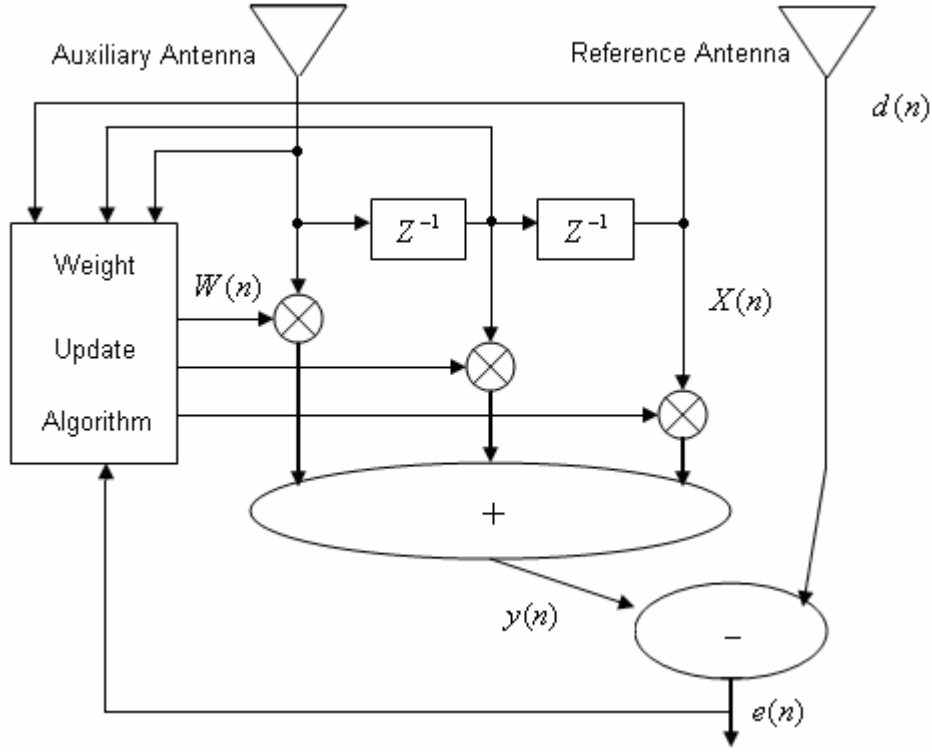


Figure 9: Block diagram of LMS algorithm

If w_o is the optimum solution of the Wiener filter and $e_o(n)$ is the corresponding estimation error produced, then the error signal of the LMS algorithm $e(n)$ can be re-written as[33]:

$$e(n) = d(n) - w_o^H x(n) + \varepsilon_o^H(n)x(n) \approx e_o(n) + \varepsilon_o^H(n)x(n) \quad \text{Equation 11}$$

In the above equation, $\varepsilon_o(n)$ is the zero order error-weight vector of the LMS algorithm. According to Butterweck's iterative procedure [33], it can be proven that

$$\varepsilon_o(n+1) = (I - \mu R)\varepsilon_o(n) - \mu x(n)e_o^*(n) \quad \text{Equation 12}$$

To further analyse the behaviour of the LMS algorithm, apply the unitary similarity transformation to the correlation matrix R . For example:

$$Q^H R Q = \Lambda \quad \text{Equation 13}$$

In the above equation, Q is the unitary matrix whose columns constitute an orthogonal set of eigenvectors associated with the eigenvalues of the correlation matrix R denoted by λ , and Λ is a diagonal matrix consisting of these eigenvalues. Defining

$$v(n) = Q^H \varepsilon_o(n) \quad \text{Equation 14}$$

For a digital filter of length M , the M eigenvectors represent the M natural modes of the feedback loop and consequently can be used to determine the transient response of

the feedback loop and hence the filter. According to Equation 12, the k^{th} natural mode of the transient response can be written as

$$v_k(n+1) = (1 - \mu\lambda_k)v_k(n) + \phi_k(n) \quad \text{Equation 15}$$

In Equation 15, $\phi_k(n)$ is often known as stochastic force [31, p265]. Therefore the error signal can be once again rewritten as:

$$e(n) \approx e_o(n) + v^H(n)Q^H x(n) \quad \text{Equation 16}$$

According to the above equation, the convergence of the error signal in mean is only dependent on the convergence of the natural modes of the LMS filter, which are denoted by v_k . It is shown in [31]

$$E[v_k(n)] = v_k(0)(1 - \mu\lambda_k)^n \quad \text{Equation 17}$$

Considering the above equation, $v_k(0)$ is the initial value of the k th natural mode of the LMS filter. To guarantee convergence of the mean, the exponential factor $(1 - \mu\lambda_k)^n$ must be reduced as the time step n increases. Therefore, a necessary condition for the mean convergence of the LMS algorithm is

$$-1 < 1 - \mu\lambda_k < +1, \text{ for all } k, \Rightarrow 0 < \mu < \frac{2}{\lambda_{\max}} \quad \text{Equation 18}$$

However, convergence in the mean does not guarantee the stability of such convergence. Consider the following two examples illustrated by Figure 10. In the right hand side plot, the error signal does converge in mean but becomes unstable towards the end of the iterations. It is more desirable to converge in a mean square sense, as illustrated in the left hand side plot. In this situation, not only the mean of the error signal approaches its optimum value, but the mean square of the error signal also reduces.

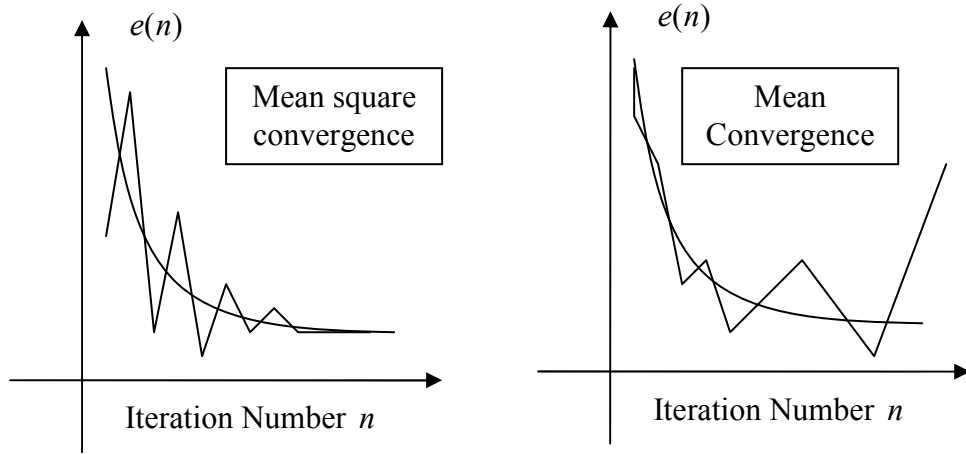


Figure 10: Mean square convergence vs. Mean convergence

The mean square error signal is equal to

$$J(n) = E[|e(n)|^2] = E[(e_o(n) + \varepsilon_o^H(n)x(n))(e_o^*(n) + x^H(n)\varepsilon_o(n))] \\ \approx J_{\min} + E[\varepsilon_o^H(n)R\varepsilon_o(n)] \quad \text{Equation 19}$$

The excess mean square error is defined as the difference between the converged mean square error by LMS and the minimum mean square.

$$J_{ex}(n) = J(n) - J_{\min} = E[\varepsilon_o^H(n)R\varepsilon_o(n)] \quad \text{Equation 20}$$

By applying the unitary similarity transformation on R , Equation 20 can be reduced as follows:

$$J_{ex}(n) = E[\text{tr}(v^H(n)Q^H RQv(n))] = \sum_{k=1}^M \lambda_k E[|v_k(n)|^2] \quad \text{Equation 21}$$

In the above equation, M is the length of the digital filter. It can be shown that [31]

$$E[|v_k(n)|^2] = \frac{\mu J_{\min}}{2 - \mu \lambda_k} + (1 - \mu \lambda_k)^{2n} \left(|v_k(0)|^2 - \frac{\mu J_{\min}}{2 - \mu \lambda_k} \right) \quad \text{Equation 22}$$

By observing Equation 21 and 22, the exponential factor $(1 - \mu \lambda_k)^{2n}$ will decay to zero over time, if the mean convergence condition is satisfied [31]. And when $n \rightarrow \infty$,

$$J_{ex}(\infty) = \mu J_{\min} \sum_{k=1}^M \frac{\lambda_k}{2 - \mu \lambda_k} \quad \text{Equation 23}$$

To guarantee mean square convergence of the LMS algorithm requires, in addition to satisfying Equation 18, that [31]

$$\sum_{k=1}^M \frac{\lambda_k \mu}{2 - \mu \lambda_k} < 1 \quad \text{Equation 24}$$

The misadjustment of the LMS filter is frequently used to measure the performance of the filter. It is defined as the ratio of the steady-state value of the excess mean square error to the minimum mean square error and for sufficiently small step sizes:

$$M = \frac{J_{ex}(\infty)}{J_{min}} \approx \frac{\mu}{2} \sum_{k=1}^M \lambda_k \Rightarrow M = \frac{\mu}{2} \times (\text{total tap-input power}) \quad \text{Equation 25}$$

It has been shown that the mean square error exponentially decays at a rate of $1/\tau_k$

where τ_k can be estimated by

$$\tau_k = \frac{-1}{\ln(1 - \mu\lambda_k)} \approx \frac{1}{2\mu\lambda_k} \quad \text{Equation 26}$$

Define the average eigenvalue of the correlation matrix R as

$$\lambda_{av} = \frac{1}{M} \sum_{k=1}^M \lambda_k \quad \text{Equation 27}$$

The average convergence rate of the LMS algorithm can then be written as

$$\tau_{mse,av} = \frac{1}{2\mu\lambda_{av}} \quad \text{Equation 28}$$

From the above analysis, it can be concluded that the misadjustment is linearly proportional to the stepsize and total tap-input power. Therefore, using more taps in the auxiliary channel will consequentially increase the misadjustment factor. A smaller stepsize can be used to compensate for this disadvantage. On the other hand, smaller step size will result in longer convergence time. Therefore, an appropriate stepsize should be chosen when designing the algorithm. In practice, the stepsize is often chosen such that the misadjustment is less than 0.1. [31, p271]

To understand the actual behaviour of null steering with tap-delay line, the error signal power subject to jamming has been simulated in MATLAB as a function of both steering angle and digital frequency. The results are shown by a colour image in Figure 11. A sine wave interference at carrier frequency with amplitude of 10 units is incident upon the array at 60° . Independent white noise with power of 0.001 units squared is added in each antenna separately. Based on the above conditions, the weight of the reference antenna is set to be 1 and the optimum weight vector of the tap-delay line is calculated according to Equation 8 as a Weiner filter. This weight

vector remains fixed and the error signal when a signal is incident upon the array over the range of steering angle and digital frequency as shown in Figure 11.

By observing Figure 11, the two “Λ” shaped light bands on this image are a result of the symmetric structure of the array. At 0 in digital frequency, the deepest null occurs at jamming direction of 60° and the ambiguous angle of 120° as expected. As the digital frequency changes, these null positions also change and at the same time the depth of the nulls reduces. At a digital frequency of approximately 0.075, the null position of the jamming signal moves to 90° and the ambiguous null appears at 270° , which initiates the second “Λ” band on the right hand side of the image.

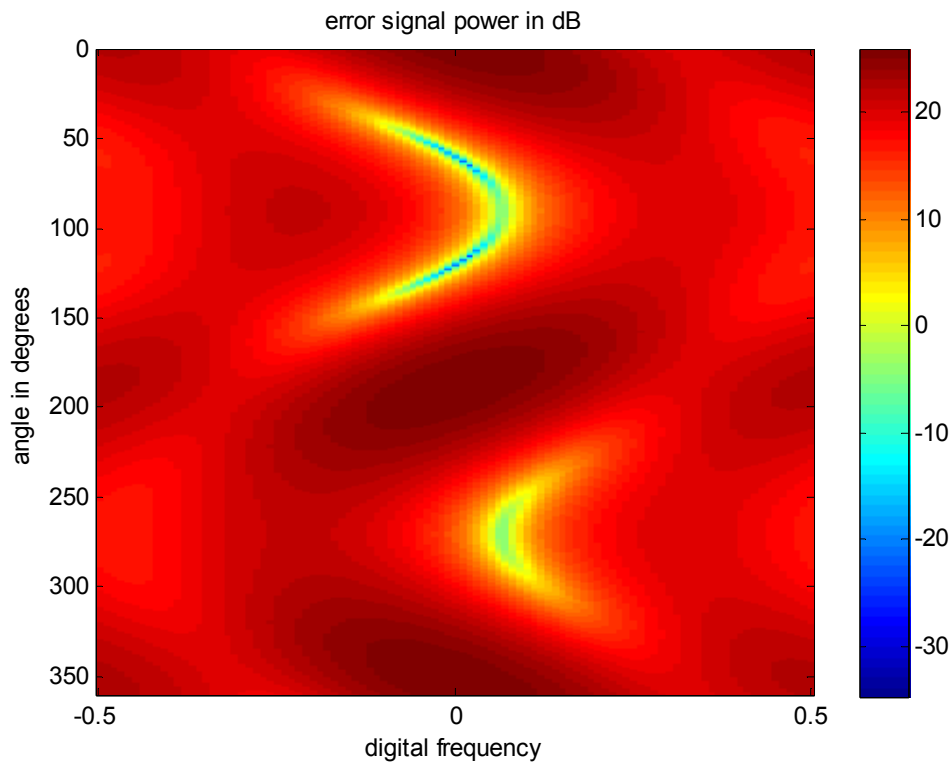


Figure 11: Error signal power subject to 60° jamming-digital frequency vs. angle plot

Figure 11 clearly shows that the depth of null changes as the digital frequency changes. This implies that by adding the tap-delay line, the adaptive antenna array has become not only directionally sensitive but also frequency selective to jamming signals. Signals incident on the array from the jamming direction or the ambiguous angle of the jamming direction will only be cancelled if their frequencies are close to the jamming signal frequency.

The steering angle against digital frequency plot has also been constructed in 3D and is plotted in Figure 12. This plot makes it visually easier to understand the relationships between steering angle, digital frequency and converged error signal power.

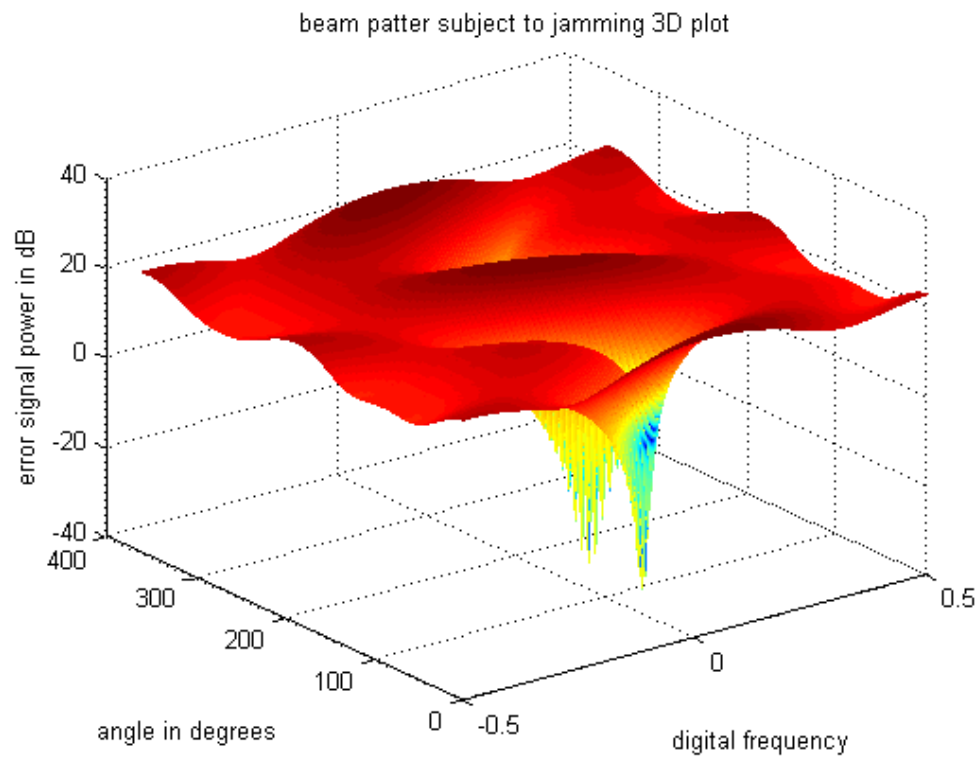


Figure 12: *Beam pattern subject to 60° jamming 3D plot*

Chapter 4

Anti-Jamming Unit Hardware Design

This chapter describes the system design of an anti-jamming unit. The performance specification and the theoretical AJ margin of the unit will be discussed. The anti-jamming unit consists of three main components and their detailed structures and main functions are also given in this chapter.

As a prototype, a two-element adaptive antenna array is implemented. As a result of having only two elements, this anti-jamming unit is only able to handle a single source of broadband interference at any instant. A tap delay line has been implemented on the auxiliary channel, aimed at reducing the mismatch between the RF front ends. This may provide the unit with some additional narrowband interference handling capability at the same time. However, this scenario has not been considered during the design and testing process, as it is not the primary intention of this project.

To further reduce the design complexity, the final product will only be applied in commercial GPS C/A code applications. Therefore, the effective operating bandwidth has been reduced to only 2MHz. This operating bandwidth reduction has simplified the optimisation process of many design parameters, and at the same time, increases the achievable AJ margin of the unit.

4.1 System Design and Performance Specification

A systematic view of the two-element adaptive antenna array is shown in Figure 13. It consists of two duplicated antenna channels, a digital processing unit and RF up and down conversion boards. The main purpose of the antenna channels is to receive analogue signals at a GPS frequency of 1.57542GHz and down-convert them to an IF frequency suitable for digitisation. Therefore, each antenna channel contains one

patch antenna for receiving the signal and an RF front end for down conversion purposes. The IF frequency has been chosen to be 50MHz based on the 200MHz sampling rate of the ADC inside of the digital processing unit. Another reason for choosing this value is due to the availability of commercial RF components at this frequency, so that the RF front end performance can be easily optimized.

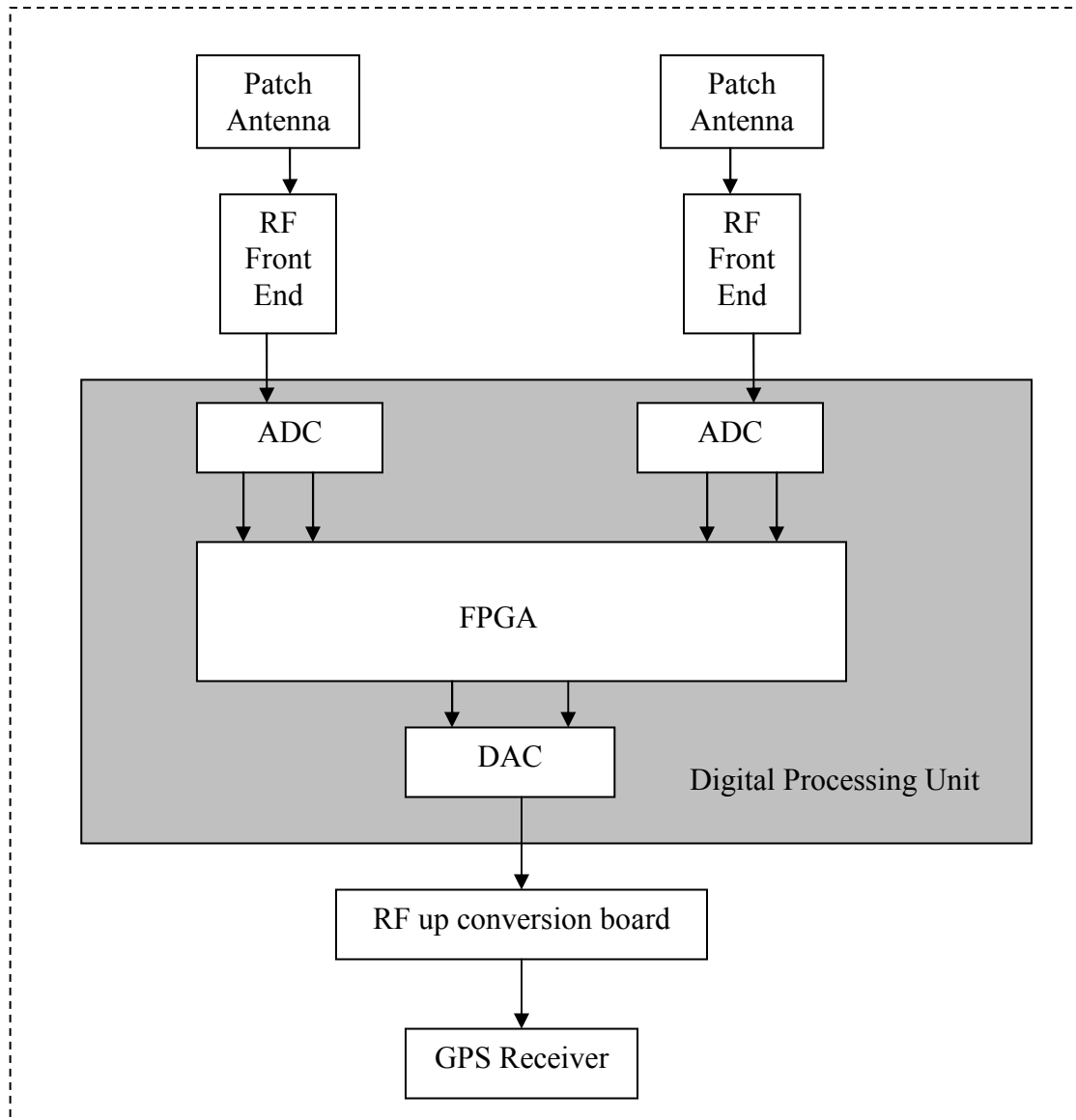


Figure 13: Systematic view of overall structure

The null-steering algorithm, which provides the interference mitigation ability for the unit, can be implemented in the digital, analogue, or combined digital-analogue domain. However, a fully digital implementation often results in a high AJ margin and fast convergence rate [9]. To speed up the prototyping process, a commercially available FPGA module was used to implement the digital signal processing. It also

contains two independent ADCs for digitizing IF signals from two separate antenna channels. As the IF frequency is 50MHz and the effective operating bandwidth is only 2MHz, the digital processing unit performs a second stage down conversion, while decimating, filtering and splitting the signal into in phase (I) and quadrature (Q) for complex base band processing. The LMS null-steering algorithm is implemented within the FPGA chip, and the processed signal is then converted into its analogue form by using a DAC, also on the FPGA module. This analogue signal is then up-mixed back to GPS operating frequency. The “up-mixing” process provides the unit an “add-on” characteristic, that it may be used for any existing GPS receiver without any modification.

4.2 RF Front End Design

The main purpose of having an RF front end is to down-convert the received GPS signal to an intermediate signal frequency suitable for pass-band digitization. The frequency of this intermediate signal is normally chosen to be half of the Nyquist sampling frequency. This will provide the largest transition bandwidths for the digital filter prior to the anti-jamming algorithm. Besides down-conversion, the RF front end also performs filtering and amplification of the received signal to meet the system selectivity and sensitivity requirements. As the ADC is part of the digital processing unit, its input signal power range cannot be customized or reconfigured. Therefore, the RF front end must be designed to match the dynamic range of the ADC.

Figure 14 shows the structure of the RF front end. It consists of amplifiers, filters and a mixer to ensure the suitability of the processed signal for digitization. All the components are linked in a cascaded chain as Figure 14 illustrates. The components names are listed in Table 1 and their details are given in Chapter 5. The order in which these components appear in the chain, and their individual performance characteristics determine the overall RF front end compatibility with the ADC.

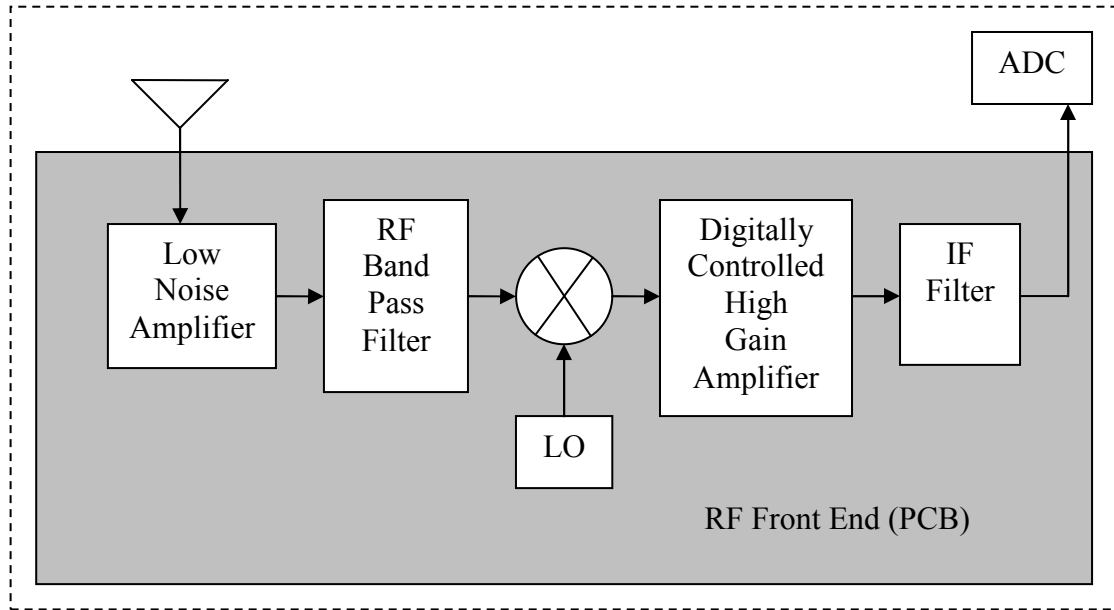


Figure 14: Systematic diagram of RF front end

The Low Noise Amplifier (LNA) is the first component in the cascaded chain. It is placed directly after the patch antenna to minimize the overall system noise figure. The signal is then band limited using an RF band pass filter before it is down mixed to an IF frequency. The RF filter is designed with 20MHz pass bandwidth. To reduce the size of the RF front end and simplify the implementation process, a ceramic resonator specifically designed for GPS applications has been chosen to provide the RF filtering. As mentioned earlier, the IF frequency has been chosen to be 50MHz. Therefore, a Voltage Controlled Oscillator (VCO), which oscillates at 1.52542GHz, is used as a Local Oscillator (LO) and its output is fed to the LO input of the mixer. A digitally controlled high gain amplifier is placed after the mixer as the final stage gain control. This amplifier provides 33dB maximum amplification with 1.5dB resolution adjustable gain ability. By using this amplifier, the overall system gain can be adjusted very precisely. It also allows Automatic Gain Control (AGC) to be implemented in the system. As the current unit is a prototype, an AGC feature is not yet implemented. However, its significance is discussed later on in this chapter. Finally, an IF BPF is applied at the last stage of the cascaded chain. This filter is implemented by discrete inductor and capacitor components and its bandwidth is chosen to be 20MHz, which is much wider than the actual GPS operating bandwidth of 2MHz. By doing so, an almost linear passband response of the filter can be achieved. The wider pass bandwidth also reduces the sensitivity of the filter response to individual discrete component variation. Therefore the mismatch between the RF

front ends will be reduced. This will further maximize the overall anti-jamming range. A detailed analysis of the effect of RF front end mismatch can be found in Chapter 5. The extra out-of-band noise will be filtered out by the digital filter, which is implemented on the FPGA.

Table 1 shows the RF performance of each individual component chosen in this design. The high gain amplifier has the ability to control its gain by using 4 digital input control pins. Its maximum output gain is 33dB. In this case, it has been set to 27dB. The ceramic RF BPF has a standard insertion loss of 1.5dB. As it is not an active device, it is sensible to assume that the filter has linear response over the practical input power range. Therefore, its Input 3rd Order Interception Point (IIP3) point has been given a value of 100dBm, so that the non-linearity of this component is not considered in the calculation.

RF components	Gain dB	Noise Figure	OIP3 (output)	IIP3 (input)	Operating frequency
LNA (HMC374)	13dB	1.6dB	37.8dBm	24.8dBm	1.575 GHz
RF BPF (CER0005A)	-1.5dB	1.5dB	100dBm	100dBm	1.575 GHz
Mixer (HMC421QS16)	9dB	11dB	28dBm	19dBm	IF at 50MHz
High Gain Amplifier (LT5514)	27dB	13.7dB	47dBm	20dBm	50MHz

Table 1: RF components parameters

4.3 RF Front End Dynamic Range

The RF front end spurious-free dynamic range (SFDR) represents the absolute input power range to the RF front end without any distortion. It is defined as the ratio of the minimum detectable signal (MDS) to the signal whose third order distortion is just above the noise floor, and can be calculated using Equation 29 [5]. In this equation, MDS is measured at the receiver input and is usually 3dB above the noise floor, and IIP3 is the cascaded IIP3 of the entire RF front end chain.

$$SFDR = \left(\frac{IIP3}{MDS} \right)^{2/3} \quad \text{Equation 29}$$

The system dynamic range is constrained by the dynamic range of its sub-components. Due to the high input dynamic range of the ADC, the dynamic range of the RF front end is considered to be the main factor limiting the system dynamic range. As the overall anti-jamming range is fundamentally limited by the system dynamic range, maximizing the RF front end dynamic range will directly maximize the unit's anti-jamming ability. To be able to meet the 40dB anti-jamming range requirement, the SFDR of the RF front end must be at least 40dB. This directly constrains the cascaded IIP3 and MDS performance. The MDS and cascaded IIP3 are calculated in the remainder of this section to give the overall dynamic range of the RF front end.

In an RF system, the signal will be competing with an ever present random signal or noise. This limits the performance of all receivers. External noise including natural and man-made noise is present at the input of the RF system and will be introduced into the system by the receiver antenna. Each RF component also contributes noise due to its non-linearity and random thermal fluctuations [7]. An important quantity used to assess the circuit performance is the noise factor. It is also known as Noise Figure (NF) if it is expressed in dB. Equation 30 shows the fundamental definition of the noise factor [31].

$$F = \frac{S_{input} / N_{input}}{S_{output} / N_{output}} \quad \text{Equation 30}$$

where S and N represent signal and noise power correspondingly. The noise factor of a two-port network is defined as the ratio of the output noise power to the output noise power of an ideal (noiseless) two-port network for which the thermal noise source is at room temperature (290K) [6]. Hence the noise factor of an RF system can be determined by measuring the output noise power when no input signal is applied.

For cascaded analogue components, the overall system noise factor can be found by using Friis' formula [5]:

$$F_{total} = F_1 + \frac{(F_2 - 1)}{G_1} + \frac{(F_3 - 1)}{G_1 G_2} + \dots \quad \text{Equation 31}$$

where F_i and G_i are the noise factor and gain of device i in linear units respectively.

According to Equation 31, the noise contributions from the subsequent terms after the first component are divided by the gain products. For a system with reasonable gain, they will be negligible. Therefore, the overall system noise factor can be approximated by F_1 . For this reason, a high gain low noise amplifier is usually the first component of a cascaded analogue system. By using Equation 31, the cascaded noise factor has been calculated to be 1.77, which is 2.48dB equivalently.

The introduction of amplifiers and mixers into the architecture of the RF front end indicates that there will be a non-linear effect due to the non-linearity of individual RF components. This non-linearity is often illustrated mathematically by modelling the transistor collector or drain current I_o , which is a function of the input voltage, denoted as V_{in} , across the base or gate and can be expanded as a polynomial series [38]:

$$I_o = I_Q + g_m V_{in} + g_{m2} V_{in}^2 + g_{m3} V_{in}^3 + \dots \quad \text{Equation 32}$$

In the above equation, I_Q is the base or gate current and g_m is the transconductance of the device. The multiple non-linear terms in this equation are realized by a multitude of harmonics at the output of transistors. These harmonics are classified depending on the power of the actual non-linear term. For example, the harmonics caused by the cubic term are referred to as 3rd order intermodulation products or 3rd order harmonics.

When a two-tone signal is applied at the input, i.e. $V_{IN} = E_1 \cos \omega_1 t + E_2 \cos \omega_2 t$, it can be shown that the output current at frequency ω_1 is given by the following equation [38]:

$$I_{\omega_1} = g_m E_1 + \frac{3g_{m3} E_1^3}{4} + \frac{3g_{m3} E_1 E_2^2}{2} \quad \text{Equation 33}$$

As g_{m3} is in general negative, when $E_2 = 0$, the current component of $\frac{3g_{m3} E_1^3}{4}$ will subtract directly from the linear term $g_m E_1$ causing power compression [37].

When $E_2 = E_1 = E$, the 3rd order term takes the magnitude of $\frac{9g_{m3} E^3}{4}$, and compresses the linear fundamental component more quickly than any other order.

Therefore during the receiver design process, most often only 3rd harmonic power compression is considered.

When the output power is 1dB below the fundamental output power, the condition is known as 1-dB compression and the output power is referred to as the 1-dB compression point. This is a commonly used measure of the power handling capability of a device. It also indicates the output power level at which the device ceases to be nominally linear. The idea is illustrated in Figure 15.

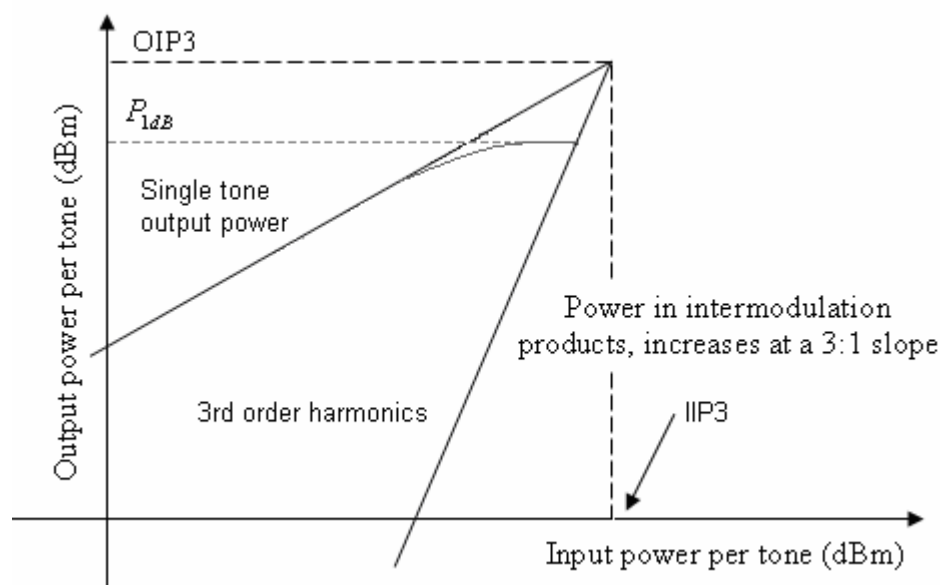


Figure 15: IP3 illustration for a two tone input signal

The non-linearity of RF components not only causes power compression at its fundamental frequency but also causes inter-modulation products within the bandwidth that cannot be filtered out. This gives another commonly used measure of the power handling capability of a device, the IIP3. It is defined as the extrapolated input power level per tone that would cause the output power of the third-order inter-modulation products of a two-tone signal to equal the single tone linear output power. The resultant output power at that point is the output third order intercept point, OIP3. This idea is illustrated in Figure 15. The IIP3 point can be determined by using two tones with equal power levels. It is an important figure for receiver design as it marks the upper limits of the overall SFDR. Therefore maximising the IIP3 will also maximise the SFDR.

The cascaded IIP3 can be calculated by using the following equation [5]:

$$\frac{1}{IIP_3} = \frac{1}{IIP_{31}} + \frac{G_1}{IIP_{32}} + \frac{G_1 G_2}{IIP_{33}} + \dots \quad \text{Equation 34}$$

where G_i and IIP_{3i} are the gain and input intercept point of device i respectively. By using this equation, the overall system IIP3 has been calculated to be -1.14dBm based on the parameters in Table 1. By using Equation 29, this implies that the theoretical SFDR of the RF front end based on the selected components is 62dB.

4.4 IF Stage Gain

As has been described, the cascaded gain of the RF front end, which includes the IF stage gain, is used in the calculation of both the MDS and IIP3. Changing the gain will thus cause both of these values to change, which will in turn affect the dynamic range. As the input dynamic range of the ADC is fixed, it is desirable to design an RF front end which amplifies the input signal to be near the full scale input power range of the ADC. This will ultimately fully utilize the overall system dynamic range. To achieve this, a variable IF stage gain can be implemented based on the input signal power. This technique is known as Automatic Gain Control (AGC).

AGC is a very effective technique to increase the useful dynamic range of a receiver. It is widely used in broadband communications. AGC sacrifices the MDS performance when a large input signal power is detected in order to prevent a loss in dynamic range due to non-linear (third order) distortion components resulting from RF component saturation. This is achieved by reducing the IF stage gain once the input signal reaches a certain power level. However, the impact of doing this on the total system dynamic range and SNR is not directly obvious and involves certain trade-offs which will be considered next.

The dynamic range of the RF front end for two gain settings is illustrated in Figure 16. The concept of AGC and its impact are also explained.

NOTE:
This figure is included on page 55
of the print copy of the thesis held in
the University of Adelaide Library.

Figure 16: *Illustration of RF performance of variable gain case [5]*

Two different gain settings have been considered in this diagram. The blue plot represents normal operation and the red plot represents a reduction in the IF stage gain to reduce the power level of non-linear components and to prevent saturation. The output power levels of the fundamental and the 3rd order harmonics have been plotted against input signal power for both scenarios. For a fixed gain setting factor, the noise floor is fixed across the whole input range, and this idea has been illustrated by two horizontal dashed lines in Figure 16. These two dashed lines will intersect the plots of output power levels of both the fundamental and the 3rd order harmonics power. The range in between these two points of intersection is in fact the input dynamic range. These two dynamic ranges have been shown as DR1 and DR2 in Figure 16. Hence, the total system dynamic range is the joint region of DR1 and DR2 and it has been shown in green. It is clear that the total system dynamic range has been increased and the amount of increase is proportional to the gain reduction factor.

There is a limit on how much the gain can be reduced. Reducing the IF stage gain is equivalent to inserting attenuators in the cascade chain. The most direct impact is an increase in noise figure and hence reduced sensitivity. This occurs if the total gain prior to any component becomes less than the noise figure of that component. The RF front end has to maintain a certain level of sensitivity for successful signal reception and an increase in noise figure will ultimately reduce the SNR of the GPS signal.

The gain reduction could potentially occur anywhere in the cascaded chain when a strong input power is present. However, reducing the gain at too early a stage of the cascaded chain could degrade system sensitivity. On the other hand, only the components after the gain reduction point in the cascaded chain are protected. Components prior to where gain reduction occurs will still experience the full input signal power. In terms of maximizing system dynamic range, it would be best to reduce the gain just before the component which limits the overall system IP3 point. At the same time, the noise figure should be re-examined with the reduced gain setting.

In this design, the AGC is achieved by the final digitally controlled high gain amplifier. It has been found that this amplifier is the critical component in the cascaded chain which limits the system IP3 point. Thus controlling the gain of this component is useful in maximising the total system dynamic range. To avoid a loss in overall receiver sensitivity, the maximum gain reduction is limited by:

- The noise figure of the amplifier: The noise figure of the amplifier increases proportionally to the gain reduction factor. To avoid degraded system sensitivity, the cascaded gain factor prior to the amplifier must exceed the noise figure of the amplifier after gain reduction.
- The MDS of the ADC: The MDS level at the output RF front end has to be above the MDS level of the ADC to avoid a loss in sensitivity.

If AGC is implemented on the unit, the DR can be potentially improved by 7dB according to the above criterion. This has been demonstrated in Figure 31 in Chapter 6.

4.5 Filtering Requirements

There are three stages of filtering that have been used to isolate the frequency range of interest. Two of the filters are allocated in the RF front end and one digital filter is implemented on the FPGA. Each of them serves a different purpose and they impact the system differently.

The first filter is at the RF stage between the LNA and mixer. Its main purpose is to isolate the input frequency range before down conversion. Because the filter is at an early stage of the cascaded chain, its insertion loss will contribute to the system noise figure the most beside the LNA and the cable loss to the antennas. Therefore, it is critical for this filter to have low insertion loss. Based on these requirements, a ceramic RF filter has been chosen due to its relatively small size and competitive performance. The filter is particularly designed for civilian GPS applications with a centre frequency of 1.57542GHz, a 20MHz pass bandwidth, and a 1.5dB insertion loss.

The second filter is at the end of the RF front end, just before the ADC, and serves as an anti-aliasing filter. To maximise the transition bandwidth of the digital filter, the IF frequency is chosen at 50MHz which is half of the Nyquist frequency. Therefore, the next aliasing frequency component caused by sampling is centred at 150MHz. Given the GPS bandwidth is 2MHz, this alias will occupy a frequency range from 149MHz to 151MHz. Hence the filter has to provide sufficient attenuation before 149MHz to prevent aliasing from occurring. This has also been demonstrated in Figure 18 in Chapter 5.

As the phased array requires two RF front ends in parallel, any mismatch between the IF filters will degrade the overall anti-jamming range exponentially. Therefore it is crucial to design the IF filters to have flat passband responses. As the operating bandwidth for GPS C/A code is 2MHz, the passband of the IF filter should be at least 2MHz. In practice it is often difficult to achieve a linear filter response over the entire pass band due to component variation. Hence, the IF filters have been purposely designed to have a 20MHz pass bandwidth, thereby improving the linearity of the response over the 2MHz bandwidth where the GPS operates in the middle of the passband.

There are a number of trade-offs in using this approach. The most obvious trade-off is a smaller transition bandwidth for the filter to cut-off at 149MHz. Therefore the filter design must be a compromise between a linear pass band response and sufficient stop band attenuation. The pass bandwidth of the IF filter is chosen to be 20MHz to ensure

more than 40dB attenuation at 149MHz. The second trade-off when using a wider IF pass band is that more noise will be presented to the ADC. As a consequence, the dynamic range of the ADC will be reduced for interference signals that cover the entire 20MHz bandwidth. However for in-band interference, the jamming power is concentrated in the central 2MHz bandwidth and the overall anti-jamming range will not be affected. Also, high power out-of-band interference signals within the 20MHz bandwidth will be passed through to the ADC and could cause the ADC to saturate. In this case, the AJ margin will be degraded.

The final filter is implemented in the digital portion of the unit, which serves as an anti-imaging decimation filter. The digital filter with more number of taps will provide more attenuation at the cut off frequency. However, this alternatively increases the area usage of the FPGA. In order to meet the FPGA area constraint, a reduced number of taps are used for the digital filter. For this reason, a wider transition bandwidth is necessary so the amount of attenuation at the cut off frequency is still sufficient to ensure the anti-jamming range is not reduced due to the aliasing components.

In this project, the ADCs are chosen to operate at 200MHz and the digital BPF is designed to have a decimation factor of 8, the final sampling frequency after this filter becomes 25MHz. As the actual GPS bandwidth is only 2MHz, theoretically a much larger decimation factor can be used. On the other hand, 25MHz sampling frequency will provide 25MHz transition bandwidth for the filter, so that more than 50dB attenuation can be achieved at 149MHz. This is the frequency where the next aliasing component occurs. The cost of doing so is that the LMS algorithm will run at a higher speed and therefore more switching power is consumed. In addition, as this digital filter is a complex filter, the I and Q signals generated by this filter are perfectly 90 degrees out of phase. Therefore the complex LMS algorithm can be applied and does not have to tolerate any phase error.

4.6 Summary

In this chapter, the system design principles of the anti-jamming unit have been described. The system design is primarily aimed to maximize the overall anti-

jamming range while maintain the small size and low power consumption characteristics of the unit.

As the digital processing unit is priority chosen, a customized RF front end has to be designed to match with its performance. The designed value of the RF front end dynamic range is 62 dB, which constrains the maximum achievable AJ range to 62dB. The sampling frequency of the ADC is 200MHz. Hence the IF has been chosen to be 50MHz. The RF front end has noise figure of 2.48dB with 20MHz pass bandwidth.

The digitally controlled high gain amplifier on the RF front end allows the AGC feature to be implemented. This will increase the total system dynamic range by 7dB. This value is calculated based on the measured performance of the RF front end. Further details can be found in Chapter 6. However, as the current unit is a prototype, the AGC feature is not yet implemented. Extra logic must be developed to control the gain of the amplifier. This feature is discussed as a possible future extension of the project.

Chapter 5

Hardware Implementation

As mentioned in Chapter 4, the antenna array consists of three main components. They are the RF front end, the digital processing unit and the RF up conversion board. The detailed implementation of these components and the overall system integration are described in this chapter.

After examining the system requirements, a DSP Heron-IO5 FPGA board by Hunt Engineering was chosen to serve as the digital processing unit. The FPGA module contains a 3 million gate Virtex 2 FPGA chip, which provides sufficient area for implementing the null steering algorithm and I/Q filtering. Two independent 200MHz, 12-bit ADCs and one DAC have also been integrated as part of the FPGA module. This allows the two antenna channels to be sampled separately. Both RF front ends and the up conversion board are based on a customized design and are implemented using PCB technology. The connections between the components are achieved with SMA connectors.

5.1 Analogue Front End

The RF front end described in the previous section is implemented by using two-layer PCB technology. Surface mount components are soldered on the top layer and the bottom layer is used as a ground plane for easier signal routing and Electromagnetic Compatibility (EMC) control. The components were chosen based on their RF performance such that the sensitivity and selectivity requirements are satisfied. However, it is also desirable to keep the total PCB area as small as possible. Therefore, the required complexities of the biasing and matching circuits for each component have also been considered. The total area of each analogue front end PCB is 2.7cm×6.0cm. A systematic block diagram is shown in Figure 14 in Chapter 4.

The details of each component used in the RF front end are described as follows. The main performance characteristics of each component described in this section are shown in Table 1 in Chapter 4. The HMC374 by Hittite has been chosen as the LNA due to its low noise figure and high gain. The ceramic RF filter is manufactured by CTS Pty Ltd. This surface mount ceramic filter was specifically developed for use in commercial GPS applications. It has the advantages of low insertion loss and small size. The mixer is a Hittite HMC421QS16. It not only provides the down conversion functionality but at the same time provides 9dB of conversion gain with a 19dBm IP3 point. The digitally controlled high gain amplifier is the LT5514 manufactured by Linear Technology. This amplifier provides over 30dB gain and 47dBm OIP3. It also includes a digitally controlled variable attenuator so that AGC can be easily implemented. However, the drawback of using this amplifier is its high power consumption, and hence it requires a heat sink mechanism. Each analogue front end also contains two 5V regulators for power supply and distribution purposes.

As the output of the high gain amplifier and the input of the ADCs are both differential signals, the IF filter was implemented using a balanced structure to accept differential input and output. A 3rd order Chebychev balanced filter has been implemented using discrete resonant circuits. The balanced structure provides a differential output, which allows the filter to be connected directly to the differential input of the ADC. On the other hand, using a balanced structure filter requires twice as many discrete components for the resonant circuits, which increases the total PCB area. By using the same PCB area, a higher order single-ended filter could be achieved, potentially resulting in a better filter if a non-differential input were provided to the ADC.

The two analogue front ends are shielded individually with aluminium. The RF up conversion board and LO and its distribution board are also aluminium shielded. To reduce the total weight of the unit, the aluminium shields have been oriented back to back so that they share some of the aluminium blocks. The shielding protects the PCBs from external EM radiation and cross talk, and hence gives more reliable RF performance. The aluminium is also used for heat sink purposes due to its good ability to conduct heat.

Figure 17 shows the top view of the analogue part of the anti-jamming unit. The aluminium shielding can be clearly observed in this picture. It isolates the three PCB boards. Two identical RF front ends have been allocated on the right hand side of the shielding and the up-converter board is placed on the left most side.



Figure 17: Top view of the anti-jamming unit

5.2 Analogue to Digital Converter (ADC)

Two ADC chips are integrated with the FPGA on the HERON-IO5 DSP board. They are the AD9430 manufactured by Analogue Devices Pty Ltd. The ADC chip is able to transform the analogue signal into a 12-bit 2's complement number at a maximum sampling frequency of 200MHz. It takes a differential input signal for maximum input dynamic range. Both ADCs are driven at 200MHz. This provides 25MHz complex digital bandwidth for the anti-aliasing digital filters to operate at.

During the digitization process, only a finite number of bits can be used to represent the analogue signal, which introduces some inaccuracies. These inaccuracies are referred to as quantization noise. It can be shown that the dynamic range of the ADC can be calculated by using the following equation, if the quantization noise is uniformly distributed across the Nyquist Bandwidth.

$$SNR_{quantise} = 6.02b + 1.75dB \quad \text{Equation 35 [5]}$$

where b is the bit number resolution of the ADC. For 12 bits ADC, the dynamic range due to quantization noise should be 73.99dB.

However Equation 35 does not accurately estimate the dynamic range of the ADC. This is because besides quantization noise, the ADC noise floor also includes thermal noise and noise due to clock jitter and other noise sources. According to the Analogue Devices component specification, the SNR for the AD9430 is 61dB. Given the digital bandpass filter inside of the FPGA has a passband of 25MHz, which is approximately a quarter of the Nyquist bandwidth, only a quarter of the total amount of ADC noise will be present at the output of the filter. This will improve the SNR of the ADC by 6dB. Hence the overall SNR for the ADC is 67dB. Given that the max input power of the ADC is 4.6dBm, the MDS of the ADC is -62.4dBm.

5.3 Complex Down-Conversion

The analogue signal at the output of the RF front end is centred at 50MHz with 20MHz pass bandwidth. It is then sampled at 200MHz by the ADC. The signal spectrum after sampling can be represented by the following diagram.

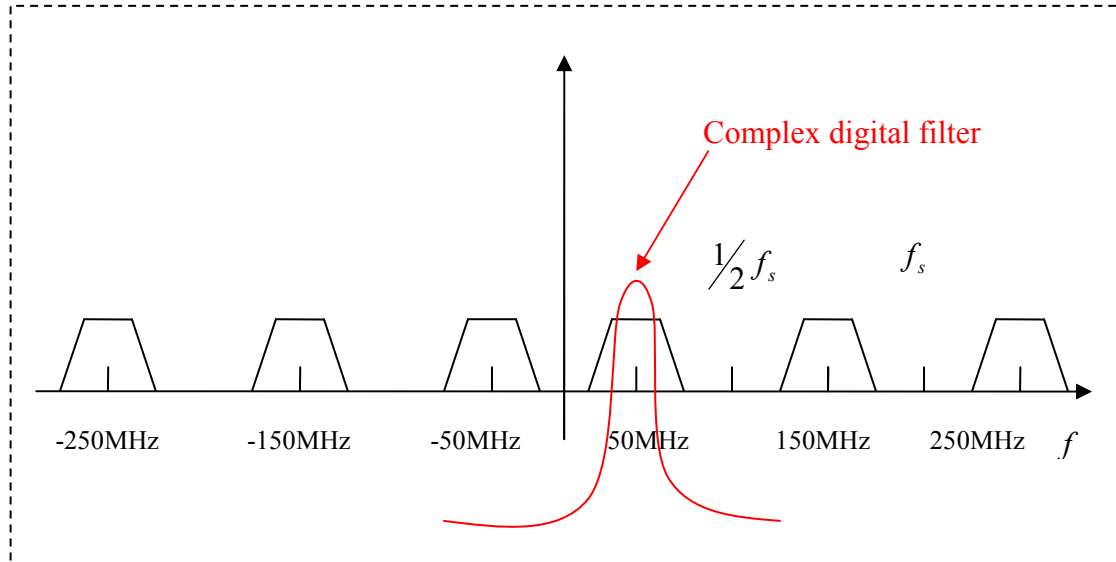


Figure 18: Sampled signal spectrum

A complex filter is then applied to the sampled signal and converts the signal into its complex form. Figure 18 shows the schematic frequency response of the digital filter

applied to the sampled signal, which selects a 2MHz frequency band centred at 50MHz. The filter is designed to have a 2MHz pass bandwidth and 25MHz stop bandwidth, and hence only signals within the GPS operating bandwidth will be processed. To reduce the FPGA processing load and hence the power consumption, the sampled signal is further down-sampled by a factor of 8. This down sampling process will cause aliases to appear at every 25MHz away from 50MHz for a complex signal. Therefore the complex filter stop bandwidth is set to 25MHz that is from -12.5MHz to 12.5MHz. The signal spectrum after down-sampling is shown in Figure 19.

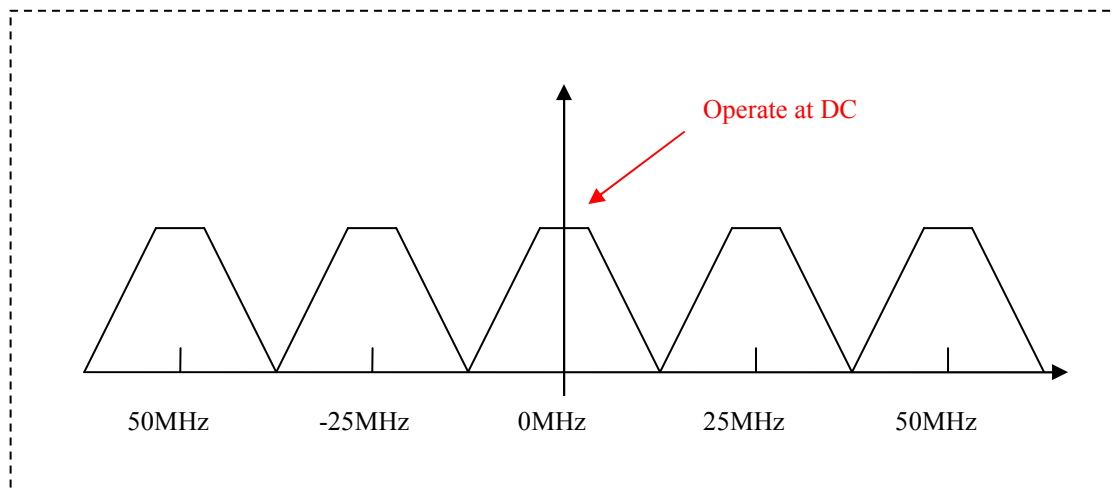


Figure 19: Frequency shift due to aliasing

The complex filtering and down conversion process are combined and realized by a FIR filter. To utilize the least area of FPGA, the FIR filter is implemented with polyphase decimation structure by using the Xilinx FIR filter core generator. The filter coefficients are pre-calculated by using MATLAB. It is initially designed as a real low pass filter with 2MHz pass-band and attenuation greater than 50dB at 12.5MHz away from the centre frequency. 60 taps have been used in the filter to achieve a minimum stop band attenuation of 60dB. This real LPF is then frequency shifted by $\frac{1}{4}$ of the maximum digital frequency so the pass band is centred at 50MHz. During this process, the real filter also has been transformed into a complex filter with 30 taps for each of the I and Q components. The magnitude and phase responses have been plotted in Figure 20.

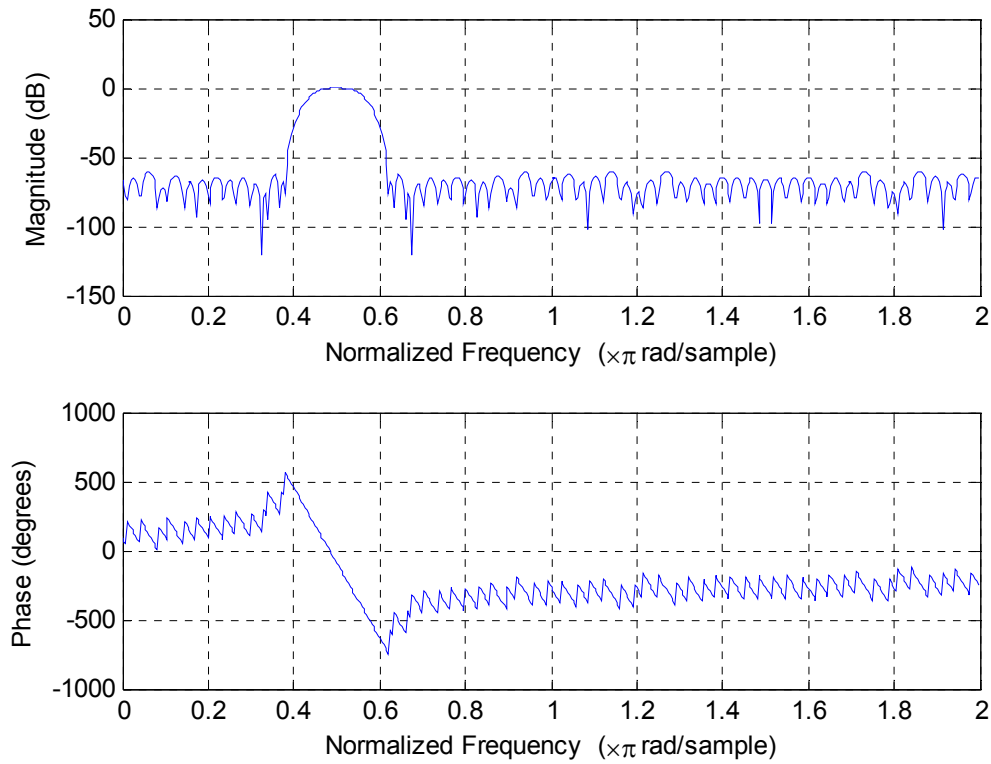


Figure 20: Frequency and phase response of the digital filter

By using this complex BPF, the real input signal is transformed into a complex signal with exactly 90 degrees out of phase between I quadrature and Q quadrature. This filtered signal then becomes the input signal to the complex LMS filter. The LMS filter is clocked at 25MHz, which implies that the alias appearing at DC caused by down-sampling is selected for the baseband processing, as has been shown in Figure 19.

5.4 Digital Signal Processing

The Figure 21 shows a systematic view of the logic blocks implemented on the FPGA on the Heron-I05 board. The VHDL language has been used for the FPGA implementation. The code was developed based on the example code given by Hunt Engineering. The example code is intended to ensure the correct configuration and timing constraint of the FPGA. It is used subject to Intellectual Property Provided by Hunt Engineering Pty Ltd.

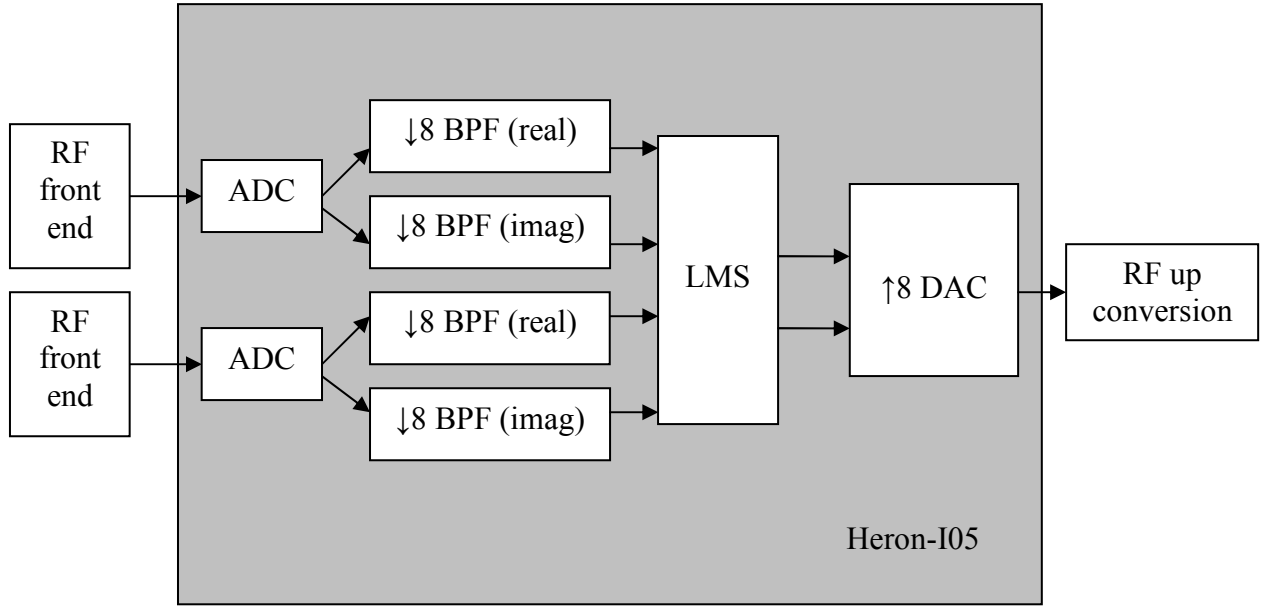


Figure 21: Major logic on FPGA

Even though the RF front ends are physically identical, they still have a different passband response due to onboard component variation. This will result in a frequency dependent mismatch between the reference channel and the auxiliary channel of the adaptive filter. The spatial LMS algorithm is not capable of equalizing this mismatch over a range of frequencies. Hence it may lead to incomplete interference rejection and distortion of the desired signal. However, the frequency dependent mismatch can be reduced by implementing a STAP tap delay line on the auxiliary antenna channel. As the LMS algorithm trying to minimize the output MSE, the frequency response of the auxiliary channels will be modified to match with the reference channel. Hence frequency dependent mismatch will be reduced once the algorithm converges. The number of taps required is determined by the order of mismatch.

The mismatch between the RF front ends has been measured and is plotted in Figure 22. The detailed measurement procedure is described in Chapter 6. In this plot, the frequency spectrum has been centred at 50MHz with 10MHz per division, and the actual GPS operating bandwidth has been highlighted. By observing this plot, there is one local minimum of -1.5dB within the 2MHz GPS operating bandwidth, where marker 1 indicates approximately. Therefore, it should require at least a 1st order

autoregressive processor to model the mismatch between the two channels in the RF front end. In this case, this mismatch can be equalized by using a 1st order FIR filter.

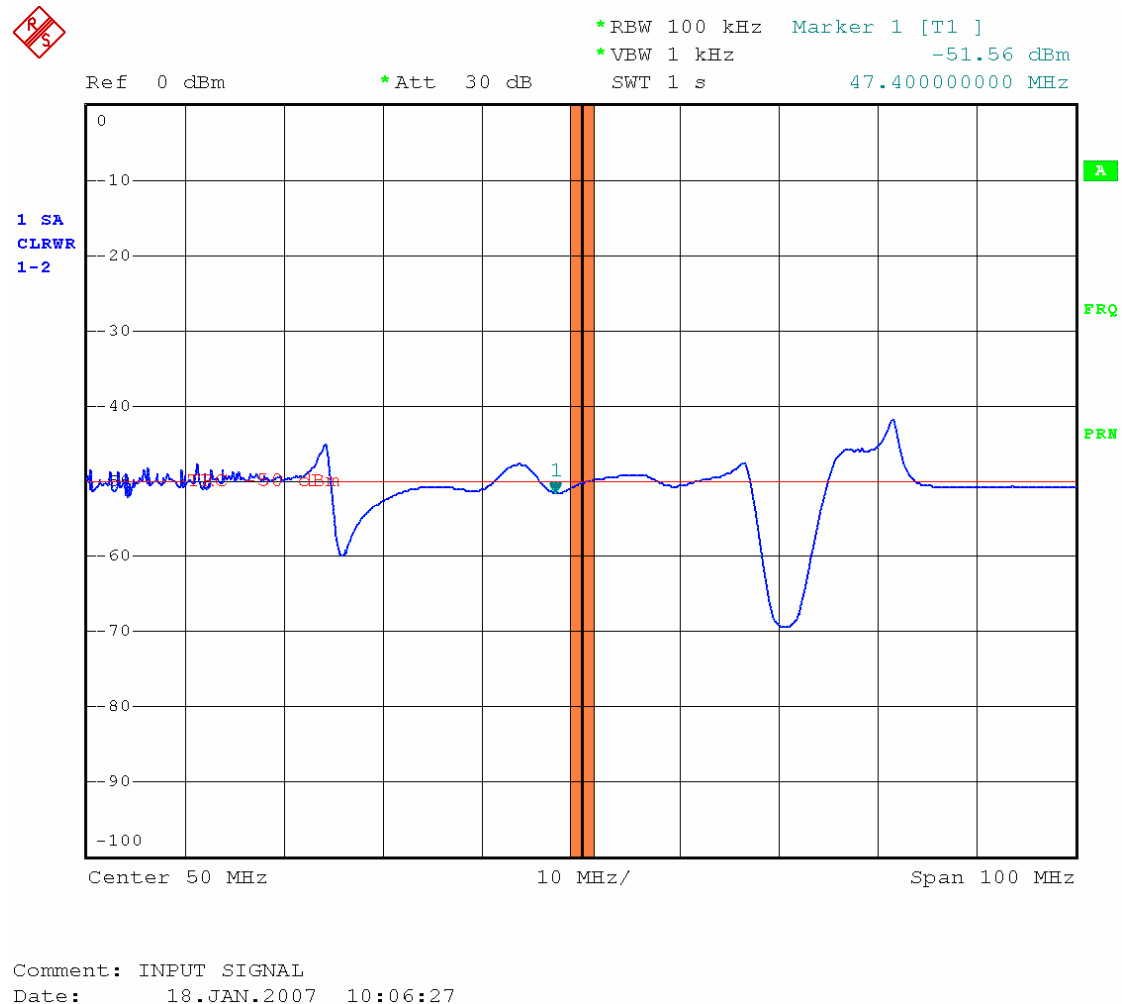


Figure 22: Mismatch between RF front ends.

To protect against the possibility that a 1st order autoregressive model is insufficient to adequately model the mismatch, a three-tap FIR filter has been added to the auxiliary channel to equalize the mismatch. More taps provide more degrees of freedom during the equalization, however, the number of taps the filter can have is constrained by the FPGA area. As a compromise between the overall performance and the FPGA area requirements, a three-tap filter has been implemented.

In order to reduce the overall developing, testing and debugging time, the LMS algorithm has been implemented by using the System Generator within Simulink, MATLAB. System Generator is a high level logic development tool for FPGA, which

provides system modelling and automatic code generation in VHDL. Logic can be implemented by using different Xilinx logic blocksets, which will then be translated into VHDL models by the system generator. Each Xilinx blockset is mapped to a particular core generator depending on the type of FPGA and this one to one mapping relationship allows efficient FPGA area usage to be achieved during this process. In order to reduce the usage of FPGA logic area even more, hardware adders and multipliers on the FPGA chip have been used wherever possible. The logic implementation inside of the System Generator has been attached in Appendix C.

Besides the dynamic range of the RF front end, the precision of the LMS algorithm also limits the AJ margin. It is determined by the output number representation of each Xilinx blockset. As most of the Xilinx logic cores do not support floating point calculation, the number of bits and binary point position must be pre-determined. This is achieved by specifying the output precision parameter inside of each logic block.

An incorrect number representation will degrade system performance. When the output of any blockset is too big to be represented by the pre-determined precision specification, an overflow will result. This implies that the jamming signal power is too strong and cannot be cancelled by the LMS algorithm with the current precision setting. On the other hand, underflow will occur when the output of any blockset is too small to be represented. As a result, some of the jamming power can not be detected by the LMS algorithm and will be let through to the GPS receiver. Overflow and underflow can be prevented by allocating more bits in the digital domain. However, this will increase the FPGA area usage. Consequently, it is harder to ensure time delay between any two latches inside of FPGA is less than the system clock period.

The inputs precision to the LMS algorithm is chosen to be fixed at 16 bits. However, bit shifts and truncations have been carried out within the implementation of the algorithm such that its anti-jamming range is just higher than the dynamic range of the RF front end. Hence the overall unit anti-jamming ability is not constrained by the digital domain and at the same time the minimum FPGA area is used. Based on the Simulink simulations, the adaptive filter is capable of providing 60dB cancelling range at the full input power when 2MHz white noise is applied.

The convergence rate and converged MSE have also been verified against the steepest descent convergence described in Chapter 3. This is achieved by simulating the LMS Xilinx implementation in MATLAB, with the setup of the experiment as illustrated in Figure 23. During the simulation, two identical sine waves with independent white noise were generated from the workstation and loaded into Simulink separately. The sine waves were given amplitudes of 0.8, and independent White Gaussian Noise (WGN) was added to each sine wave with a variance of 0.001 units squared.

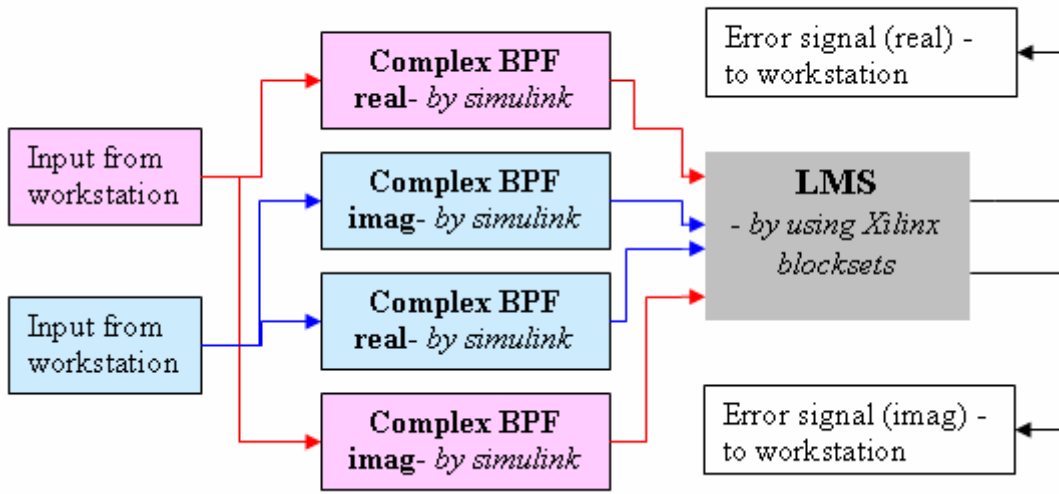


Figure 23: LMS rate of convergence simulation setup

In Figure 23, the two antenna channels of the adaptive null steerer have been marked in red and blue. The input signals are filtered by two identical and independent digital BPFs before they are processed by the LMS algorithm. It is worth clarifying that in this simulation, the complex BPF is implemented using a FIR decimator from Simulink. In practice, it is implemented using a LogiCore polyphase filter inside the FPGA. Although the two filters are implemented differently, they are mathematically equivalent.

The magnitude and phase response of the complex BPFs are shown in Figure 20. As only the positive frequency of the sine wave is selected after the filtering, the amplitude of the filtered sine wave is halved. The complex signal power is calculated as A^2 , where A is the amplitude of the signal. Given that the amplitude of the original

real sine wave before the complex BPF is 0.8 units, the power of the complex sine wave is therefore 0.4^2 unit square.

The minimum MSE (J_{\min}) of the Wiener filter can be calculated using Equation 7, which requires an accurate estimate of the noise power added on both the reference and auxiliary channels. On the other hand, as the complex BPF is also applied to the WGN, the total noise power let through to the LMS filter is also reduced. The amount of noise power which passes through the complex filter is proportional to the area under the filter response in the frequency domain across the whole digital bandwidth. To better estimate the noise power, the integral of the frequency response of the filter is calculated and a value of 0.063 is obtained, given that the total area across the whole digital bandwidth is 1. This implies that only 6.3% of the WGN power input to the complex BPF is added to each channel of the LMS algorithm.

The error signal obtained from this simulation has been averaged over 100 realizations and its power in dB is plotted in Figure 24 against the number of iterations during the convergence process. As the exact covariance of the input signal is known in this case, the convergence of the steepest descent algorithm can be calculated and plotted in red in Figure 24. Both convergence curves have had their initial error signal power normalized to 0dB. However, the convergence curve obtained by simulation appears to be a delayed version of the steepest descent convergence. This is due to the propagation delays inside the complex BPF. As the filter contains 30 taps for both the I and Q channels, 30 delays are required before convergence commences. From this plot, it can be concluded that the convergence rate measured using the simulated data agrees with the theoretical value. With a step size of $1/16$, approximately 200 iterations are required for the LMS filter to converge to its optimum value.

The minimum MSE is calculated according to Equation 7 based on the error surface of the steepest descent algorithm. As the input signal is known in this simulation, w can be solved using Equation 8. Hence the minimum MSE is given by $\sigma_d^2 - p^H R^{-1} p$ and a value of 8.526×10^{-5} has been obtained. The converged MSE of the LMS algorithm is estimated by averaging the error signal power of the last 1000

samples of all realizations, yielding a value of 9.032×10^{-5} . This implies that the misadjustment of the LMS algorithm is 0.059, which is more than the theoretically calculated value of 0.015 according to Equation 25. In order to maximize the cancelling range of the LMS algorithm, truncation and bits shift have been carried out during the implementation process. This results in the LMS filter not being able to represent small numbers beyond a certain range, hence increasing the misadjustment above the theoretically predicted value.

According to Figure 24, the error signal converged to its optimum value after approximately 200 iterations. As the LMS algorithm is running at 25MHz in the FPGA, the total convergence time will be $8\mu\text{s}$.

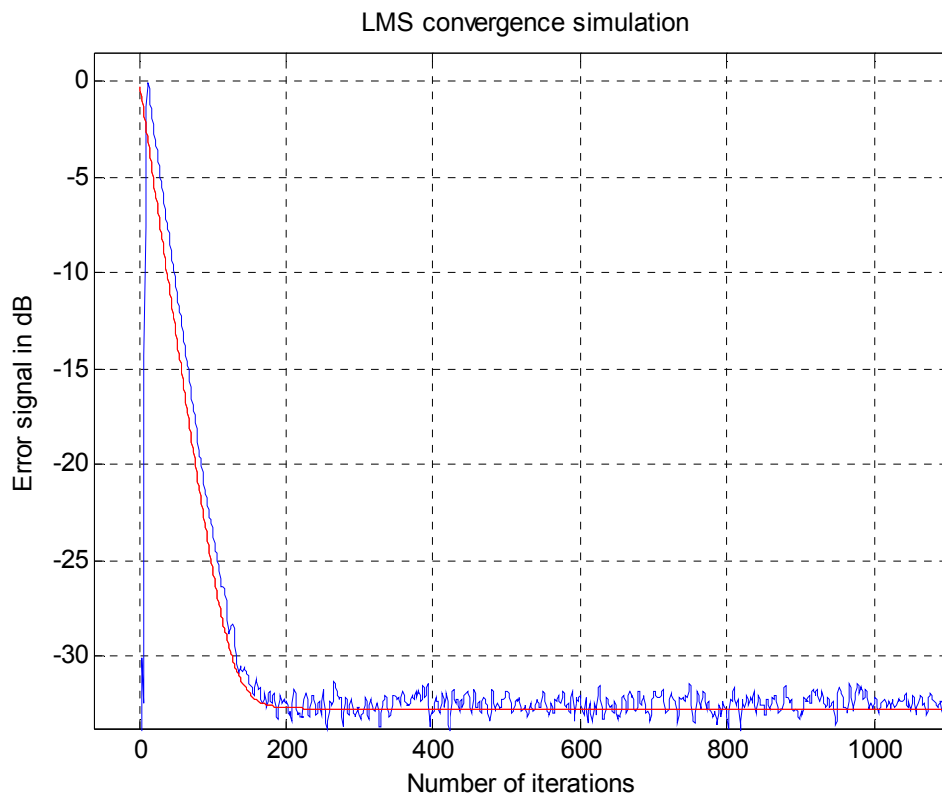


Figure 24: Simulated LMS algorithm convergence

The LMS algorithm requires the calculation of an error signal to update the weight vector. At a high sampling frequency, the calculation of the error signal will require a time delay. In other words, updating the weight vector by using the current error signal requires extremely fast computation speed and remains practically challenging. An implementation of the LMS algorithm, which can be retimed and pipelined to five functionally equivalent stages, is known as the Delayed LMS (DLMS) algorithm [33].

In this algorithm, a slightly delayed error signal is used to update the current weight vector. This delay eases the time required for calculating the error signal. If D is used to represent the number of delays in the pipeline of the DLMS algorithm, then the weight vector can be updated as Equation 36 shows.

$$w(n+1) = w(n) + ue(n-D)x(n-D) \quad \text{Equation 36[33]}$$

Through the use of DLMS, the algorithm is able to be implemented in a pipelined fashion. As a result, this algorithm can be adapted for programming onto the FPGA. Theoretically, the DLMS algorithm slightly increases the training time, but has the benefit that the retiming principle can be applied.

5.5 Physical Structure

Figure 25 shows a side view of the complete unit. The FPGA board is mounted on top of the RF aluminium shielding box shown in the top half of Figure 25. This forms the complete unit. However, to be able to determine the performance of the unit easily and make field testing possible, two independent commercial GPS receivers and two modems are integrated together with the unit and have been mounted below the unit. One of the receivers is connected to the adaptive antenna array, so performance of the unit can be reflected through the receiver message. This forms the protected channel. The other receiver is connected directly to a GPS antenna which demonstrates the behaviour of a normal receiver under a jamming environment without the anti-jamming unit. This forms the unprotected channel. The two receivers' messages are transmitted via the two modems on board which enable the UAV to communicate wirelessly to the ground station during flight.

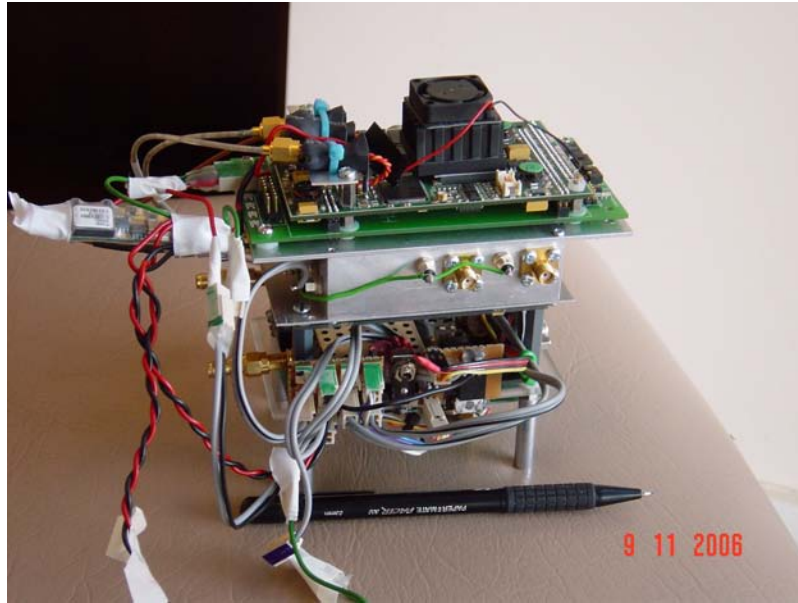


Figure 25: Side view of the anti-jamming unit

Chapter 6

Laboratory Performance Testing

The anti-jamming unit has been tested extensively under laboratory conditions. This section details the procedure of each test and the corresponding results obtained.

6.1 Sensitivity

The sensitivity of the RF front end determines the minimum detectable signal level. It is one of the important figures by which to evaluate the performance of any analogue receiver. The signal often becomes undetectable when the signal level drops below the noise level, so it is necessary to determine the self induced noise level of the RF front end first. As explained in Chapter 4, the NF can be measured by determining the noise power at the output when no input signal is applied. A 50Ω load is required to match the input impedance.

During this test, the spectrum analyser was set to have a resolution bandwidth (RBW) of 100kHz and sweep time of 10s in order to obtain a stable reading. The attenuation level was set to 0dB to minimise the noise introduced by the spectrum analyser.

When there is no input signal present, the noise power at the output of a RF system is the total noise contributed by the RF system itself plus the amplified thermal noise at the input. Hence the noise figure can be calculated by using the following equation:

$$NF = P_{out} + 174 \text{ dBm/Hz} - 10 \log(B_{WIF}) - G \quad \text{Equation 37}$$

where P_{out} = measured total output noise power

174 dBm/Hz = noise density of 290K ambient noise

B_{WIF} = frequency range of interest, in this case it will be the RBW

G = total system gain

The IF filter inside the spectrum analyser defines the IF frequency range that is used in the power calculation of each point on the frequency axis. The bandwidth of this filter defines the RBW. It is desirable to have a rectangular filter response in order to obtain an accurate measurement. However, the transient response of such a filter is unsuitable for a spectrum analyser. In practice, a spectrum analyser uses a Gaussian filter instead for optimized transient response. Therefore in practice, the RBW is defined as the 3dB bandwidth of the IF filter in the spectrum analyser. A small correction factor should be applied to give an accurate noise power measurement. In this case $B_{WIF} = 1.065 \times RBW$ has been used, according to the spectrum analyser handbook [33].

By using the spectrum analysis, the measured noise power for the RF front end channel 1 and channel 2 were -82.46dBm and -83.10dBm respectively. Based on Equation 37, the noise figures for channel 1 and channel 2 are 7.1dB and 6.4dB respectively. These values are higher than the predicted noise figure of 2.48dB, which has been calculated in Chapter 4. This is attributable to several causes. The layout of the RF front end was designed such that the total area of the PCB board was minimized. Therefore some of the ideal layout requirements of the components on the board were not satisfied. This can degrade individual component performance, and cause an increase in the noise figure. Another reason is due to impedance mismatch between components. To ensure maximum power delivery between stages in the cascaded chain, impedance must be matched between components. However, as all PCB mounted components suffer +/- 20% variation in value, it is very difficult to achieve a complete impedance match via matching network circuits between components. This results in a reduction in the cascaded chain and could be another reason for the poor measured noise figure.

The minimum detectable signal is determined by the noise floor of the device in a given bandwidth. It is usually set to be 3dB above the noise floor in practice. The noise floor can be calculated by using the following equation:

$$\text{Noise Floor} = kT_s B = k(NF)T_a B \quad \text{Equation 38}$$

where k is Boltzman's constant, B is the system bandwidth, T_s is the equivalent input system noise temperature, T_a is the antenna input noise temperature due to

environment noise, and NF is the noise factor of the device. According to this equation, the noise floors for channels 1 and 2 of the RF front end are calculated to be -92.45dBm and -92.94dBm respectively based on the measured noise figures.

6.2 Selectivity

The selectivity of the RF front end refers to its ability to reject signals outside its pass band and is mainly determined by the selectivity of the IF filter. To test the selectivity, a signal generator and spectrum analyser were networked together using the General Purpose Interface Bus (GPIB), thereby allowing sweeps through the entire frequency spectrum. The setup for the test is shown in Figure 26 below. From this test, the actual bandwidth of the front end can be determined.

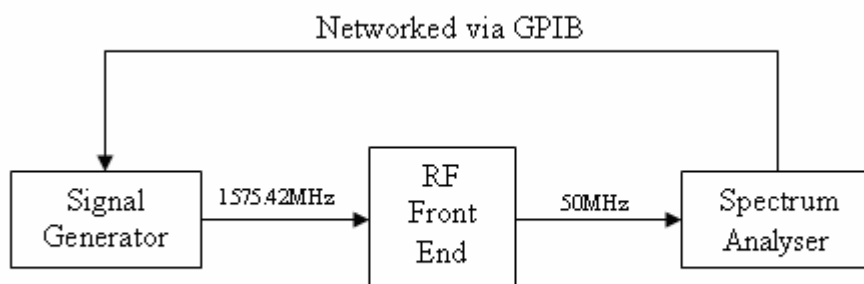


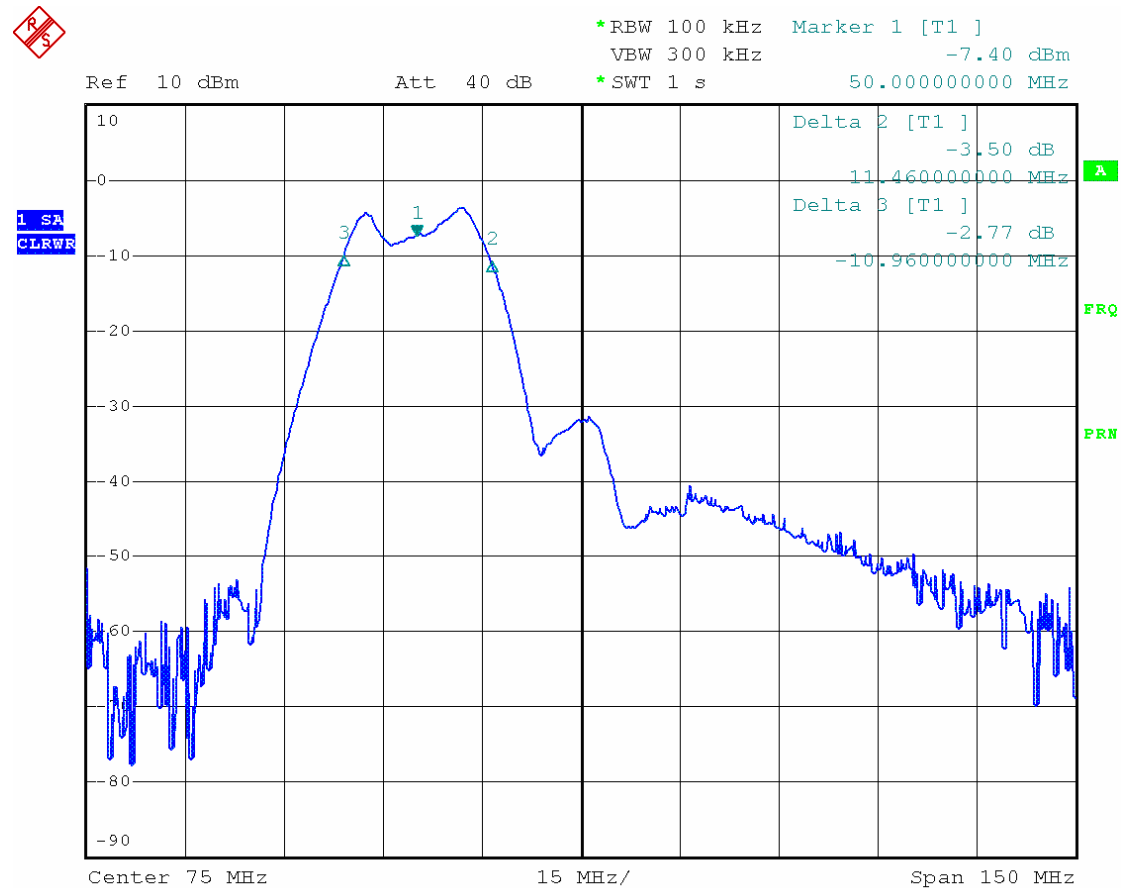
Figure 26: RF front end selectivity test setup

The output from the spectrum analyser is shown in Figure 27. Marker 1 indicates 50MHz which is the exact centre of the passband. Markers 2 and 3 have been used to mark the approximate position of the 3dB drop from the centre frequency. The distance between marker 2 and marker 3 is roughly 20MHz. This value agrees with the intended design value. In this diagram, a second peak is apparent at 75MHz. This is due to internal oscillations in the RF front end. However, this oscillation is outside the passband of the digital filter and will be filtered out in the digital domain.

Figure 27 also indicates that the passband of the RF front end is not smooth. This is because the exact designed values of the analogue components which form the IF filter cannot be obtained in practice. Components with values closest to the desired values have been used. This results in a non-linear passband response. In addition,

most of the PCB mounting components suffer from sensitivity to temperature variation. The actual values of the components vary with the operating temperature, with some varying up to +/- 20%. This further degrades the linearity of the filter passband response.

By using spectrum analysis, the mismatch between the two RF front ends has also been measured and plotted in Figure 22 in Chapter 5.



Date: 16.JAN.2007 07:44:23

Figure 27: RF front end passband spectrum

6.3 Non-Linearity of RF Front End

The RF front end IIP3 can be measured by applying two tone signals of frequency f_1 and f_2 at the input and measuring the output power in relation to third order harmonics. The third order products should appear as sidebands and have frequencies of $|2f_1 - f_2|$ and $|2f_2 - f_1|$.

A Signal Generator and Network Analyser were used to provide two tones at 1.57552GHz and 1.57532GHz respectively. The two signals are tuned to have the same power and were combined together by using a splitter. Figure 28 illustrates the setup of this experiment.

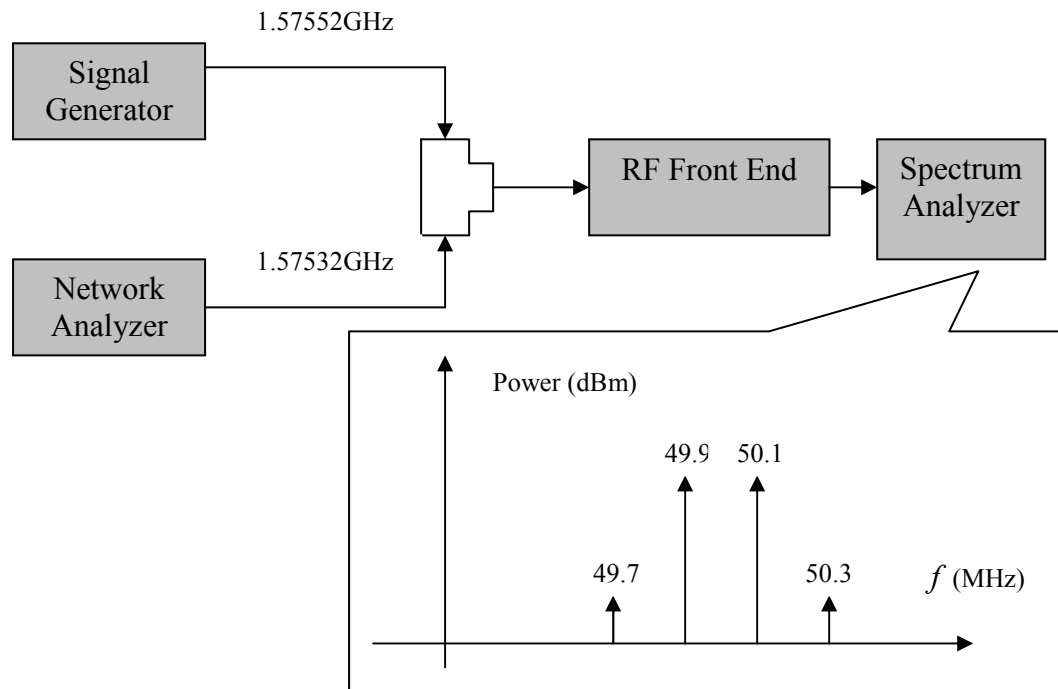


Figure 28: Measurement of IIP3 illustration

To be able to detect very low intermodulation products at very low input signal powers, the spectrum analyser has to be set to a very fine RBW so the noise power in each band is reduced.

The fundamental output signal power and the power of the 3rd order harmonics were measured and have been plotted against the input power in Figure 29. Ideally, the 3rd order harmonic components should increase at a 3:1 ratio with input power in the small-signal gain region. Therefore, the curve of the 3rd order harmonics against input signal power is expected to be a straight line with a slope of 3 at low input signal powers.

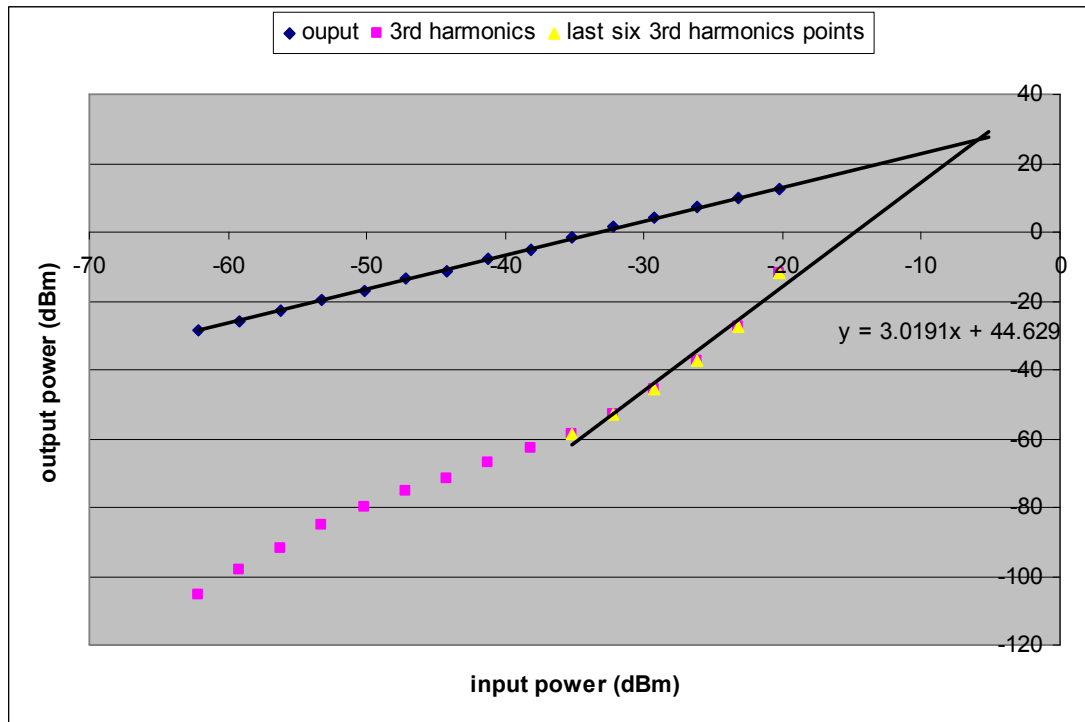


Figure 29: Tested result of IIP3

From the above diagram, the 3rd order harmonic does not have a slope of 3 over the entire input power range, and its power is stronger than predicted at low input powers. The harmonics components only start to increase close to a rate of 3 when the fundamental input power is close to the 1dB compression point. To show the non-linearity of the harmonic powers more clearly, the IIP3 was calculated at each input power level and the results are plotted in Figure 30. The IIP3 point should be a constant value if the harmonic power increases linearly with the fundamental input power. However, as Figure 30 indicates, the IIP3 varied by over 20dB and only converged to -5dBm at larger input powers.

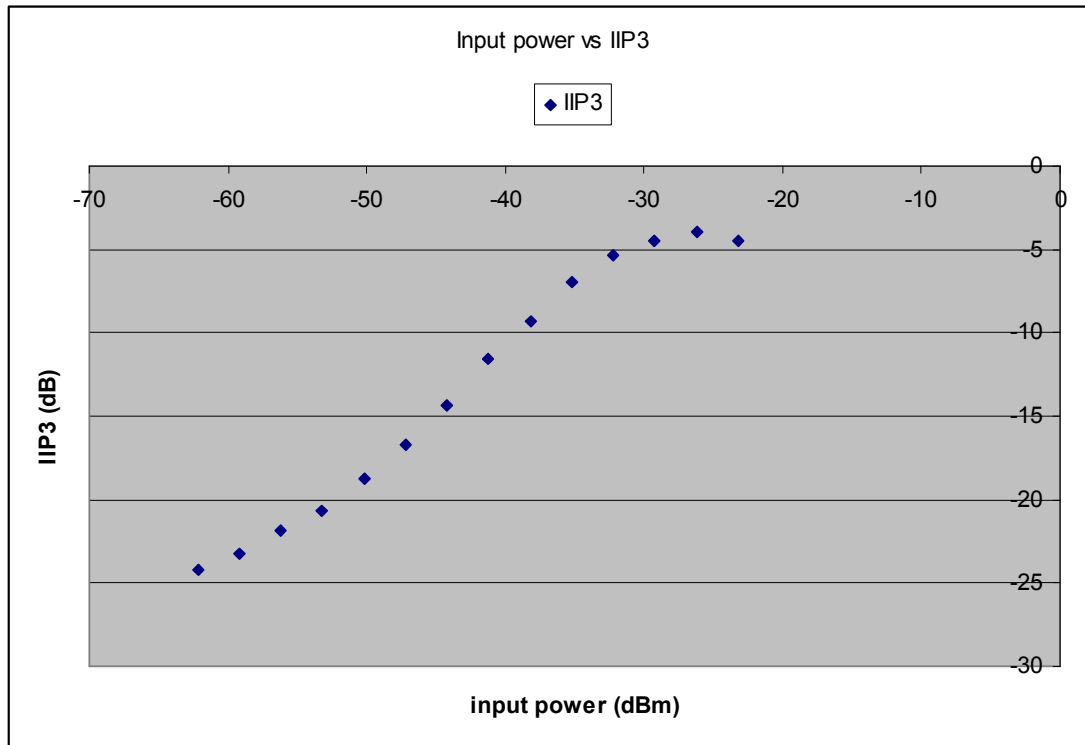


Figure 30: *IIP3 varies at different input power level*

A line of best fit using the last six data samples has a slope very close to 3. By using this slope, the IIP3 of the RF front end is estimated to be -6dBm. This value, together with the MDS calculated in the sensitivity section previously, specify the overall dynamic range of RF front end to be 55.633dB. This value is 7dB less than the predicted dynamic range of the RF front end. When calculating the theoretical performance of the RF front end, the passive BPF at the end of the cascade chain was given 0dB gain, in other words, a lossless filter. However, it is difficult to ensure that the reactance of the filter is 0Ω in practice, causing loss of gain in the overall system. This could be the main reason for the smaller than expected dynamic range achieved. The non-linearity of the 3rd order harmonics could be due to the optimization techniques implemented in the high gain amplifier (LT5514). The amplifier sacrifices some of the harmonic performance at lower input power for a better IP3 point overall.

6.4 Overall Anti-jamming Ability Analysis

The overall AJ range by using the null steering technique is fundamentally limited by the overall system dynamic range. Therefore, dynamic range compatibility among sub-components of the unit is crucial for obtaining maximum AJ range performance.

Figure 31 illustrates the dynamic range compatibility of the RF front end and ADC. On the left hand side is the output performance from the RF front end and on the right hand side is the input performance for the ADC. This diagram clearly shows that the overall system dynamic range is limited by the dynamic range of the RF front end itself.

The gain of the RF front end has been chosen such that the MDS level of the RF front end within the IF bandwidth is above the MDS of the ADC. In this case, it is approximately 7dB higher. The reason for this gain setting is to maximise the SNR in the GPS receiver after the de-spreading process. If the MDS level in the RF front end falls below -62.4dBm, which is the MDS level of the ADC, GPS acquisition is still possible, but the carrier-to-noise ratio will be degraded.

To avoid degrading the carrier-to-noise ratio of the GPS signal significantly, the gain of RF the front end can only be reduced by another 7dB. This would result in a dynamic range improvement of 7dB when using the AGC. This implies that it is possible to improve the overall system AJ range by at least 7dB if AGC is applied.

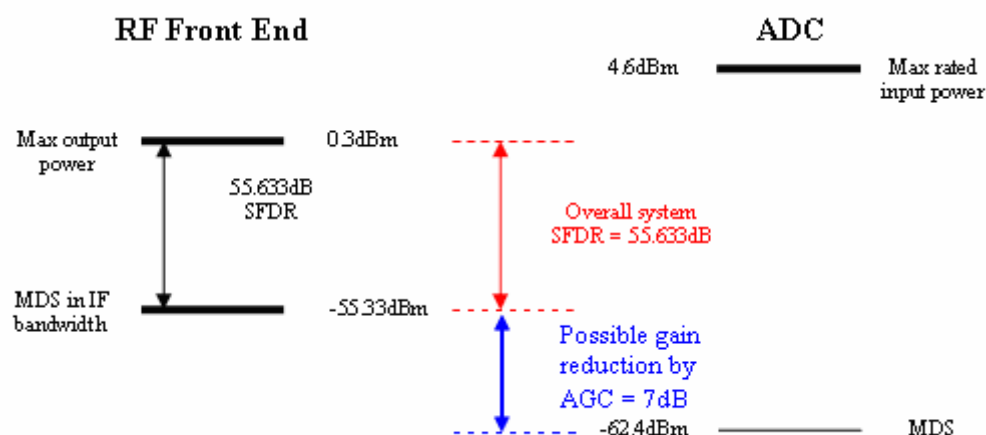


Figure 31: *Compatibility of RF front end with ADC*

6.5 Overall Broadband Anti-Jamming Lab Test Result

The overall anti-jamming range has been tested in the laboratory. Figure 32 illustrates the testing procedure. A broadband noise generator is used as the interference source. A number of amplifiers are inserted to ensure the interference signal is strong enough

to jam the GPS receiver with the anti-jamming unit present. The final broadband noise signal is 2MHz wide and centred at 1.57542GHz. A manually controlled attenuator is inserted in the cascaded chain to adjust the interference power level.

The GPS signal is generated using a GPS simulator. This signal is then split into two identical signals and combined with the jamming signals separately as the two inputs to the antenna array. One of the two inputs is also directly connected to the GPS receiver. However, to simulate that the GPS and jamming signals are incident upon the array from different directions, so that the GPS signal will not be cancelled, different length of cables must be used to carry the GPS and interference signals before they are combined together. Hence, the anti-jamming range can be determined by comparing the satellite C/No when the anti-jamming unit is either switched in or out.

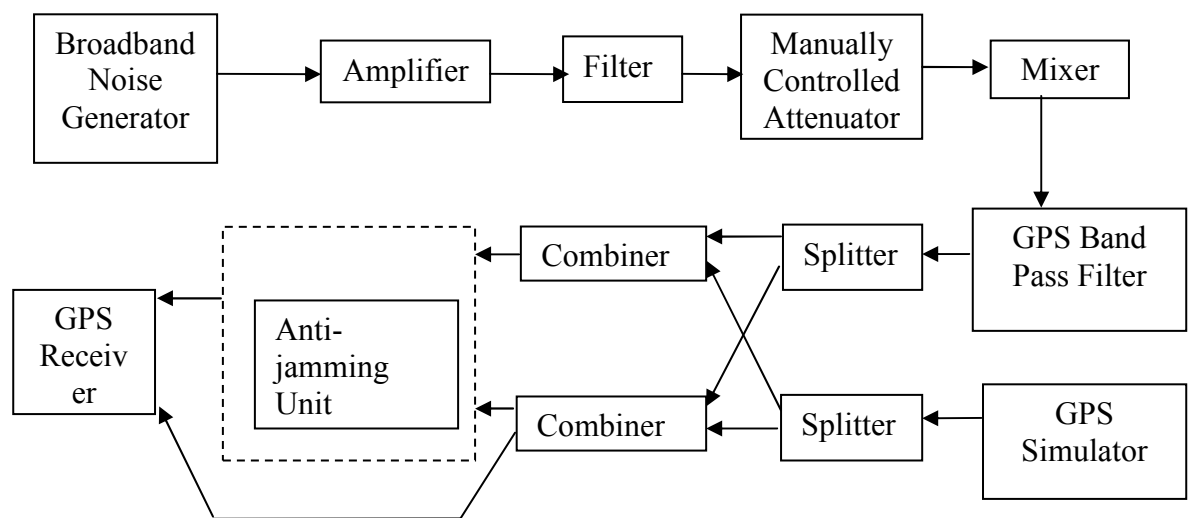


Figure 32: Laboratory anti-jamming range testing setup

There were 11 satellites in view during the simulation and all satellite C/No values were recorded separately at various interference power levels. The average value of the C/No across all satellites has been calculated and is plotted against jamming power in Figure 33. The red line represents the average C/No of the received signal with the anti-jamming unit present. The blue line represents the average received C/No when the anti-jamming unit is not used. According to this diagram, the received signal C/No dropped below 30dB when the attenuation level was reduced below

-60dB. However, when the anti-jamming unit is present, the received signal C/No was above 30dB steadily until the attenuation level is reduced up to -20dB. Therefore, the overall anti-jamming range is approximately 40dB. The fact that the C/No remained steady despite the increased jamming power suggests that the direction of the GPS signal is significantly different from the nulling direction. However the AJ range is significantly lower than the predicted value of 54.5dB. The main reason for this discrepancy is because the dynamic range calculation based on the SFDR, refers to the point when the SNR is degraded by 3dB due to third order harmonic distortion products, rather than when the receiver is jammed completely. The power difference between the two 3dB points is closer to 50dB, i.e. the 3dB point for the protected channel occurs at an attenuation of -20dB which is approximately 50dB above the attenuation setting of -70dB where the SNR of the unprotected receiver drops by 3dB. At attenuation settings lower than -20dB the third order distortion power increases at three times the input power in the dB domain, thus the SNR drops off more rapidly than for the unprotected receiver giving a lower overall interference power rejection margin for complete jamming of the receiver. To further improve the interference rejection margin of the unit an Automatic Gain Control could be implemented, which will provide 7dB more in dynamic range and hence in anti-jamming range.

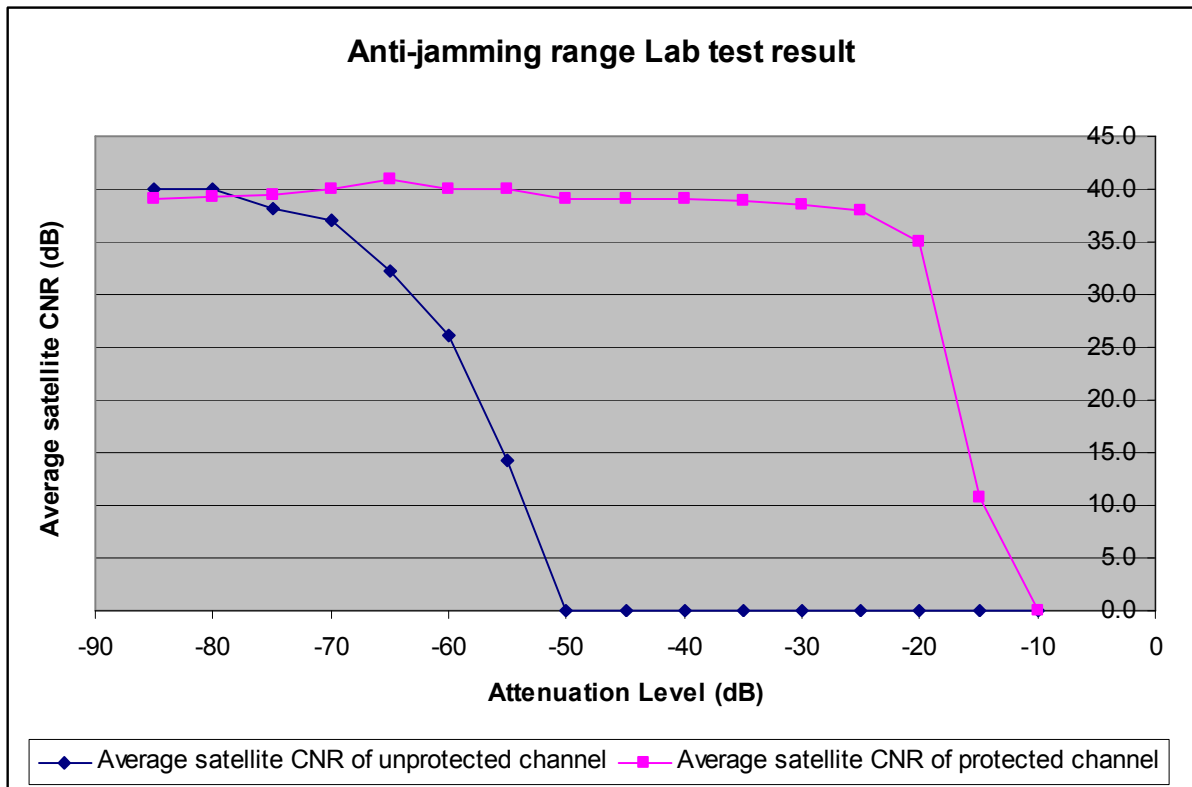


Figure 33: Overall anti-jamming ability lab test result

6.6 Performance enhancement and simulation results

A UAV may experience strong turbulence or be subject to sharp banking angles during flight. This sudden motion will introduce discontinuities in the phase of the adaptive antenna array. The convergence rate of the LMS algorithm is very important when dealing with such a situation. If the LMS algorithm does not converge quickly enough, some of the jamming power will get through the interference canceller to the GPS receiver. As a result, the GPS receiver on board may be jammed for short period of time. With fixed step size LMS algorithm, the step size is limited by the maximum input power to avoid instability. This implies the convergence time will increase when the input power is reduced.

The convergence rate of the LMS algorithm can be optimised by adjusting its step size accordingly to its input signal power. Such a technique is referred to as the Normalized LMS (NLMS). This comes at a price of greater computational complexity. In this project, the LMS algorithm is firstly implemented using a Xilinx blockset inside of Simulink. It is then translated into VHDL using a system generator and then downloaded onto the FPGA. The LMS algorithm can be easily modified into

a NLMS algorithm by adding extra logic blocks. These logic blocks are used to estimate the input signal power and make the appropriate step size adjustments. To simplify the calculation process, the NLMS algorithm has been given quantized step sizes of 1, 0.5, and 0.25.

Figure 34 shows the convergence rate of LMS against the NLMS, both of which have been implemented using Xilinx blocksets inside Simulink, which allows them to be mapped directly onto FPGA. There are five different plots in this diagram; the x-axis indicates the simulation time. The first plot is the input signal applied to both algorithms. It is 2MHz band limited white noise, with maximum input amplitude of 0.5 to prevent overflow. The second plot is the average input signal power calculated inside of NLMS, and the chosen step size is shown in the third plot. The second and third plots clearly show the inverse relationship between the estimated input signal power and the step size. The fourth and fifth plots are the error signals of the NLMS and LMS algorithm respectively. By observing Figure 34, it can be concluded that the convergence time of the NLMS algorithm is approximately 20% of the convergence time required by the conventional LMS algorithm. It can also be concluded from Figure 34 that the final converged noise power of the NLMS algorithm is significantly reduced. This implies a reduced level of misadjustment noise for the NLMS algorithm compared with the conventional LMS algorithm.

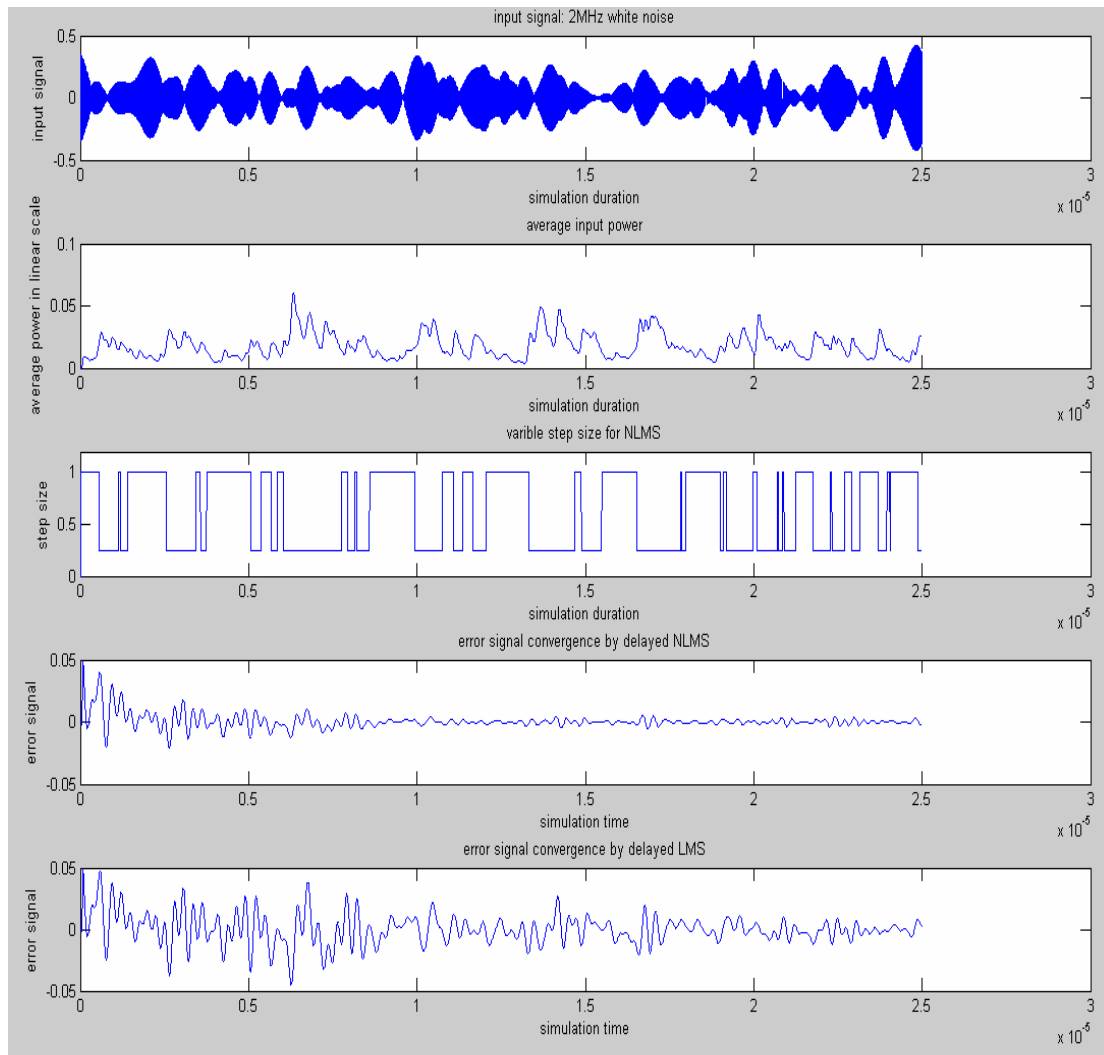


Figure 34: Performance comparison of LMS vs. NLMS (MATLAB simulation)

Chapter 7

Woomera Trial 2006

The anti-jamming unit was taken to a trial in 2006 in Woomera SA, where a jamming signal within the GPS operating bandwidth was permitted to be radiated within certain power limits during a certain period of time. The trial was supported by the Defence Science and Technology Organisation (DSTO), who kindly made a 2MHz high power broadband jammer available for experimental purposes. There were two tests conducted during this trial with different antenna array configurations. This chapter describes the test procedures that were carried out to characterize the unit and the corresponding results obtained.

7.1 UAV Configuration

A model aircraft has been used as a UAV during this trial. The anti-jamming unit was mounted inside of the model aircraft during all tests. Figure 35 illustrates how the anti-jam unit was mounted in the UAV.

The anti-jamming unit was placed in front of a GPS receiver and the receiver messages were constantly monitored to determine the performance of the unit. To be able to maintain communication with the UAV over a long distance, the receiver messages were transmitted wirelessly via an onboard modem. This is known as the protected channel and has been marked in green in Figure 35. The detailed physical structure of the unit is described in Chapter 5.

To be able to determine the anti-jamming ability of the unit, an unprotected channel is also integrated on the UAV. In this configuration, a GPS receiver was connected to a receiver directly and the receiver messages were transmitted via a second

communication modem on board the UAV. To distinguish the two channels, the unprotected channel is drawn in pink in Figure 35.

During the trial, it was found that the electronics in the unit radiates interference at the GPS frequency. A hand-held GPS receiver experienced difficulty acquiring GPS signals when it was placed next to the unit. The strength of the radiated signal was found to be sensitive to the cable orientations and it impacts over approximately 1 meter range from the electronic unit. Further investigations were carried out in the lab after the trial. It was found that the noise in the GPS band varies with the digital system clock frequency. This strongly suggested that the interference source was due to the switching noise inside of the FPGA. For a two element antenna array, the unit can only provide protection against single interference source. Hence adequate protection can not be provided once the external jamming signal is introduced. This would also prevent the non-protected channel from acquisition in a jamming free environment. For this reason, the antenna elements and the electronic part were mounted in different sections of the aircraft.

It was also found that the interference had the least impact on the receivers if the antenna elements were placed further towards the tail of the UAV. This was verified by using the hand-held GPS receiver, which was able to acquire satellites without any difficulty when placed near the tail of the aircraft. Thus, all the electronics were mounted in the canopy of the aircraft, including the anti-jam unit, two GPS receivers and two modems, while the antenna elements connected to the unit were placed towards the tail of the aircraft as shown in Figure 35. The GPS antenna used for the unprotected channel was placed furthest away from the electronic parts to avoid bias in the test results.

NOTE:
This figure is included on page 89
of the print copy of the thesis held in
the University of Adelaide Library.

Figure 35: *Anti-jamming unit mounting position in UAV [34]*

Two antennas are required by the anti-jamming unit; the reference antenna and the auxiliary antenna. Two auxiliary antennas were installed on the UAV during the trial, although only one of these was connected to the anti-jamming unit at a time. One was placed on the right hand side of the reference antenna facing the sky and the other one was placed directly under the reference antenna facing the ground. By doing so, different array configurations could be tested.

Different antenna array configurations provide various benefits and trade-offs. When the bottom auxiliary antenna is used, a “top-bottom” configuration is formed. As the unit is designed for UAV applications, this implies the interference signal will most likely be coming from ground and pointing towards the sky. In this case, the auxiliary antenna will experience a much stronger jamming signal than the reference antenna. This could cause the unit to be saturated much earlier, and hence reduce the overall AJ margin. However, this is not an issue if the auxiliary antenna is also facing the sky, as both antennas will receive similar amounts of jamming power. In this case a “side by side” configuration is formed.

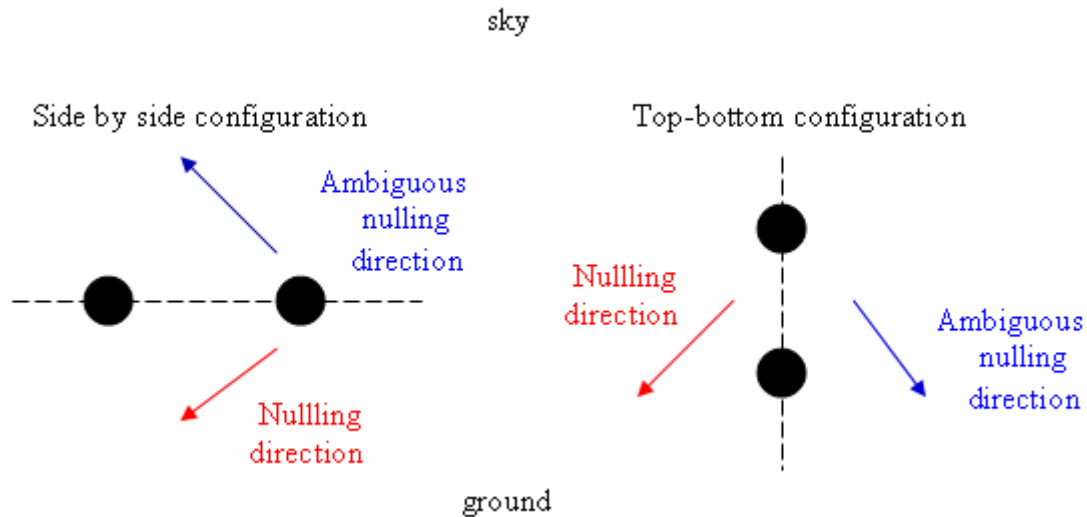


Figure 36: Antenna configuration nulling direction

On the other hand, the “side by side” configuration also has its own disadvantage. When using a linear array, nulls will be formed in both interference and ambiguous directions due to its symmetric structure. This has been demonstrated in Chapter 4. For both antenna configurations, the nulling and ambiguous nulling directions have been shown in Figure 36. In this case, a “side by side” configuration will cause the ambiguous null to point to the sky and hence cause possible cancellation of some GPS signals. However, for a “top-bottom” configuration, both nulls formed by the adaptive antenna array will point towards the ground. This reduces the chance of GPS signals being rejected.

7.2 Test Procedures and Results

The tests were aimed at determining the anti-jamming ability of the unit in a controlled environment. During these tests, the aircraft was first placed on a mast high above the ground to simulate the same RF environment as it would experience when flying. The height of the mast was approximately 9m above the ground, and a 2MHz bandwidth jammer, centred at the GPS frequency, was located approximately 20m away from the mast. The radiated power of the jammer can be adjusted in increments of 1dB. The test configuration is illustrated in Figure 37.

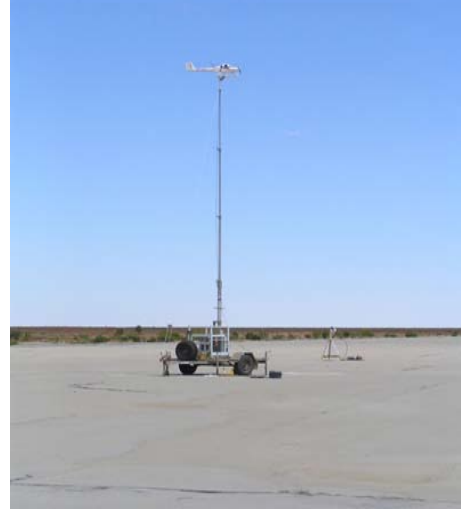
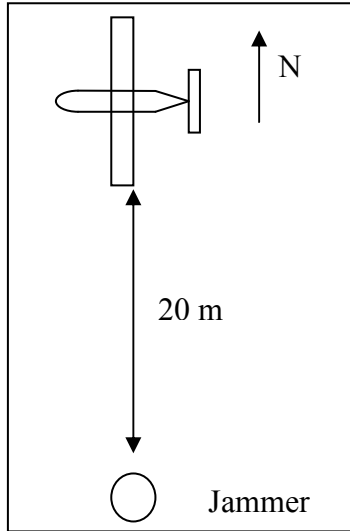


Figure 37: Test configuration

In order to assess the performance of the unit, the “GPGSV” (GNSS satellite in view) and “GPGGA” (global positioning system fixed data) receiver messages of both channels were used to obtain detailed information including satellites in view, the corresponding C/No and position information. This information was processed in MATLAB and plotted against jamming signal power. Hence, the AJ margin of the unit can be determined by examining the difference in jamming power levels at which the protected and unprotected receivers lost track of all satellites in view.

To further investigate the behaviour of the unit, the position information is also analysed. As the actual position of the UAV was fixed during all tests, the longitude and latitude values should remain constant. Therefore, only the position deviations of both receivers, after the jammer was turned on, have been calculated to assist the investigation. The test results of both antenna array configurations are detailed in the following sections along with the corresponding test analysis.

Top-bottom Configuration Static Test

Figure 38 shows the number of tracked satellites during the test with a “top-bottom” configuration. In this plot, the protected channel is shown in the top diagram and the unprotected channel is shown in the bottom diagram. The jamming power against time is also shown in the middle diagram. At the beginning of this test, when the

jammer was just turned on, both receiver channels were able to track 7 satellites. As the jamming power increases, the unprotected channel continued tracking all satellites during the early stage of the test but started to lose track of satellites when jamming power exceeded -105dBW. When the jamming power reached -100dBW, the unprotected channel lost track of all satellites. On the other hand, the protected channel was able to continue tracking 5 satellites or more until the jamming power increased to -62dBW. It lost tracking of all satellites when the jamming power reached -60dBW. This suggests that the anti-jamming unit is able to provide 38dB jamming protection.

The position information reported by both receivers during this test was compared with the initial position obtained when the jammer was not in operation and the deviations against jamming power are plotted in Figure 39. The behaviour of the position deviation curve agrees with the number of satellites in lock plot, shown in Figure 38. When jamming power reached -105dBW, the position of the unprotected channel drifted off. In the Figure 39, this is reflected by the longitude and latitude becoming a straight line towards the end of the test. This is because the receiver lost track of satellites, hence was not able to update the position. However, the position deviation for the protected channel remained less than $\pm 10\text{m}$ up to maximum jamming power of -62dBW. Therefore it can be concluded that the anti-jamming unit is able to provide 38dB protection which agrees with the anti-jamming margin obtained previously by observing the number of satellites in lock plot.

NOTE:

This figure is included on page 93 of the print copy of the thesis held in the University of Adelaide Library.

Figure 38: Number of Satellites in lock vs. jamming power [34]

NOTE:

This figure is included on page 93 of the print copy of the thesis held in the University of Adelaide Library.

Figure 39: Position deviation vs. jamming power [34]

Side By Side Configuration Static Test

The static test is repeated with the “side by side” antenna array configuration. The number of satellites in lock during this test is once again plotted in Figure 40 against jamming signal power. For the unprotected channel, the receiver lost track on all

satellites when jamming power exceeded -101dBW. However, the protected channel was still tracking satellites when the jammer reached its maximum power of -62dBW. Thus, the full anti-jamming range of the unit was not exercised in this test. It can be concluded that the AJ margin for this configuration is at least 42dB, which is 4dB more than the “top-bottom”. This result agrees with previous antenna configuration analysis.

NOTE:
This figure is included on page 94
of the print copy of the thesis held in
the University of Adelaide Library.

Figure 40: *Number of Satellites in lock vs. jamming power [34]*

The position errors were significantly higher in this test. The position deviations of both receivers against jamming power are plotted in Figure 41. From this plot, the unprotected channel started to drift off when jamming power was set to -106dBW and completely lost track at -104dBW. However, for the protected channel, the position variations were within +/-50m during the entire test and drifted off when the jamming power reached -64dBW. This suggests that -64dBW could be the maximum amount of jamming power the unit is able to handle, and confirms that the AJ margin for the “side by side” configuration is 42dB.

The larger position deviations at the start of the test shown in Figure 41 compared to the “top-bottom” configuration can potentially be explained by examining the C/No of each satellite. The C/No for all acquired satellites during both tests with the “side by side” and “top-bottom” configurations are shown in Appendix D. By observing

these two diagrams, it can be concluded that the average C/No for the protected channel with the “side by side” configuration was lower and unstable during this test, hence introducing more position errors. Most of the satellites had a C/No less than the threshold value of 30dB after the test was commenced at 55min, which is also when the position deviation curve, shown in Figure 41, starts to drift. This suggests the position errors were caused by the low C/No of the received GPS signals.

There are two possible reasons for the unstable C/No during the test. At the start of the test, only low level jamming was introduced. Hence the width of the null formed by the AJ unit is much wider compare with a high power jamming scenario. This will cause suppression of the GPS signals. The degraded signal quality introduced more positions errors. This could also be due to the self variable interference caused by the electronic unit.

NOTE:
This figure is included on page 95
of the print copy of the thesis held in
the University of Adelaide Library.

Figure 41: *Position deviation vs. jamming power* [34]

There are several possible explanations for lower C/No with the “side by side” configuration test. It is most likely due to the direction of the ambiguous null pointing towards the sky. The satellites may not be positioned exactly in the nulling direction, but as the null width is very wide for a two-element antenna array, as demonstrated in Chapter 3, the satellite signals may have been attenuated somewhat. For broadside

jamming with ideal antennas, 22.2% of the sky becomes GPS blind zone as shown in Figure 7. The visibility might be even worse in practical situation caused by non ideal antenna and ground reflection.

During this test, the two GPS patch antennas used to form the antenna array were placed side by side. This implies that the auxiliary antenna was necessarily placed closer to the electronic part of the unit, which might have caused it to pick up more self-induced interference from the unit. As the two-element adaptive antenna array is only able to handle a single interference signal at a time, any self-induced interference generated by the electronic part will be passed through to the receiver while the unit is cancelling out the main jamming signal. This would result in a drop in the C/No for the protected channel.

It was found that the strength of the self-induced interference by the electronic part of the unit is sensitive to the cable orientations and temperature variations. Changing the antenna configuration between the tests could have caused changes in the cable orientations resulting different RF environment for the two tests. As these parameters were not constantly monitored in the outdoor environment, it is difficult to know the exact reason for the drop in C/No values during this test.

7.3 Summary

Both of the tests performed during the trial with different antenna configuration showed that the anti-jamming unit is capable of providing approximately 40dB protection for a commercial GPS receiver in a real jamming environment. This value also agrees with the laboratory test result. The two antenna configurations have different strength and weakness, which have been also demonstrated in these tests.

For the “top-bottom” configuration, the unit was found to have a lower AJ margin of 38dB, but better C/No values and smaller position deviations, which were within +/- 20m. In comparison, the “side by side” configuration was able to provide at least 42dB anti-jamming range. Additional jamming power was not available from the jammer in order to fully exercise the unit under test. However, the test did demonstrate the “side by side” configuration resulted in lower C/No values and

greater position deviations. There are several possible reasons which could cause this problem. As has been analysed previously, the “side by side” antenna array configuration will cause the ambiguous null to point to the sky and hence may cause cancellation or degradation of GPS signals. Self-induced interference from the electronic part of the unit could also degrade the quality of the GPS signal. However, this can be improved by better EMC control.

In general, the “side by side” configuration is expected to be less suitable for UAV applications, once it starts to operate in a more dynamic environment. The cone shaped ambiguous null will change its direction along with the relative position between the aircraft and the jammer, which will result in a greater chance of cancelling the GPS signals. The short loss of signal from each satellite could cause receiver to lose track of that satellite and hence it would need to re-acquire. This process would occur for multiple satellites as the null direction changes, which will either degrade the overall positioning accuracy or stop the receiver from forming a position solution. To avoid this problem, the structure of the array has to be changed into a non-symmetrical shape and more antenna elements would be required. The detailed results of this trial were presented in [34].

Chapter 8

Conclusion

The sensitivity to in-band interference is a well known problem for GPS receivers due to low GPS signal strength. Many techniques have been developed to protect GPS receivers from intentional and unintentional jamming. Among these techniques, null steering is recognized as an effective method against both narrowband and broadband interference signal(s). However, as null steering requires an adaptive antenna array, it is difficult to fit it onto small platforms.

In this thesis, the suitability of null steering technique for small UAV applications has been examined. As a prototype, a two-element adaptive antenna array has been implemented aimed at protecting civilian GPS receivers only. The primary design objective of the unit was to maximize its AJ margin while still maintaining a small size, low weight and power consumption characteristics.

The null steering technique arranges the weights of the adaptive antenna array to form nulls in the directions of any incident interference signals while trying to maintain uniform gain in all other directions. The weight vector can be obtained by solving the Weiner Hopf equation, the solution of which has been approximated by using the LMS algorithm in this project due to its computational simplicity. As the LMS algorithm has to be implemented on FPGA, the DLMS algorithm was used instead to simplify the implementation. The DLMS algorithm allows the weight vector to be updated a few sample delays after the input signal.

The AJ margin of the unit is primarily limited by the system dynamic range, which is mainly constrained by the dynamic range of the RF front end. The RF front end is used to down-convert the received GPS signal to an intermediate frequency which is suitable for digitization. It is implemented using PCB technology. To maximise its dynamic range and overall sensitivity, components with high IIP3 points and low

noise figures have been chosen. The measured dynamic range of the RF front end was 55.6dB, which was 7dB less than the theoretically predicted value. This could be due to the layout of the RF front end and impedance mismatch between components and non-ideal performance of individual components.

As the adaptive antenna array employs two antenna elements, the AJ margin is also sensitive to mismatch between the two RF front ends. To minimize this mismatch, 20MHz has been used for the final bandwidth of the RF front end instead of 2MHz, which is the actual GPS operating bandwidth. Because a wider bandwidth has been chosen for the RF front end, subsequent filtering must be provided to reject all out of band noise. This is performed by the digital BPF, which is implemented on the FPGA. By doing so, the filter is able to have a more linear passband response and become insensitive to individual analogue components variation, thereby reducing the mismatch between the two RF front ends.

After the RF front ends were built, it was determined that the maximum mismatch within the GPS operating bandwidth was -1.5dB by examining the passband response. A three tap filter was added on the auxiliary channel to equalize this mismatch. A greater number of taps provide more degrees of freedom during the equalization, however, the number of taps the filter can have is constrained by the FPGA area. As a compromise between the overall performance and the FPGA area requirements, a three-tap filter has been implemented.

The tap delay line changes the behaviour of the adaptive antenna array. Signals incident upon the array from the interference direction will only be cancelled if their frequencies are close to the jamming signal frequency. In other words, by having the tap delay line on the auxiliary channel, the adaptive antenna array becomes frequency selective. As a drawback, the filter misadjustment will increase for the same convergence time.

The anti-jamming unit has been tested both in the laboratory and in a real outdoor jamming environment. A GPS simulator has been used in the laboratory test to provide GPS signals. This simulated GPS signal is mixed with a 2MHz interference, which was generated by a broadband noise generator. Cables of different length have

been used, in order to create the spatial delay, so that the interference and GPS signal did not appear to come from the same direction. In this test, an AJ margin of 40dB was obtained.

The unit was taken on trial in Woomera, November 2006. In this trial, two tests were conducted. Each test had a different antenna array configuration. With a “top-bottom” configuration, an AJ margin of 38dB was achieved and position deviations were within ± 20 m. In the “side by side” configuration test, the unit demonstrated at least 42dB AJ margin, which is 4dB better than the “top-bottom” configuration. However, with this configuration, the receiver experienced larger position errors. The position deviations during this test were within ± 50 m. This could be due to the ambiguous null pointing towards the sky causing degraded GPS signal strength. Self induced interference could also have caused a loss in C/No during this test. As these parameters were not constantly monitored in the outdoor environment, the exact reason for the inaccurate position information during this test could not be concluded. In practice, the “side by side” configuration is less suitable for UAV applications because the ambiguous null points towards the sky, potentially degrading the quality of the GPS signals.

In general, the AJ margin obtained from the trial agrees with the value obtained from the laboratory test, of approximately 40dB. This means that if an interference signal is strong enough to jam an unprotected receiver at 10,000m, with the anti-jam unit the receiver can be moved as close as 100m to the jammer and still remain operational.

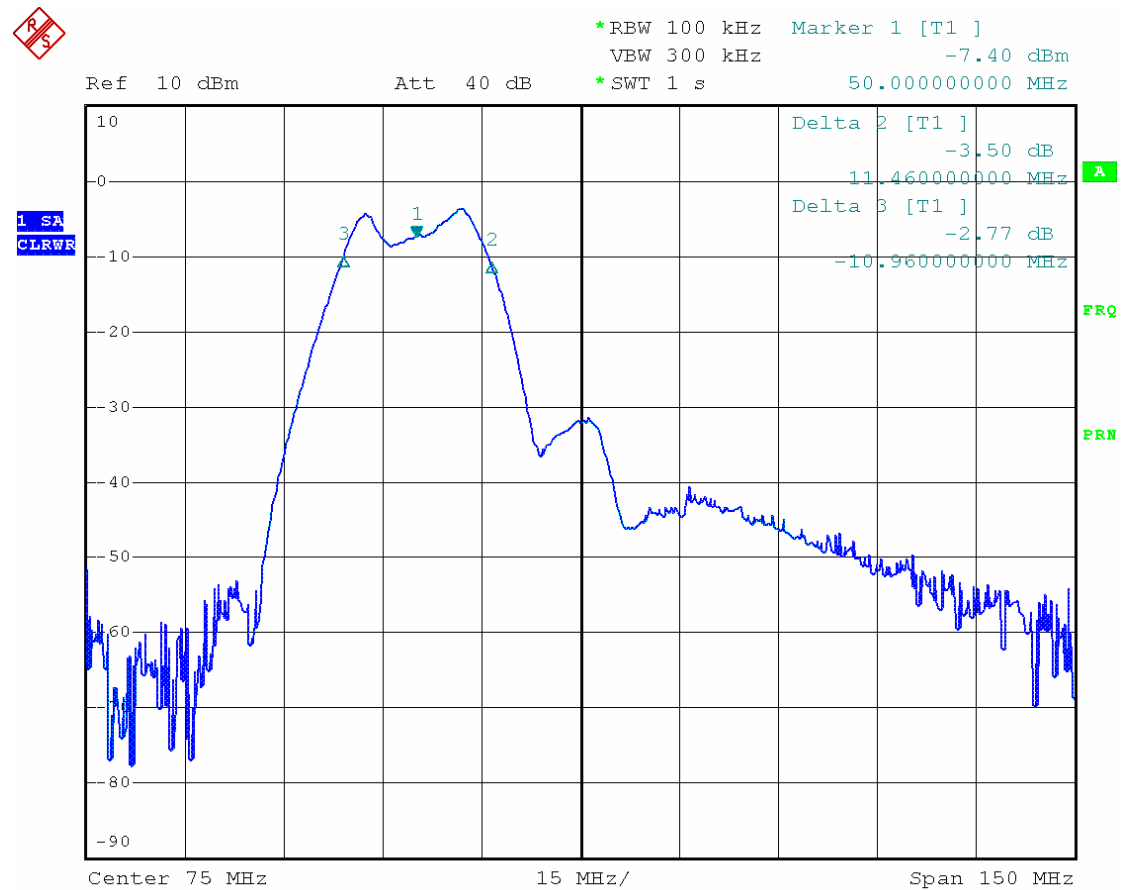
In conclusion, a detailed implementation of an anti-jamming unit for civilian GPS receiver has been described in this thesis. The unit is implemented based on adaptive antenna array technology with null steering approach, which provides the unit with ability to reject both narrowband and broadband interference signal. The anti-jamming ability of the unit has also been investigated in this thesis. When the unit was tested in a laboratory condition, 40dB anti-jamming range was achieved. 38dB and 42dB AJ margins were achieved when the unit was tested in a real jamming environment, with different antenna configurations.

The AJ margin can be further improved by implementing an AGC feature on the unit. It has been concluded in this thesis that the AGC feature should provide 7dB more in AJ margin, and this value was obtained by measuring the actual performance of the RF front end rather than its theoretical performance.

A NLMS algorithm has also been implemented in MATLAB aimed to improve the convergence time. The algorithm uses quantized step sizes and only requires 20% of the convergences time required by a conventional LMS algorithm. With this feature, the anti-jamming unit will become more robust against sudden changes in a jamming environment, which a UAV is likely to experience during a flight. The NLMS algorithm has been implemented with Xilinx blocksets in Simulink and can be easily adapted by the unit in any future development.

The overall size of the unit is approximately $14\text{cm} \times 8\text{cm} \times 6\text{cm}$ and weights 0.5 Kg, and all components used for the unit are commercially available. The total power consumption is 22W (11V by 2A). It can be concluded that the physical size and power consumption are reasonable for small sized UAV platforms.

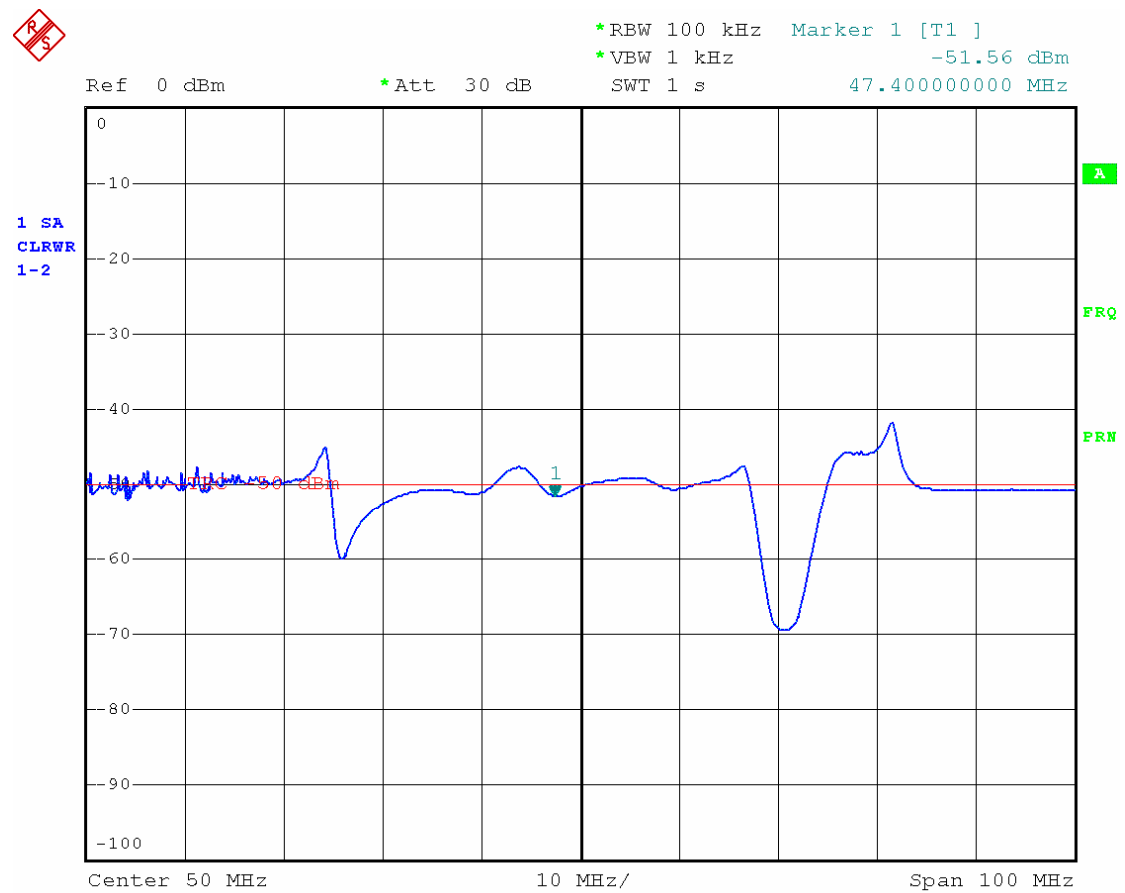
Appendix A - IF passband spectrum



Date: 16.JAN.2007 07:44:23

Figure 42: RF front end passband spectrum

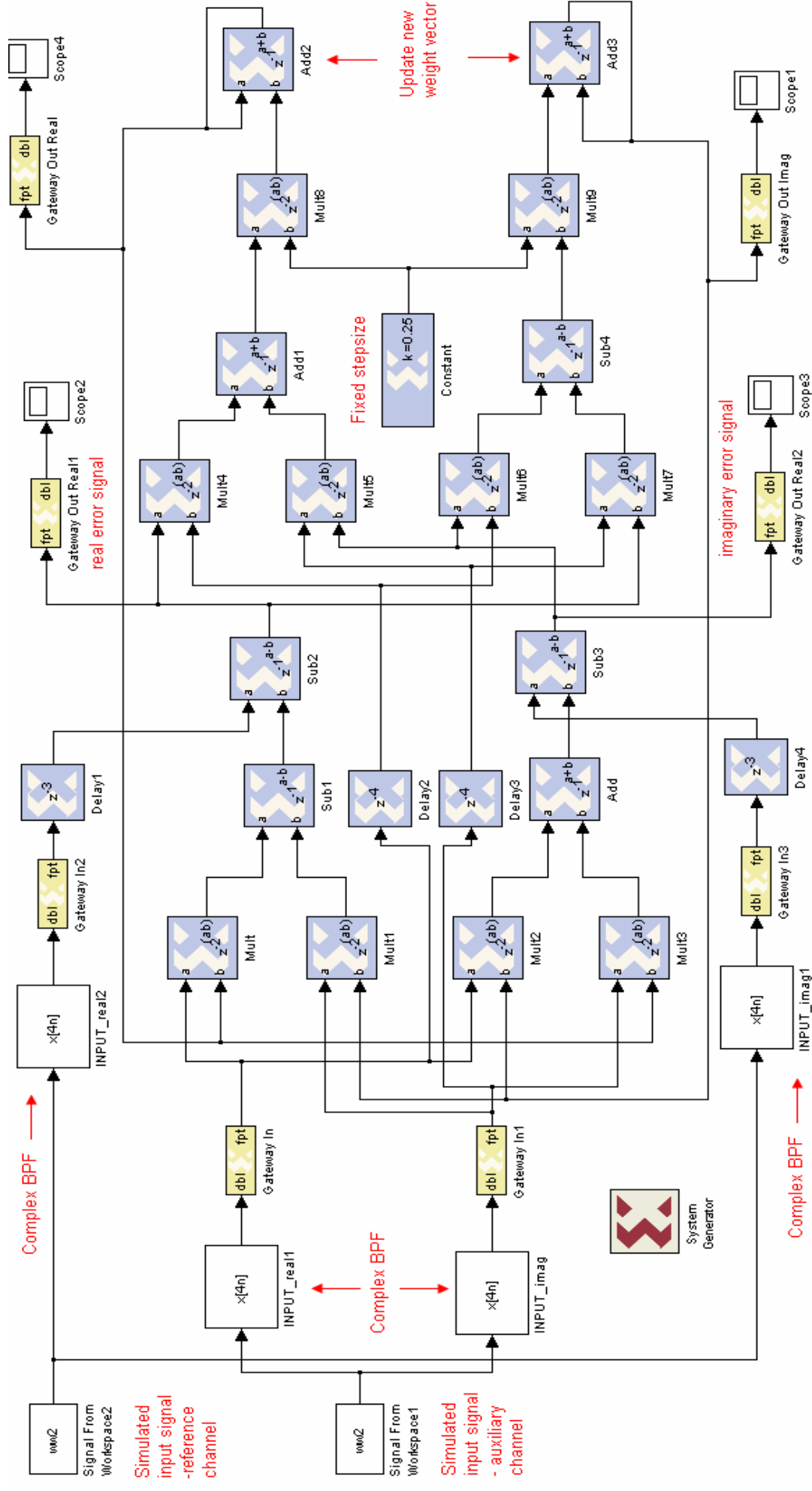
Appendix B - IF passband spectrum mismatch



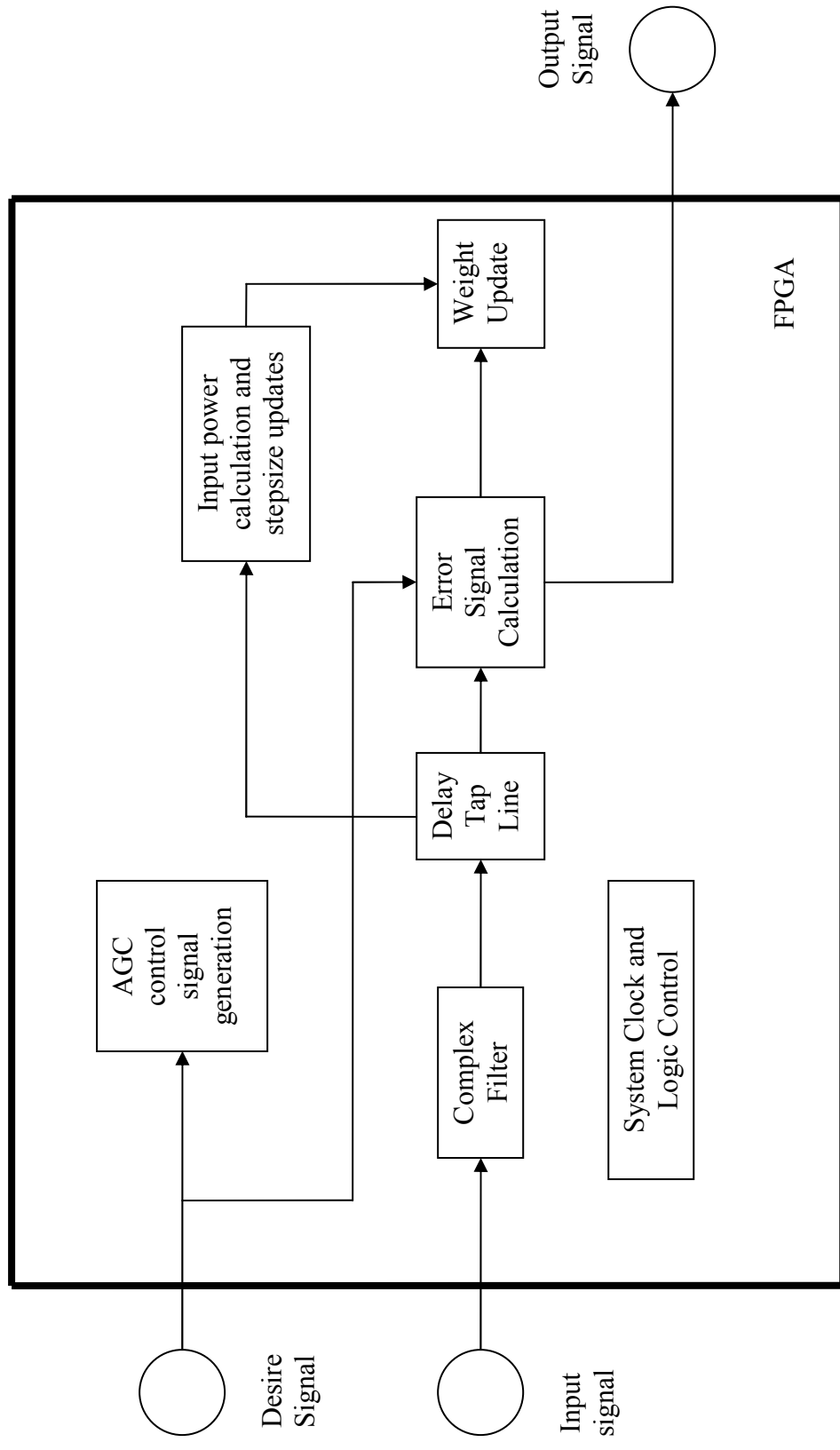
Comment: INPUT SIGNAL
Date: 18.JAN.2007 10:06:27

Figure 43: RF front ends pass band spectrum mismatch

Appendix C - snap shot of DLMS inside of Simulink



Block diagram of FPGA area allocation:



Appendix D - C/No of all satellites in trial

C/No of all satellites in static test

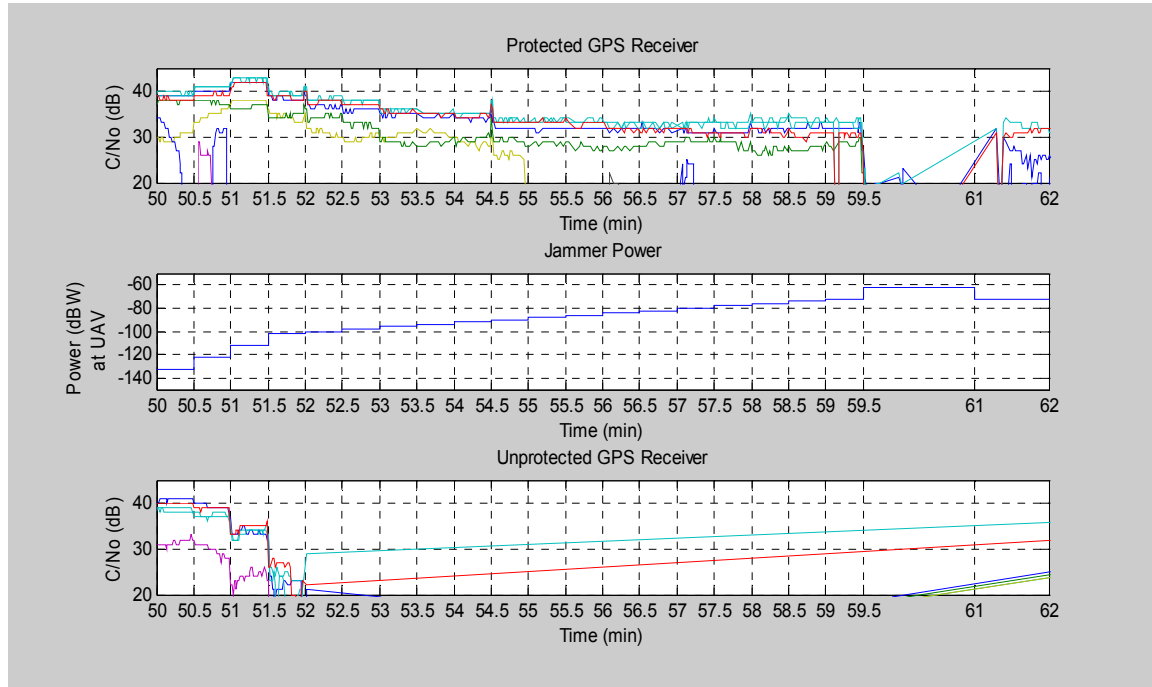


Figure 44: C/No of all satellites for “top-bottom” configuration

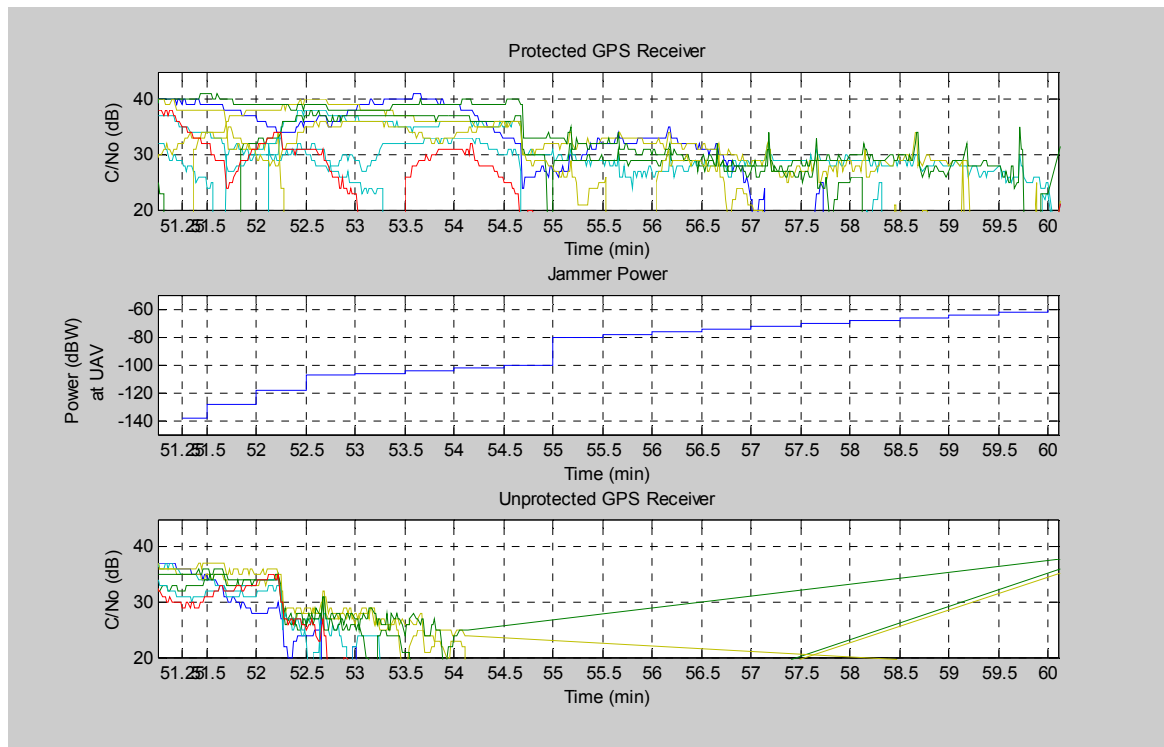


Figure 45: C/No of all satellites for “side by side” configuration

References

- [1] Kenneth S. Simonsen, Dean Nathans, Mark L. Suycott, John Wohlfel, Arch Turner and Bob Crumplar, “GPS: our Strongest assets or weakest links?”
- [2] Greg S. Loegering, “Dual-Redundant Antijamming Architecture for GPS-guided Air Vehicle Navigation System”, Technology Review Journal, Spring/Summer 2006. (page 4, 6, 9)
- [3] Tamal Bose, “Digital Signal and Image Processing” Malloy, Inc. pp. 422 – 474. (page 15, 16)
- [4] Dimitris G. Manolakis, Vinay K. Ingle, Stephen, M. Kogon, “Statistical and Adaptive Signal Processing”, Thomas Cason, 2000.
- [5] Rowan Gilmore, Besser Les, “Practical RF circuit design for modern wireless systems” Artech House, c2003.
- [6] John G. Proakis, Masoud Salehi, “Communication Systems Engineering” 2nd edition, Prentice Hall, 2001
- [7] C. J. Coleman, “ An Introduction to Radio Frequency Engineering”, Cambridge University Press, 2004
- [8] P. Capozza, B.Holland, T. Hopkinson, C. Moulin, P. Pacheco, R. Rinfkin, “Measured Effects of a Narrowband Interference Suppressor on GPS receivers”, ION 55th Annual Meeting, June 1999, pp. 645-651.
- [9] M. Trinkle, D. Gray “GPS Interference Mitigation; Overview and Experimental Results”, Proceedings of the 5th International Symposium on Satellite Navigation Technology & Applications, 2001, pp. 1-14.
- [10] Mi-Young Shin, C. Park, Ho-Keun Lee, Dae-Yearl Lee, Sang-Jeong Lee, “ An Adaptive Narrowband Interference Excision Filter with Low Signal Loss for GPS Receivers”. ICCAS2005, Korea.
- [11] D Lu, Q. Feng, R. Wu “ Survey on Interference Mitigation via Adaptive Array Processing in GPS” Progress in Electromagnetics Research Symposium 2006.
- [12] M. M. Casabona, M. W. Rosen, “Discussion of GPS Anti-jam Technology” GPS solutions, Vol. 2, No. 3, pp. 18-23(1999)
- [13] D. Moelker, Y. Bar-Ness, “An Optimal Array Processor for GPS Interference Cancellation”, 15th AIAA/IEEE Digital Avionics Systems Conference 1996, pp. 285-290.

- [14] D. S. De Lorenzo, J. Gautier, J. Rife, P. Enge, D. Akos “Adaptive Array Processing for GPS Interference Rejection” ION GNSS 2005.
- [15] M.D. Zoltowski, A. S. Gecan, “Advanced Adaptive Null Steering Concepts for GPS” MILCOM 1995, vol.3
- [16] G.F. Hatke, “Adaptive Array Processing for Wideband Nulling in GPS Systems”, 32nd Asilomar Conference on Signals Systems & Computers 1998, vol. 2
- [17] A. Gecan, P. Flikkema, A. D. Snider, “Jammer Cancellation with adaptive Arrays for GPS Signals”, Proceedings of IEEE, 11-14 Apr, 1996, pp. 320-323.
- [18] I. J. Gupta, T. D. Moore, “Space-Frequency Adaptive Processing(SFAP) for Radio Frequency Interference Mitigation in Spread-Spectrum Receivers”, IEEE transactions on antennas and propagation, vol. 52, NO. 6, June 2004.
- [19] “Spatial and Temporal Processing for Global Navigation Satellite Systems: The GPS Receiver Paradigm”. IEEE workshop on Statistical Signal and Array Processing, Pocono Manor, PA, August 2000.
- [20] United States Patent, Patent Number 4,771,289 by Raymond J. Masak, 13th, Sep, 1988.
- [21] Chung-Liang Chang, Jyh-Ching Juang, “Analysis of Spatial and Temporal Adaptive Processing for GNSS Interference Mitigation” Proc. IAIN/GNSS, Korea, 2006
- [22] K. Falcone, G. Dimos, C. Yang, F. Nima, S. Wolf, D. Yam, J. Weinfeldt, P. Olson, “Small Affordable Anti-Jam GPS Antenna (SAAGA) Development” ION GPS-99, 12th International Technical Meeting of the Satellite Division of the Institute of Navigation, Sep, 1999, Tennessee.
- [23] R. L. Fante, J. J. Vaccaro, “Wideband Cancellation of Interference in a GPS receiver Array”, IEEE transaction on Aerospace and Electronic Systems, vol. 36, NO. 2 April 2000.
- [24] W. L. Myrick, M. D. Zoltowski, J. S. Goldstein, “GPS Jammer Suppression with Low-Sample Support using Reduced-Rank Power Minimization”, Proc. 10th IEEE Workshop on Statistical Signal and Array Processing, 2000.
- [25] S. Rounds, “Jamming Protection of GPS Receivers: Part I : Receiver Enhancements”, GPS World, Jan, 2004.
- [26] C. R. Hamm, W. S. Flenniken, IV, D. M. Bevely, D. E. Lawrence, “Comparative Performance Analysis of Aided Carrier Tracking Loop Algorithm in High Noise/ High Dynamic Environment”, Proc. ION GNSS 2004.
- [27] S. Alban, D. M. Akos, S. M. Rock, D. Gebre-Egziabher, “Performance Analysis and Architectures for INS-Aided GPS Tracking Loops”, Institute of Navigation’s National Technical Meeting, Anaheim, CA. Jan, 2003.

- [28] R. Babu, J. Wang, "Ultra-Tight GPS/INS/PL Integration: Kalman Filter Performance Analysis"
- [29] J. Anon. Interference Control Document GPS-ICD-200, with IRN-200B-PR001, Department of the Air force, USA, July 1, 1992.
- [30] B.W. Parkinson, J. J. Spilker, "Global Positioning System: Theory and Application", Volume 1, p77, 1996.
- [31] S. Haykin, "Adaptive Filter Theory", 4th edition, Prentice-Hall, Inc, 2002.
- [32] R. J. Baker, "CMOS Circuit Design, Layout and Simulation", 2nd edition, Wiley Interscience, 2005.
- [33] C. Rauscher, "Fundamentals of Spectrum Analysis", 1st edition, Rohde&Schwarz GmbH&Co.KG, 2001.
- [34] M. Trinkle, J. Li, "GPS Mini Gismo-II Trial Report", Department of Electrical Electronic Engineering, The University of Adelaide, Nov, 2006.
- [35] D. Reynolds, A. Brown, A. Reynolds, "Miniaturized GPS antenna array technology and predicted anti-jamming performance", Proceedings of ION GPS'99, Nashville, TN, Sep, 1999.
- [36] G. Bucco, M. Trinkle, D. Gray, W.C. Cheuk, "FPGA Implementation of a Single Channel GPS Interference Mitigation Algorithm", Journal of Global Positioning System 2004, Vol. 3, No.1-2: 106-114.
- [37] C. Chien, "Digital Radio Systems on a Chip", Kluwer Academic Publishers, 2002.
- [38] W. F. Egan, "Practical RF System Design", John Wiley&Sons, INC., Publication, 2003.
- [39] D. Li, J. Wang, "Performance Analysis of the Ultra-Tight GPS/INS Integration Based on an Improved Kalman Filter Design for Tracking Loops", IGNSS Symposium 2006.